Architecture and IC Implementation of Ultrasound Communication and Rangefinder Systems for Sensor Swarms

Architecture and IC Implementation of Ultrasound Communication and Rangefinder Systems for Sensor Swarms

Gönenç Berkol

This work has been funded by the European Union's Horizon 2020 research and innovation programme under grant agreement No 665347.

Cover design by Gönenç Berkol

Berkol, G.
Architecture and IC Implementation of Ultrasound Communication and Rangefinder Systems for Sensor Swarms
Proefschrift Technische Universiteit Eindhoven, 2021.
A catalogue record is available from the Eindhoven University of Technology Library
ISBN 978-90-386-5210-8
NUR 959

Architecture and IC Implementation of Ultrasound Communication and Rangefinder Systems for Sensor Swarms

PROEFSCHRIFT

ter verkrijging van de graad van doctor aan de Technische Universiteit Eindhoven, op gezag van de rector magnificus prof.dr.ir. F.P.T. Baaijens, voor een commissie aangewezen door het College voor Promoties, in het openbaar te verdedigen woensdag 24 februari 2021 om 16:00 uur

door

Gönenç Berkol

geboren te Izmir, Turkije

Dit proefschrift is goedgekeurd door de promotoren en de samenstelling van de promotiecommissie is als volgt:

voorzitter:	prof.dr.ir. P.H.N. de With
1e promotor:	prof.dr.ir. E. Cantatore
2e promotor:	dr.ir. P.J.A. Harpe
leden:	prof.dr. M. Matters-Kammerer
	prof.dr. P. Reynaert (KU Leuven)
	dr.ir. M.A.P. Pertijs (TUD)
	prof.dr.ir. P.G.M. Baltus

Het onderzoek of ontwerp dat in dit proefschrift wordt beschreven is uitgevoerd in overeenstemming met de TU/e Gedragscode Wetenschapsbeoefening.

Contents

List of symbols and abbreviations

Symbol	Description
ADC	Analog to Digital Converter
ANTS	Autonomous Nanotechnology Satellites
BER	Bit Error Rate
CMUT	Capacitive Micromachined Ultrasound Transducers
CMOS	Complementary Metal Oxide Semiconductor
CW	Continuous Wave
EC	Evolutionary Computation
FFT	Fast Fourier Transform
FoM	Figure of Merit
FMCW	Frequency Modulated Continuous Wave
FDD	Frequency Division Duplexing
ID	Identification
IC	Integrated Circuit
MEM	Micro Electro Mechanical
NEF	Noise Efficiency Factor
OOK	On Off Keying
PZT	Piezoelectric Transducer
PVT	Process Voltage Temperature
PE	Pulse Echo
RF	Radio frequency
RSSI	Received Signal Strength Indicator
SNR	Signal to Noise Ratio
SBPM	Single Balanced Passive Mixer
SI	Swarm Intelligence
SCC	Switched Capacitor Converter
TDoA	Time Difference of Arrival
ToF	Time of Flight
US	Ultrasound
WuRX	Wake-up Receiver

Chapter 1

Introduction

1.1 Background

Biological evolution by means of a natural selection, as stated by Charles Darwin in 1859 [1], continues to inspire modern-day science including electrical engineering. Evolutionary Computation (EC), a biologically inspired computational approach, becomes one of the emerging tools that can be utilized to solve complex optimization problems. The general and systematic nature of EC can be applied to various emerging applications ranging from silicon integrated circuit (IC) design [2,3] to developing aerospace systems for outer space exploratory missions [4]. The fundamental algorithm of EC can be explained as follows [5]: A population, representing the set of candidate design solutions of an optimization problem, is generated as a first step. This is followed by a selection process, where some of the individuals in the population are chosen based on pre-defined performances (i.e. survival criteria as used in Biology). The performances can be estimated through a simulation or a real-life measurement and can be expressed in terms of a cost function. Some individuals in the population outperform the others with respect to their cost function. This means that these individuals have more probability of survival, or satisfy better to the design goal of the optimization. The next step in the algorithm is recombination (mating) of the chosen individuals, where the next generation of the population (candidate design solutions) are generated by mixing the chosen individuals. This step is critical and the goal is to increase the diversity of the population as much as possible. This is followed by new performance estimations to obtain the cost function of the new population, and this iteration is repeated until the design criteria of the optimization problem are met.

Swarm Intelligence [6] (SI) is another example of biologically inspired methods. SI is used when the exploration of a hostile and/or difficult-to-access environment is desired. During the exploration, a large number (swarm) of sensor nodes is used. This is needed especially when the environment to be explored by these sensor nodes cannot be accessed by humans due to the harsh environmental conditions. Considering this,

a large number of nodes is beneficial in case one or more of the nodes get damaged. Thus, required exploratory tasks such as sensing, distance measurement, data collection, and data processing, etc. are distributed throughout the swarm of the nodes, rather than having one (super) sensor node that is capable of performing all tasks. An important highlight of these systems is that the collective information obtained by the swarm is used to analyze the properties of the environment explored. A good example is a space mission of NASA, called Autonomous Nanotechnology Satellites (ANTS), where 1000 intelligent satellites are used to investigate an asteroid belt [7].

1.2 The Phoenix Project

The Phoenix project [8] aims to investigate a new paradigm that will enable the exploration of difficult-to-access environments through a swarm of sensor nodes. The idea behind the Phoenix concept is built upon the EC and SI methods explained in the preceding section. The sensor nodes are used to gather data from the operating environment, where the information collectively gathered by the swarm is analyzed by means of post-processing. These data are used by the (offline) algorithms to perform evolution, as in the conventional EC method, to extract information about the environment explored by the swarm. The sensor nodes can improve their performance in terms of quality of the generated information and energy efficiency, via successive generations, in an artificial evolution scheme based on the EC and SI methods. For instance, the sensor nodes can use ultrasound or electromagnetic signals for communication and localization, and sense several parameters such as pressure, salinity, and temperature, while the desired end goal of the exploration could be the pressure and/or temperature map, detecting a leakage (if any) of a water pipe, and a topological map of the environment visited by the sensor nodes. This unique property is called co-evolution and can be repeated until the desired exploration task is met. The broad range of possible applications can be addressed by having several casts[1] of the sensor nodes that can be chosen by the evolutionary loop depending on the application of interest [8, 9].

According to the Phoenix concept, in this thesis, we focus on the system and hardware design of the swarm of nodes, to enable communication and distance measurements among the sensor nodes, while the goal of the exploration task is to find the geometry of an enclosed volume to be explored. The application considered in this thesis is the exploration with a swarm of sensor nodes of enclosed volumes filled with fluids[2], in places that are missing GPS coverage. Examples of such volumes are water pipelines or oil distribution systems, underground infrastructures like reservoirs, and industrial mixing tanks for processing chemicals [10–12]. Future directions of the applications may include medical monitoring, or investigating the water droplets found in space missions. Human access to these enclosed (semi-)liquid-filled volumes is very limited.

[1] A class of nodes having a specialized function

[2] Liquid-filled volumes have been considered in the context of this work

Moreover, radio frequency (RF) signal propagation inside the volume is difficult due to the severe attenuation of RF signals in liquids. In addition, remote access to the sensor nodes inside the volume is not guaranteed. As a result, ultrasound (US) has been chosen in the nodes for a low bit-rate data exchange as US propagates with a lower attenuation in liquids compared to RF. On one hand, miniaturized and energy-constrained sensor nodes are needed considering the limited size of these environments. On the other hand, the sensor nodes have to perform a power-hungry US data exchange to find the relative distance among each other. Fig. 1.1a shows an

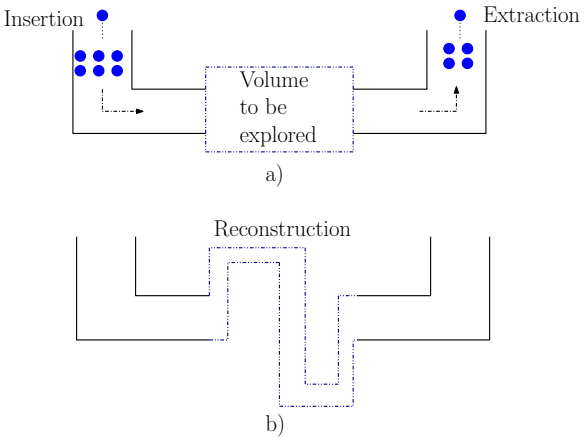

Figure 1.1: a) An illustration of the go-with-the-flow approach b) A possible outcome of the exploration.

application of the Phoenix concept, called go-with-the-flow [13] approach, that has been considered in this thesis. At the Insertion point, the swarm of sensor nodes is inserted in the volume to explore. Inside this (unknown) volume, the sensors perform distance measurements among each other, while going with the flow of the medium [13]. Mutual distance measurements are recorded in their memory while the nodes are traversing the volume to explore. These data are analyzed after recuperating the sensor nodes at the Extraction point. As shown in Fig. 1.1b, post-processing is performed subsequently at central stations to reconstruct the information about the geometry of the volume traveled by the swarm of sensor nodes, based on the mutual distance measurements performed [13–15].

1.3 Problem Statement

The enclosed volumes which the sensor nodes are traversing can be man-made industrial infrastructures (pipelines and mixing tanks) that are used for extracting and distributing fluids such as oil and water, or can be natural underground infrastructures like reservoirs and wells. A detailed comparison of these volumes is given in [13], where the typical sizes of the pipeline, reservoir, and industrial mixing tanks

are given as 1000x1x1m, 1000x0.1x0.1m, 10x10x10m, respectively. Clearly, the size of the (swarm of) nodes should be small enough to enable injection in these volumes. This means that the communication and distance measurement system to be developed for these applications is constrained by the limited available energy due to the small physical size requirement of a node in the swarm.

Using US for data-exchange in liquids enables larger propagation distance compared to RF [16,17]. Moreover, the compatibility of micro-electro-mechanical (MEM) transducers with complementary metal-oxide-semiconductor (CMOS) technology can lead to miniaturized systems [18,19], holding the promise for building a small form-factor US-enabled sensor node. However, there are two main obstacles when interfacing to the transducers. The first one is their relatively large electrical capacitance (pF to nF range [20]). When driving the US transducer, a big portion of the used energy is dissipated to charge and discharge this large capacitance. The second obstacle is that the propagation in the enclosed volumes considered in this thesis, is characterized by multipath propagation and collisions (interferences) among different sensor nodes [21,22]. The detrimental effects of these phenomena are escalated when a dense swarm of sensor nodes is used.

There are many ranging (distance measurement) methods proposed for sensor nodes that are operated in liquids [23, 24]. Unfortunately, the majority of them are based on either using additional hardware like GPS or having a beacon (or a super node) in the network that has the capability of communication with the outside world and the other sensor nodes: these approaches are not suited for the applications considered in this thesis. Moreover, a global network synchronization [25] requires either highly stable timing sources (such as atomic clocks) or advanced MAC protocols [26] that require exchanging several data packets. These approaches are too power hungry for our applications. Typical US distance measurement methods exploit Time-of-Flight (ToF) of the US echoes coming from passive reflectors. However, collisions and multipath propagation of the echoes experienced when the nodes are operated in an enclosed volume increase the complexity of the distance measurements and decrease their reliability when reconstructing the geometry of the explored volumes. In [13, 27] a two-way ranging protocol suited to the go-with-the-flow approach is presented. It is based on recording the ToF of US among (multiple) sensor nodes in a cluster using a modified version of the conventional two-way ranging (i.e. recording the round trip time of US going back and forth). However, this method depends on successfully receiving (and saving) many US interactions among the nodes, while the effect of multipath and collisions, as well as low-level implementation details such as the type of transducers, modulation schemes, frequency of operation, etc. have not been considered. To the best of the authors' knowledge, no experimentally validated ranging protocols and US distance measurement methods exist in the literature that simultaneously address the multipath and collision phenomena while avoiding synchronization requirements of the sensor nodes in a swarm. In the following sections of this thesis, we use the term rangefinder system to combine the method of distance measurement, the embodiment of the distance measurement method, and the distance measurement protocol into one word to simplify the explanation.

1.4 Aim of the thesis

This thesis aims to develop the system and circuit level concepts enabling ultrasound communication and rangefinder systems that suit the Phoenix concept using the go-with-the-flow approach. In addition, integrated-circuit design of such systems and their proof-of-concept experimental characterization are the main goals. Accordingly, the research questions this thesis aims to answer can be summarized as:

1. Can we establish an energy-efficient ultrasound communication link among the resource-limited sensor nodes?
2. Can we devise an ultrasound rangefinder system for a swarm of sensor nodes that can successfully operate in collision and multipath rich enclosed volumes?
3. Can we design critical building blocks of these systems at a transistor-level and experimentally demonstrate the proof-of-concept principle of the proposed systems?

The target features of the envisioned ultrasound rangefinder and communication system are as follows:

- State-of-the-art sensitivity and energy per bit for an ultrasound transceiver.
- State-of-the-art energy per measurement for an ultrasound rangefinder without global clock synchronization within the swarm.

1.5 Scope of the thesis

The scope of this thesis is limited as follows:

- This thesis focuses on the design, implementation, and characterization of the ultrasound interface circuits. Other circuit blocks needed to complete the rangefinder system, such as power management, voltage regulation, and bias generation are not in the scope of this thesis. On-chip clock generation is done for an always-on wake-up receiver (Chapter 3), however, the higher frequency clock needed for the digital circuitry (Chapters 2 and 3) is provided from off-chip oscillators and is not in the scope of this work.
- The design and implementation of the reconstruction algorithm needed to map the operating enclosed volume after the nodes are recuperated is not in the scope of this thesis.

- The design and implementation of the MEM transducer is not in the scope of this thesis, and commercially available transducers [20] are used during the proof-of-concept experiments.

- The design and implementation of the peripheral digital circuits (see Chapters 2 and 3) and the digital backend needed in the proposed systems are not in the scope of this thesis. Besides, the power-hungry digital signal processing needed (for instance Fast Fourier Transform (FFT)) are performed off-line after the nodes are recuperated.

- The FFT of the data gathered by the ICs and the high-level protocol used to control the ranging among the nodes are implemented in MATLAB.

- The methods proposed are tailored to be used in liquid-filled enclosed volumes. However, experimental characterization of the proof-of-concept principle of the rangefinder systems has been performed in air due to the difficulty to measure at large distances in liquids, and thus to simplify the experimental characterizations by keeping the maximum distance between the sensor nodes at a manageable level.

- Standard 65nm CMOS technology is used for the IC implementations.

1.6 Own Contributions

Novel system architectures and circuit level techniques have been proposed to enable state-of-the-art energy efficiency in ultrasound communication and rangefinder systems for the exploration of enclosed volumes with a swarm of sensor nodes. The contributions of this thesis can be summarized as follows:

- *Proposal of a communication system for symmetrical ultrasound links.* Its system and circuit level implementation details and the main experimental results are described in Chapters 2, 3, and 4, respectively, which are based on the papers included in Appendices C and D.

- *Proposal of two Frequency-Division Duplexing (FDD) Frequency Modulated Continuous Wave (FMCW)-based ultrasound rangefinder systems.* Their system and circuit level implementation details and the main experimental results are detailed in Chapters 2, 3, and 4, respectively, which are based on the papers included in Appendices A, B, and the patent described in [28].

Specifically, three ICs (see Fig. 1.2) have been designed, implemented, and experimentally characterized to investigate the aforementioned architectures. This work thus describes:

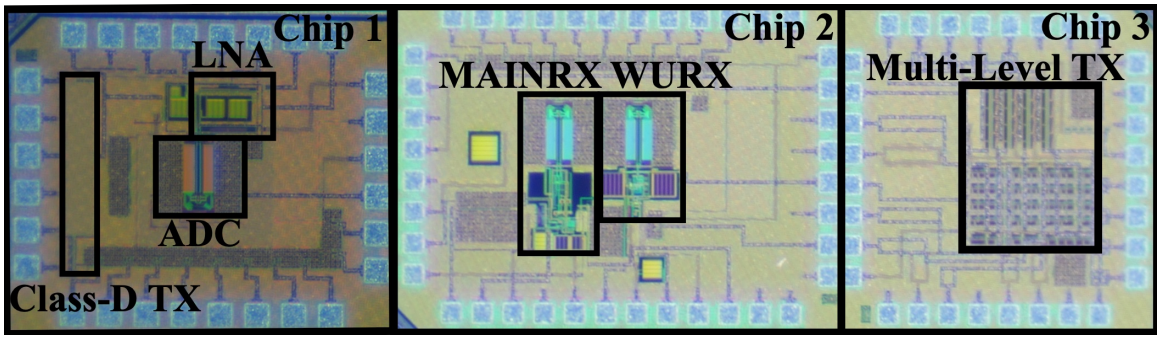

Figure 1.2: Die photos of the chips designed in this thesis.

Chip 1 The design, implementation, and characterization of a Class-D transmitter and a low-power receiver comprising an LNA and a 10-bit SAR ADC. The power consumption of the LNA and ADC is measured as 1.18μW. The receiver sensitivity is $-81.6dBm$ at a 10^{-3} Bit Error Rate (BER) level, which enables an experimentally verified transmission over 3.2m in air. The measured power consumption of the transmitter at a 1kb/s data-rate is 50μW. Measurement results show that the proposed circuits (Chip 1) achieve a state-of-the-art sensitivity ($-81.6dBm$) and energy-per-bit ($51.18nJ/b$) for an ultrasound transceiver (see Appendix C).

Chip 2 The design, implementation, and characterization of an ultra low-power wake-up receiver (WURX) and a ranging receiver (MAINRX). The wake-up receiver operates at a 23.6nW of total power consumption under a supply voltage of 0.6V while achieving the best wake-up Figure-of-Merit (FoM) of $0.79 \cdot 10^{-20}(J/b) \cdot W$ in the present state-of-the-art. The ranging receiver operates at a 0.56μW of power while using a single 0.6V supply. It includes a single-ended low-noise amplifier using a novel DC feedback method (see Appendices A and B).

Chip 3 The design, implementation, and characterization of a multi-level transmitter (TX). Chip 3 includes two switched-capacitor converters and an output multiplexer to output a four-level signal. The multi-level circuit saves more than 30% energy on the large capacitance of the ultrasonic transducer compared to a two-level transmitter.

Combining the above-mentioned Chip 2 and Chip 3, novel ultrasound rangefinder systems suited for the go-with-the-flow approach have been presented (see Appendices A and B). A Wake-up and FMCW based ultrasound rangefinder system achieving a state-of-the-art energy consumption of $1.25\mu J$ per measurement has been experimentally demonstrated (see Appendix A).

1.7 Outline of the thesis

This thesis consists of five chapters and four appendices including the scientific papers, as shown in Fig. 1.3. The aim of the chapters is to give an introduction to the key contributions proposed in this thesis at the system and circuit level. The chapters give a concise summary of the scientific publications in the appendices, yet provide a thorough overview for the readers. After the introductory Chapter 1, system-level contributions are discussed in Chapter 2. Specifically, the theoretical principles of symmetrical ultrasound links and two ultrasound rangefinder systems based on FDD-FMCW are introduced. Chapter 3 summarizes the design of three key interface circuits: low-noise amplifier, transmitter, and wake-up receiver. Chapter 4 describes the main experimental results of the proposed ultrasound communication and rangefinder systems. In the appendices of this thesis, the scientific publications are included. Whenever needed, the readers are referred to the corresponding scientific publications for more detailed information about the design, implementation, or experimental characterization.

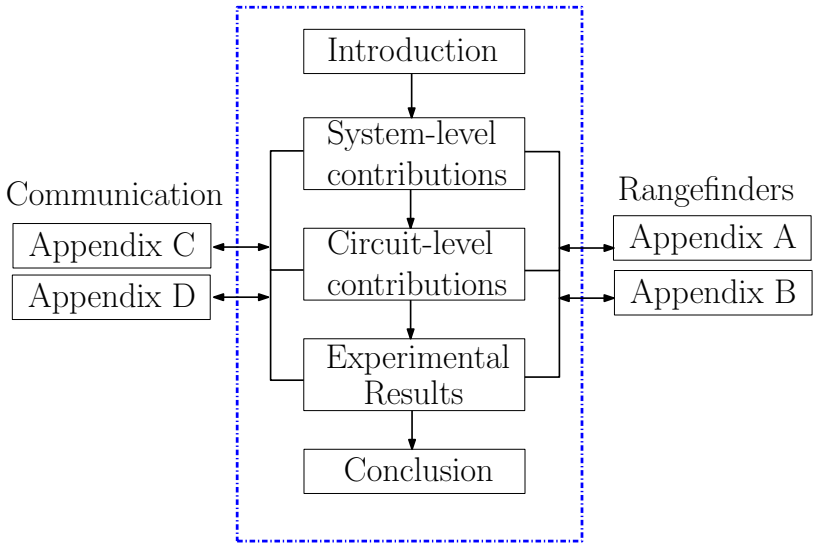

Appendices	
A	Wake-up based FDD-FMCW
B	FDD-FMCW with a Chirp Exchange
C	Symmetrical US links
D	Underwater US links

Figure 1.3: Outline of the thesis

Chapter 2

System-Level Contributions

This chapter discusses system-level contributions of this research, where Section 2.1 deals with ultrasound communication, and Section 2.2 deals with ultrasound rangefinder systems.

2.1 Communication Links for Sensor Swarms

The Phoenix project exploits the go-with-the-flow approach to be used in emerging applications such as the exploration of the ocean floor, underground infrastructures, water distribution systems, and industrial tanks for processing chemicals [9, 11, 13, 29, 30], as discussed in the previous chapter. From a system-level perspective, these applications have in common that miniaturized and resource-limited sensor nodes in a swarm will be used for the exploration of fluidic environments. For the exploration, the nodes must provide two main functions: communication and ranging. Indeed the sensor nodes should be able to exchange information, e.g. the sensed quantities and measured distances, which allows retrieving more useful data when all or some of the nodes are recuperated. Thus, this section focuses on system-level design choices, e.g. the type of signals used for the data-exchange, modulation schemes, and frequency of operation to build a low-power communication system for sensor swarms.

2.1.1 Type of Signals to be used in Fluids

The first step towards building a communication system for sensor swarms is to choose an appropriate propagation signal to be used in fluidic (i.e. liquid-filled) mediums. Radio Frequency (RF) communication is extensively studied for terrestrial wireless applications. RF communication enables implementing sophisticated network architectures and advanced modulation schemes with high data-rate communication [31]. Despite these attractive properties, the path loss of RF signals in conductive mediums (like most liquids) becomes severe (e.g. up to 300dB/m in seawater at 67MHz [32]),

which limits the effective communication distance [33]. Low-frequency RF signals (<20MHz) have been used in underwater environments to achieve long transmission distances, however, the power budget and antenna size needed for implementing low-frequency radio systems [34] are not suited for the miniature applications considered in this thesis.
Optical signals have short wavelengths (e.g. 400nm for blue light and 700nm for red light), high frequency and high speed in liquids, which would enable developing high performance communication systems [35]. The drawback of using optical signals is that the clarity (transparency) of liquids has a significant influence on communication performance [34]. Besides, line of sight is required for communication. As a result, optical signals limit the type of fluidic environments to be explored and are thus not considered to be suitable for our applications.
Ultrasound (US) has been widely used in wireless systems operated in liquids (e.g. Underwater Wireless Sensor Networks (U-WSNs) [36]). The fundamental reason for exploiting US is its favorable attenuation characteristics in liquids compared to RF. Indeed, US propagates with a low attenuation coefficient (e.g. <10dB/km at 100kHz in water [34, 37]), which could be exploited for an energy-efficient data exchange over long distances. In addition, US transducers used for transmitting and receiving ultrasound signals can be fabricated with CMOS compatible technologies, enabling miniaturization of the nodes. For these reasons, US has been chosen in this thesis as a propagation signal to be used among the sensor nodes.

2.1.2 US Transducers, Link Capacity, and Modulation Schemes

Ultrasound transducers are devices that are capable of converting energy between the acoustic and the electrical domain [38]. When the transducer is excited with an electrical energy (e.g. with a high voltage pulse at a suitable frequency), the device converts this energy to the acoustic domain and transmits a pressure wave (i.e. an ultrasound signal) to the environment. Similarly, the device produces an electrical response when it receives a pressure wave. As a result, wireless data exchange among the nodes can be realized by using ultrasound transducers to send and receive US waves in the operating environment.
The channel capacity of ultrasound links, the highest data-rate that can be achieved in a noisy channel, can be estimated by Shannon's law [39] ($C = BW \cdot log_2(1+SNR)$), where the channel capacity (C) is determined by Signal to Noise Ratio (SNR) and bandwidth (BW). In ultrasound communication links, the bandwidth is limited by that of the transducers. Piezoelectric transducers (PZTs) have been used in this thesis mainly because of their availability in the market [20]. Commercial piezoelectric transducers typically have a nominal operating frequency spanning from a few tens of kHz to several hundreds of kHz [20] and a relatively low bandwidth (up to a few tens of kHz [17]), which limit the achievable data-rate to a few tens of kb/s [17]. Although Capacitive Micromachined Ultrasound Transducers (CMUTs) have been used in literature [40] to achieve a larger bandwidth (up to a few tens of MHz [41]) compared to PZTs, the high-voltage DC bias requirement of CMUTs (e.g. 40V in [42])

is an important drawback in the battery-operated applications.
To increase data rate, bandwidth-efficient modulation methods such as Quadrature Amplitude Modulation (QAM), as well as multi-carrier modulations in the form of Orthogonal Frequency Division Multiplexing (OFDM), have been demonstrated for ultrasound links established in liquids [43, 44]. However, as the complexity of the modulation schemes increases, the complexity of the hardware needed increases too. Hardware complexity typically leads to higher power consumption. For this reason, simpler modulation schemes, e.g. On Off Keying (OOK), has been considered in this work due to the very limited energy available in the nodes.

2.1.3 High-Level Trade-offs in US Communication

Fig. 2.1 depicts an example of an arbitrary sequence transmitted using OOK communication among two identical nodes, where the left node broadcasts the symbols '101'. In this example, the problem is simplified by focusing on data exchange among two nodes to give a high-level description of the communication system and to highlight the main challenges related to the power consumption of the nodes.

To realize the example communication system shown in Fig. 2.1, each node needs

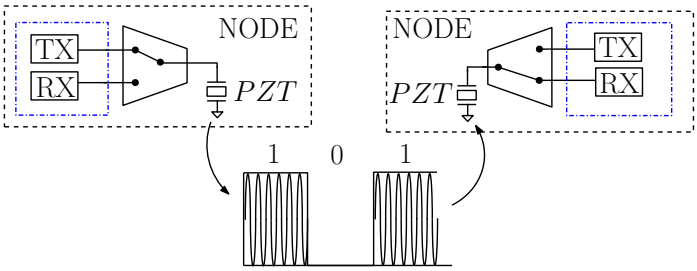

Figure 2.1: An illustration of OOK communication among the nodes. The sensor nodes comprise a transmitter, TX, a receiver, RX, and a US transducer, PZT.

to use an ultrasound transducer, PZT, a receiver, RX, to sense the electrical response of the transducer, and a transmitter, TX, to drive the transmitting transducer and broadcast the data. The PZT transducer can be connected to either TX or RX with a switch that can be controlled based on a suitable protocol.
Lowering the power consumption of the RX and TX is of special interest in the context of this work, considering the resource-limited and miniaturized nodes needed for the exploration, as discussed in Chapter 1. To lower power consumption, one could choose a PZT that has a relatively low resonance frequency. This helps reducing the frequency dependent attenuation of US propagation. In addition, the relatively low operating frequency of transducers helps lowering the power consumption of the receiver [45, 46]. Let's assume that the RX comprises a Low Noise Amplifier (LNA) and an Analog to Digital Converter (ADC) to interface with the PZT transducer (e.g. Chip 1). In this case, the low operating frequency allows using a very low static bias in the LNA (e.g. a few tens of nA [47]), which leads to a significant decrease

in the front-end power consumption compared to RF systems. The bandwidth of the front-end should be compatible to that of the transducers and the data-rate of the communication. In case a low bit-rate data-exchange among the nodes is tolerable, the bandwidth of the RX can be reduced to save power as well. Moreover, the sampling frequency of the ADC to digitize these low frequency data can be reduced down to the Nyquist limit (a few tens of kHz [45]) to reduce power consumption. The minimum detectable US signal will be determined by the noise of the transducer and the input-referred noise of the front-end, which is a combination of the input-referred noise of the LNA and the quantization noise of the ADC. If the communication link and the RX bandwidth can be reduced, this will decrease the in-band noise and lower the needed power budget to keep a desired SNR level.
The other power-hungry building block in the nodes is the transmitter (TX) used for exciting the PZT transducer. An important bottleneck of US transducers is that they have typically a large parasitic capacitor (e.g. up to a few nF [20]). Thus, when driving US transducers, a large amount of energy is needed to charge and discharge this large capacitor. Although the low operating frequency and the limited data to broadcast allow lowering the instantaneous TX power consumption, this is typically much larger than that of the RX, resulting in an imbalance in power consumption between the TX and RX functions. Due to the relaxed linearity requirement of the OOK scheme, simple and power-efficient TX architectures such as class-D drivers with no static-bias and/or with a power-down state can be used to save power.
The imbalance of the instantaneous power consumption between the TX and RX should be carefully considered in the US system design, specifically in cases where the nodes comprise both TX and RX. This critical system-level trade-off is addressed in the next section, where balancing the RX and TX average power consumption is achieved by exploiting an always-on ultra low-power RX and a duty-cycled TX that is activated only on demand.

2.1.4 Symmetrical US Links

An always-on RX, which can be operated at a very low power (e.g. 8nW in [48]), has been widely used in literature, while transmitters are typically not used in resource-limited nodes. The majority of the applications indeed exploit asymmetrical US links, where the data exchange is performed from a resource-rich master node (e.g. no power constraint and can be placed outside of the environment) to resource-limited slave nodes, which mainly perform receiving and/or sense the presence of incoming US data. In this case, the slave nodes do not send data out via a US up-link, but trigger another (e.g. RF) transceiver for this purpose. Examples of asymmetrical US links include ultra-low power US wake-up receivers used to assist the main RF transceivers [45, 49, 50]. Another example of asymmetric US links can be biomedical implanted devices [18, 46, 51, 52], where the resource-limited implanted nodes are powered by an external master node with no power constraint. These applications favor US for the RX functions, as the US receivers can be made ultra low-power. Indeed, asymmetric US links allocate different power budget to the resource-rich and

resource-limited nodes.
In this thesis, contrary to the prior-art discussed above, a symmetrical US link has been proposed. This is because each node in the envisioned system has a limited power budget. Our communication (and rangefinder) system cannot use a resource-rich external master node that has an unlimited amount of power [46]. Therefore, a new system design approach to realize symmetrical US links is needed, where the aim is to efficiently use the power in the sensor nodes and perform both RX and TX functions. This requires exploiting a holistic design approach considering both the transmitter and the receiver power in a node.

2.1.5 System Design of Symmetrical US Links

In this section, a system design approach (Fig. 2.2) and a specific example for a symmetrical US link will be presented. More details on this approach can be found in the papers included in Appendices A, C, and D.
An important feature of symmetric US links is to allocate a similar requirement

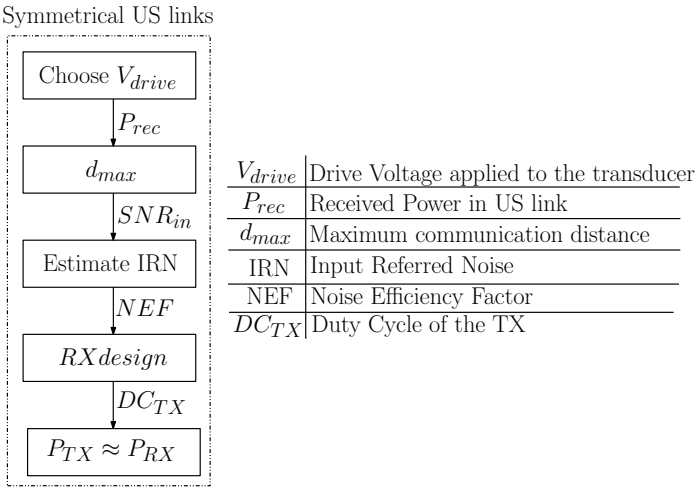

Figure 2.2: A design approach for symmetrical US links.

for the RX and TX functions in terms of average power consumption. The design begins by choosing a commercial US transducer. The same transducer is used for both transmitting and receiving ultrasound signals, where the resonance frequency of the transducer will be used as the carrier frequency. The next step is to choose a drive voltage, V_{drive}, to excite the chosen transducer, as shown in Fig. 2.2. A higher V_{drive} increases the magnitude of the ultrasound waves transmitted at the cost of an increased electrical power consumption. The methodology described in Appendix D exploits a system-level design approach with a holistic optimization of both transmitter and receiver instantaneous power with respect to V_{drive}, which indicates that there is an optimum power consumption for US transceivers. In the context of Appendix A and C, the value of V_{drive} has been chosen identical to the relatively low supply

voltage used in the receiver, aiming to avoid the practical requirement of using many voltage regulators in the system and to reduce the instantaneous power consumption of the TX.
The next step in the system design approach is to characterize the link among the identical transducers by exciting the transmitting one with a burst of square waves of amplitude V_{drive} and recording the electrical power received (P_{rec}) as a function of the distance. Thanks to this system characterization, one can estimate the received power at a desired distance (d_{max}) and the bandwidth among the link built with two identical transducers. The bandwidth will allow to derive the specifications e.g. the suitable frequency range to be used for data-exchange, modulation schemes, etc.
After finding the received power at the desired distance and at the given TX driving amplitude, the noise requirement of the RX can be derived. In this step, a certain level of SNR at the input of the RX should be assigned. Considering the OOK scheme, $\approx 12dB$ SNR is needed [53] to achieve a Bit Error Rate (BER) lower than 10^{-3}. This allows calculating the integrated Input-Referred Noise Density (IRND) requirement of the RX for a given baseband bandwidth. Based on this requirement, the architecture of the RX can be decided. Moreover, the total power in the front-end can be estimated via using e.g. Noise Efficiency Factor (NEF) [54] for the amplifier power consumption and Walden Figure-of-Merit [55] for the ADC power consumption. An important highlight specific to symmetrical links is that a similar power budget is allocated for the transmitter to balance the power used in the nodes. The ratio between RX power and TX power determines the duty cycle needed to equalize the average power spent in the two functions.
The system design example provided in the paper in Appendix A is now discussed. In this case, a $0.6V_{pp}$ V_{drive} and a transducer with a 40kHz resonance frequency [20] are selected. In this example, a resonance frequency of 40kHz has been chosen to save RX power. The outcome of the US link characterization among two identical transducers show that the bandwidth (7.1kHz) and the Q-factor (5.6) of the system are enough to support simple modulation schemes. The received power at 1m distance in air is measured as $-72dBm$ ($56\mu V_{rms}$). Allocating 12dB SNR at the input, the sensitivity requirement can be achieved when the integrated Input-Referred Noise (IRN) of the receiver is around $14\mu V_{rms}$ ($20 \cdot log(56/14) = 12dB$). In this application, an always-on wake-up receiver is needed. To minimize the complexity of the base-band demodulation circuitry, a low-complexity OOK communication scheme with a limited data-rate (e.g $\leq 0.5kbps$) is exploited. This allows allocating a ≈1kHz baseband bandwidth, thus an Input-Referred Noise Density (IRND) of $443\frac{nV}{\sqrt{Hz}}$ for the receiver is estimated, which can be achieved even without an LNA to save power (see Chapter 3). The noise of the transducer is estimated to be around $2.6\frac{nV}{\sqrt{Hz}}$, which is negligible compared to the IRND of the receiver. To balance the RX and TX average power consumption, a suitable duty-cycle ratio (DC_{TX}) (e.g. 0.17% and 2.5% in Appendix A and C, respectively) should be chosen.
The presented approach enables a systematic high-level design flow and provides a method to derive circuit-level specifications (e.g. the input-referred noise, bandwidth, circuit topology, duty-cycle, etc.) suited for symmetrical ultrasound links.

2.2 US Rangefinder Systems

This section will describe system-level challenges when implementing US rangefinder systems and discuss novel rangefinder systems proposed in this thesis to enable distance measurements among sensors nodes in a swarm.

2.2.1 Aim of US Rangefinder Systems

The goal of the Phoenix project is to gather data on the shape and dimensions of enclosed volumes explored by a swarm of sensor nodes. The resource-limited nodes cannot communicate with the outside world. As a result, the nodes need to determine their relative positions while traversing the environment [10, 13–15, 56]. Once the nodes are recuperated, these data are extracted from the nodes and their trajectories during the exploration are reconstructed in offline post-processing [13, 15] to build a map (e.g. shape and dimensions) of the enclosed volumes traveled.

Fig. 2.3 illustrates an example snapshot taken during the travel of the nodes,

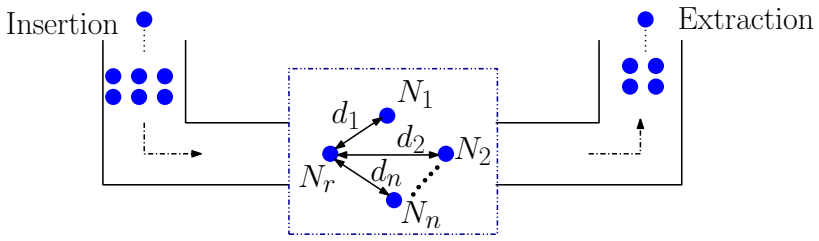

Figure 2.3: An illustration of a distance measurement among sensor nodes.

where the node denoted as N_r performs a distance measurement to determine its relative distance, $d_{1,2..n}$, to other surrounding nodes, $N_{1,2,..n}$, respectively. A node that initiates the distance measurement is named ranger node. Thus, by performing the distance measurement, the ranger node would like determine its relative distance (e.g. $d_{1,2..n}$) to surrounding nodes and gather identification (ID) payloads [13,14,56] of these surrounding nodes (e.g. $N_{1,2,..n}$). Ideally, each node in the swarm can become a ranger node and initiate the distance measurements. For this purpose, the rangefinder system design involves the following steps:

- Define a distance measurement method: The method of distance measurement describes how each node will determine its relative distance to other nodes in the swarm. For instance, Time of Flight (ToF) or Received Signal Strength Indicator (RSSI) can be given as examples of distance measurement methods. The former method is based on measuring the round trip time of US going back and forth among the nodes, while the latter method depends on measuring the distance dependent attenuation of US among the nodes. The candidate methods suited for our applications will be discussed in more detail in the following section.

- Define an implementation principle of the distance measurement method: After choosing a suitable distance measurement method, its implementation principle should be carefully considered in the rangefinder system design. For instance, the majority of the existing ultrasound rangefinder systems are based on the Time of Flight (ToF) method. The implementation principle of the ToF method can be realized by operating the rangefinder system either in Pulse Echo (PE) [57] or Continuous Wave (CW) [58] mode, as will be discussed in more detail in the following sections. These approaches are based on detecting the round trip time of US echoes reflected from passive reflectors, which makes them difficult to directly use for sensor nodes operating in an enclosed volume. Therefore, new implementation principles enabling sensor nodes to gather their relative distance (e.g. $d_{1,2..n}$), distinguishing other nodes from passive reflectors, are needed. This requires a design of an energy-efficient two-way communication link among the nodes (including details on the type of signal to be used during the measurements, modulation schemes, frequency of operation, hardware implementation, etc.), and a distance measurement method to find the relative distances (e.g. Time of Flight).

- Define a distance measurement protocol (e.g. ranging protocol): The protocol is an algorithm enabling the swarm to control the distance measurements. The protocol used in rangefinder systems deals with the organization of the nodes during the distance measurement. For instance, the protocol determines which node initiates the distance measurement and which nodes respond back. In addition, focusing on the synchronization among the nodes should be pointed out in the protocol. Specifically, to avoid a global synchronization among the nodes, which is too power hungry to achieve [25], it is desired that the initiation of the distance measurements can be controlled autonomously by each node, based on a simple algorithm.

In the next section, a general introduction and comparison of ultrasound distance measurement methods suitable for the context of this work will be given. The two sections after that will deal with implementation challenges of rangefinder systems in enclosed volumes and investigate advantages and disadvantages of the existing rangefinder systems. Finally, Section 2.2.5 will introduce novel rangefinder systems proposed to address the specific aims of this thesis. As discussed in Chapter 1, the term rangefinder system has been used to combine the method of distance measurement, the embodiment of the distance measurement method, and the distance measurement protocol into one word, to simplify the explanation.

2.2.2 Distance Measurement Methods

After the sensor nodes are injected into the volume, human intervention during the exploration is not possible. In addition, considering the restricted propagation of RF signals in the environments to be explored, the nodes will not be equipped with GPS.

In literature [13, 23, 24], most of the underwater sensor networks exploit a beacon, a node at known coordinates which has the capability to communicate with the outside world and the other sensor nodes. This is not suited for the applications considered in this thesis. Therefore, the sensors need to perform distance measurements autonomously inside the volume to explore.
The distance measurement methods that are based on Received Signal Strength Indicator (RSSI) require pre-knowledge of the attenuation characteristic of US waves, which highly depends on the operating medium and environmental parameters like temperature and salinity. This results in a large error (e.g. more than 25% [59]) in the distance measurements. Time of Arrival (ToA) based distance measurement methods rely on the knowledge of the exact time that a signal is transmitted and the exact time that the signal is received, thus require a network synchronization, either to a single node in the swarm [36] or to an external hub [25], together with highly stable timing sources (such as atomic clocks) or advanced MAC protocols [26] that require exchanging several data packets. These approaches are too power hungry for our applications. Thus, distance measurement methods that can enable both mutual communication and distance measurements, while avoiding a global synchronization in the network, are desired.
The Time Difference of Arrival (TDoA) based distance measurement methods in fluids exploit different propagation speeds of US and RF and the time difference of arrival of these signals, thereby can be used for only short distances due the attenuation of RF in liquids [33]. Typical US distance measurement methods exploit Time of Flight (ToF) of US. ToF based rangefinder systems are widely used in literature e.g. in medical imaging [40, 60] or other emerging US applications such as fingerprint sensors and gesture recognition systems [61, 62]. Indeed, ToF is a well-established ranging method for measuring the distance between e.g. a sensor and a passive reflector, which is based on recording the round trip time of US going back and forth. As long as the speed of US in the medium is known, the distance between the sensor and reflector can be calculated. Moreover, no propagation signal other than US is needed, and compared to ToA, ToF uses the round trip time and eliminates the need for the knowledge of the exact time that a signal is transmitted, thus does not require a precise synchronization in the swarm. For these reasons, ToF based US distance measurement methods can be utilized in the go-with-the-flow applications considered in this thesis as well. In this case, however, new system level challenges will occur when building rangefinder systems for sensor swarms.

2.2.3 Implementation Challenges of US Rangefinders in Enclosed Volumes

In Section 2.1, system-level challenges towards building energy-efficient US links have been discussed, and the main problem has been identified in the need to minimize the power consumption of the nodes. However, due to collisions and multipath phenomena, the performance and robustness of US links will be effected when a large number of nodes performs the distance measurements in enclosed environments.

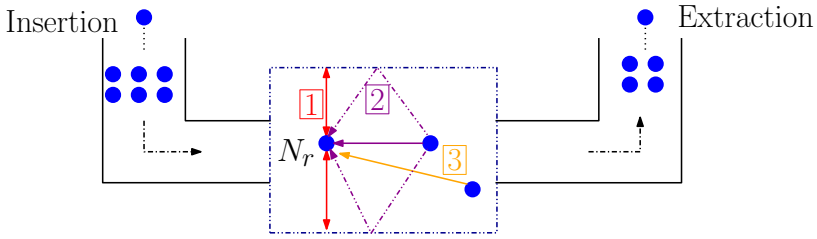

Figure 2.4: An illustration of system-level challenges.

There are three main system-level challenges of rangefinder systems for sensor swarms when the nodes are operated in an enclosed volume, as discussed here below:

1. When a ranger node (e.g. N_r in Fig. 2.4) transmits an ultrasound signal to the environment to initiate a distance measurement, it receives interference due to echoes generated by the boundary of the volume or from other passive reflectors residing in the environment. As the aim of the rangefinder system is to determine the distances among the nodes, the echoes from the passive reflectors should be considered as interferers. Thus, the ranger node should be able to distinguish its own echoes from possible responses of other nodes in the environment.

2. When a ranger node initiates a distance measurement, it expects to receive only one response signal from a surrounding node due to the two-way nature of the desired communication and distance measurement. However, the small size of the operating environment results in multipath propagation of the response signal, as shown in Fig. 2.4, which can interfere with the original response. This means that, in addition to the original response, delayed and reflected versions of the original response reach to the ranger node N_r. As a result, the ranger node should be able to cope with multipath propagation of the responses from the surrounding nodes.

3. A ranger node might receive several responses from different nodes. These responses can overlap (in time) when arriving to the ranger node, as depicted in Fig. 2.4. Therefore, the ranger node should be able to distinguish the responses provided by different nodes in the swarm.

2.2.4 Implementation of ToF based US Rangefinders

ToF based US Rangefinders are used to measure the distance between e.g. a sensor and a passive reflector. Fig. 2.5a shows basic building blocks for a US rangefinder operated in Pulse Echo (PE) mode [38, 60–64] and Fig. 2.5b illustrates its operation in the time domain. A TX drives an ultrasound transducer (e.g. via a relatively short

pulse or a pulse train) to broadcast a US signal from the sensor. This signal propagates through the environment, where it gets reflected from e.g. a passive reflector. This reflected signal is called an echo and is received via e.g. an amplifier (AMP) in the sensor. If the speed of ultrasound, c_{US}, in the medium is known, one can easily calculate the distance R between the sensor and a passive reflector, using the formula shown in Fig. 2.5b, by recording the round trip time τ_d of the US signal.

Using US rangefinder systems in PE mode for sensor swarms would be very chal-

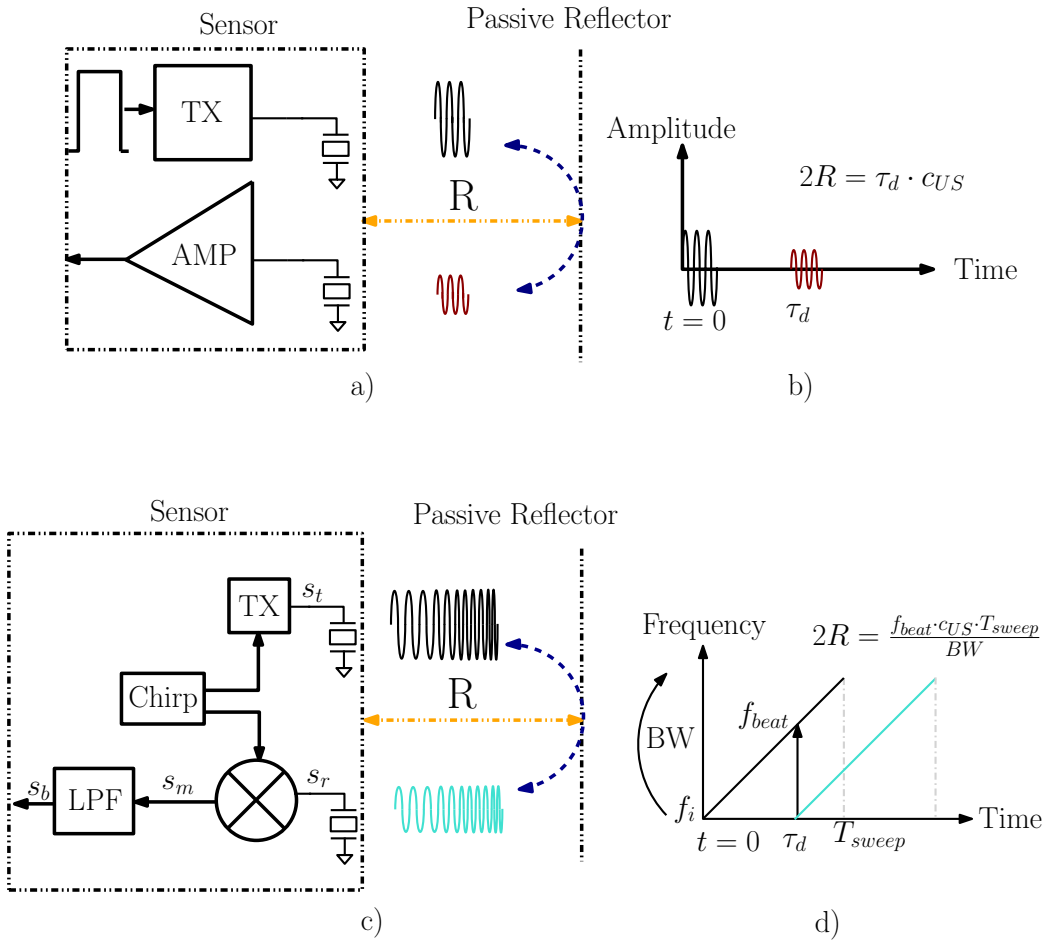

Figure 2.5: a) Implementation of the conventional PE method b) Illustration of the ranging in a Amplitude vs Time plot. c) Implementation of the conventional FMCW method d) Illustration of the ranging in a Frequency vs Time plot.

lenging. This is mainly because collisions and multipath propagation of the echoes experienced when the nodes are operated in an enclosed volume [21] increase the complexity of extracting distance information from the measurements and decrease the accuracy of reconstructing the geometry of the explored volumes. Clearly, distinguishing the echoes is not an easy task considering that they can be originated from the boundary of the volume or can be the response from another node. Moreover, collisions that are likely to happen during the distance measurements among several

nodes further limit the performance of US rangefinder systems.
Alternatively, US rangefinders can be operated in a Continuous Wave (CW) mode [58, 65–70], where typically Frequency Modulated Continuous Waves (FMCW) are used to measure the distance between the sensor and passive reflector, as shown in Fig. 2.5c. In this case, the frequency of the transmitted US signal changes over time e.g. is swept in a bandwidth around the resonance frequency of the transducer, producing a "chirp" signal that is broadcasted and used to down-modulate the received echoes. In case of PE, the transmitted signal and the received echo are separated in time domain, whereas in case of FMCW, the transmitted signal and the received echo are processed simultaneously (Fig. 2.5d). Although both approaches are based on ToF, the round trip time τ_d of the echo signal in the FMCW method is observed as a peak in the baseband, which is a function of the distance R. As will be elaborated in more detail in the following sections, this property is useful for distinguishing the signals overlapped in time domain. FMCW can also be exploited for the data-exchange and distance measurements within sensor swarms [71]. More details on FMCW implementations, and novel implementations of FMCW especially designed for the go-with-the-flow measurement scenario are discussed in the following subsections.

2.2.4.1 Conventional FMCW Method

The basic building blocks needed to implement the conventional FMCW method [67] are shown in Fig. 2.5c. Two US transducers of the same type and resonance frequency are used. A transmitter (TX) and a receiver employing a mixer and a low-pass filter (LPF) are needed to broadcast and receive the US signals, respectively. The operation is depicted in Fig. 2.5d, where a chirp, a signal with a linearly changing frequency in time, is transmitted, and its reflected echo from a passive reflector is received after a time τ_d. The frequency of the transmitted signal at any given time t can be expressed as

$$f(t) = f_i + c_r \cdot t, \quad \forall t < T_{sweep} \tag{2.1}$$

where f_i is the initial frequency of the chirp and c_r is called the chirp rate, which is given as $c_r = \frac{BW}{T_{sweep}}$. Here, BW is the chirp bandwidth and T_{sweep} is the sweep time of the chirp. Accordingly, the phase of the transmitted signal can be written as

$$\begin{aligned} \phi_t &= 2\pi \int_0^t f(t) \cdot dt \\ &= 2\pi \cdot (f_i \cdot t + \frac{c_r \cdot t^2}{2} + \phi_0), \end{aligned} \tag{2.2}$$

where ϕ_0 is the initial phase at $t = 0$ and can be assumed as 0 for simplicity. The echo chirp will be a delayed version of the transmitted signal, where the delay, τ_d, is corresponding to the round-trip time between the sensor and the passive reflector. As a result, we can write the transmitted signal, s_t, and the received echo signal, s_r, as follows:

$$s_t = \cos 2\pi (f_i \cdot t + \frac{c_r \cdot t^2}{2}) \tag{2.3}$$

$$s_r = \cos 2\pi (f_i \cdot (t - \tau_d) + \frac{c_r \cdot (t - \tau_d)^2}{2}). \tag{2.4}$$

These signals will be mixed at the receiver. The signal at the output of the mixer, s_m, can be expressed as

$$\begin{aligned} s_m &= s_t \cdot s_r \\ &= \cos 2\pi (f_i \cdot t + \frac{c_r \cdot t^2}{2}) \cdot \cos 2\pi (f_i \cdot (t - \tau_d) + \frac{c_r \cdot (t - \tau_d)^2}{2}). \end{aligned} \tag{2.5}$$

The equation above can be decomposed into two parts by using the trigonometric equation of cosine multiplication. The first one is the sum term that will be filtered out after the LPF. The other term is the difference term, which is called beat signal, s_b. It can be written as

$$s_b = \cos 2\pi \underbrace{(f_i \cdot \tau_d + c_r \cdot \tau_d \cdot t - \frac{c_r \cdot \tau_d^2}{2})}_{\phi_b}, \quad \tau_d \leq t \leq T_{sweep} \tag{2.6}$$

where ϕ_b denotes the phase of the beat signal. The frequency of the beat signal, f_{beat}, can be calculated as

$$\begin{aligned} f_{beat} &= \frac{1}{2\pi} \cdot \frac{d\phi_b}{dt} \\ &= c_r \cdot \tau_d \\ &= \frac{BW \cdot 2R}{T_{sweep} \cdot c_{us}}, \end{aligned} \tag{2.7}$$

where R is the distance to the passive reflector and c_{US} is the speed of US in the medium. Therefore, we can conclude that the spectrum of the signal obtained via mixing the transmitted and received chirps will show a frequency peak, f_{beat}, corresponding to the round trip time of the transmitted signal. As a result, the distance to the passive reflector can be estimated knowing c_{US}, BW, and T_{sweep}.
Let's imagine that one of the multipaths of the transmitted signal bounces back from the passive reflector and interferes with the original echo. This interference signal together with the original echo will be mixed at the receiver. We conceptually illustrate this situation in Fig. 2.6a, where the signal shown in red shows this interference, assuming that it will arrive at the receiver after a round-trip time of τ_{dm}. The spectrum of the resulting signal after mixing will show two frequency peaks, f_{b1} and f_{bm}, corresponding to the desired echo and its multipath interference, respectively. Despite the fact that these signals are overlapping in the time domain, their corresponding beat frequencies are separated in the frequency domain, thus the interference can be distinguished in the spectrum.
The range resolution is defined as the minimum distance between two reflectors that can be distinguished by the rangefinder system [66]. Considering that the rate of change of f_{beat} is bounded by the repetition time of the chirp ($\Delta f_{beat} \geq 1/T_{sweep}$), the range resolution is given as [72]

$$\Delta R = \frac{c_{US}}{2BW}. \tag{2.8}$$

Assuming that there are multiple passive reflectors present in the environment that are separated by more than ΔR, the echo signals that bounce back from these objects will all be mixed at the receiver. This situation is depicted in Fig. 2.6b, where the

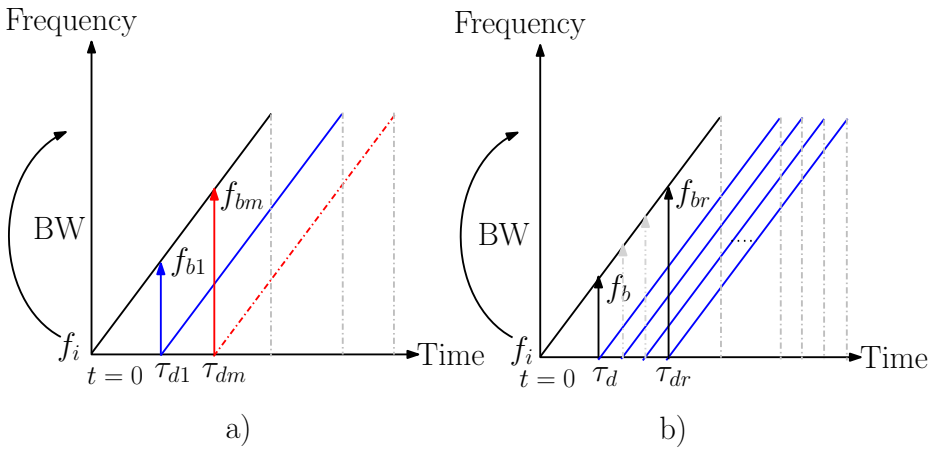

Figure 2.6: a) Illustration of the separation of the multipath from the original echo. b) Illustration of the ranging when there are multiple objects present.

echo chirps coming from the multiple reflectors can be seen. Their corresponding beat frequencies, $f_b, ..f_{br}$, will be separated in the frequency spectrum and thus the reflectors can be distinguished. Although we assume in this thesis that the nodes are traversing the volume to explore with a similar velocity, in case the Doppler effect is to be considered, the conventional FMCW method can be used again. Instead of transmitting the signal with a linearly increasing frequency in time, a chirp that has a sawtooth (up and down) frequency change in time should be used for estimating the relative distance and the velocity of the nodes. More details can be found in [73]. In conclusion, the conventional FMCW method uses the echoes reflected from objects in the environment and provides a distance measurement method for these objects. This method could be adopted for distance measurement in the go-with-the-flow approach. In this case, each node in a swarm would perform the distance measurement independent from each other. Thus, no synchronization would be needed. As discussed in this section, echo collisions from different objects at the input of the nodes can be processed as long as they are separated more than the range resolution. However, the main drawback is that the echoes from the boundary of the volume and the echoes reflected from the surrounding nodes in the volume (if any) cannot be distinguished. Similarly, the echoes reflected from the nodes and the echoes due to another transmit signal of a nearby node cannot be distinguished. As we would like to find only the distances between each node and the surrounding nodes while avoiding the echoes from the boundary of the environment, alternative methods better suited for this task are proposed in the following two sections.

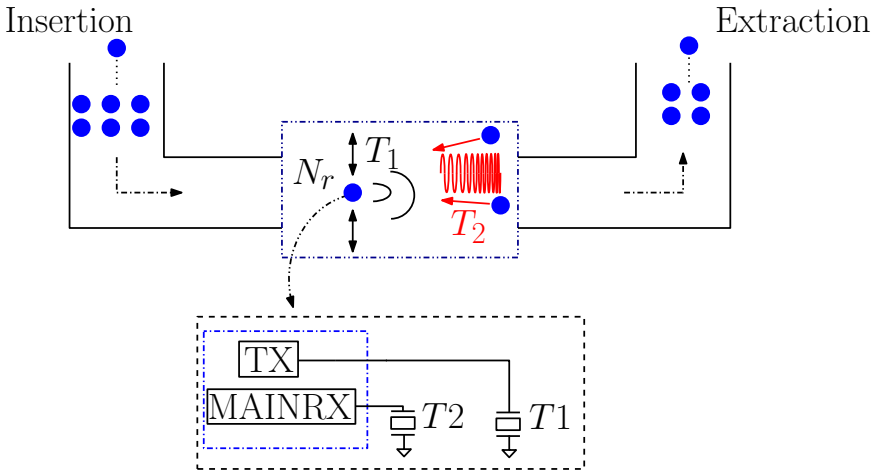

Figure 2.7: a) Illustration of the Frequency Division Duplexing FMCW (FDD-FMCW)

2.2.5 Rangefinder Systems based on FDD-FMCW

Frequency-division duplexing (FDD) is a technique that exploits a different operating frequency band for the transmitter and receiver [74]. As will be explained in this section, when an FDD-like technique is combined with FMCW, it enables the sensor (e.g. the ranger node) to distinguish between echoes from its own transmitter, and responses from other nodes. This is illustrated in Fig. 2.7, where the sensor nodes use two different transducers, T_1 and T_2, to enable frequency division duplexing during a distance measurement. The basic building blocks needed by a sensor node in the swarm are shown in Fig. 2.7, where each sensor node is equipped with two transducers (T_1 and T_2), a ranging receiver (MAINRX) and a transmitter (TX) suited for receiving and broadcasting FMCW US data. One of the key requirements is that the operating frequency bands (and thus the resonance frequencies) of the transducers T_1 and T_2 are different from each other. These transducers can be switched to either TX or RX.
The proposed FDD-FMCW based distance measurement methods are modified versions of the conventional FMCW method that was discussed in the preceding section. The aim is to exploit the advantages of the FMCW method with respect to collision and multipath phenomena while enabling the sensor node initiating the distance measurement to distinguish between passive echo reflections and answers from other nodes in the swarm. Accordingly, the FDD-FMCW distance measurement methods have the following characteristics:

- The sensor nodes in the rangefinder systems are able to support two configurable operating modes. The first operating mode is called ranger mode, where a node aims to find its relative distance to surrounding nodes. When the ranger node initiates the distance measurement, it transmits a signal via transducer T_1, as shown in black in Fig. 2.7. The second operating mode is called the active-tag

mode. The nodes operating as an active-tag listen to the incoming signals via T_1, and transmit back a response signal via T_2, which is shown in red in Fig. 2.7.

- The distance measurement is performed by means of a two-way ranging. First, the ranger node initiates the ranging by broadcasting a request signal via T_1. An important highlight is that the response signals coming from the active-tags are US frequency-modulated continuous waves (FMCW) broadcasted via T_2. As the operating frequency bands of T_1 and T_2 do not overlap, the ranger node can distinguish its own echoes from the responses generated by other tags.

- The ranger node deals with active responses rather than reflected echoes. Therefore, the US signal going back and forth is attenuated by a factor proportional to $\approx R^2$, which is less compared to the attenuation proportional to $\approx R^4$ experienced in the conventional echo based systems. This property is attractive, as it enables lowering the power needed to transmit and receive US signals.

- In case multiple sensor nodes that are at different distances transmit a response, these signals will correspond to different beat frequencies that are separated in the frequency domain, and can be distinguished during post-processing [67]. Furthermore, identification (ID) payloads of the surrounding nodes can be embedded in the response signals, e.g. by amplitude modulation [75] or phase modulation [71]. In this way the ranger can distinguish between the first response by a node and possible delayed version of the same signals due to multipath propagation [67]. In case the distance of a node is equal to the multipath distance to another node, these nodes cannot be distinguished. In actual applications, the loss of information due to these kind of collisions can be compensated by increasing the number of iterations of the exploration.

- The configuration of the operating modes (ranger or active-tag) can be implemented digitally with a negligible effort. From the hardware perspective, the transducers can be routed to either TX or MAINRX with switches that can be activated/deactivated digitally. From the ranging protocol perspective, the nodes can be configured based on an algorithm [13] embedded inside e.g. a digital backend. Furthermore, the initiation of the distance measurement does not need a global synchronization among the nodes, but is simply controlled by the ranger node. Ideally, the active-tags respond instantaneously, therefore, the system does not depend on the synchronization of the active-tags and can be activated anytime by a ranger node.

Both of the rangefinder systems proposed in this thesis are based on the FDD-FMCW approach. As a result, they have similar system-level architectures as elaborated above. The difference between the proposed rangefinders is in their specific implementation. The following two subsections provide more details of each specific approach.

2.2.5.1 An FDD-FMCW based Rangefinder System with a Chirp Exchange

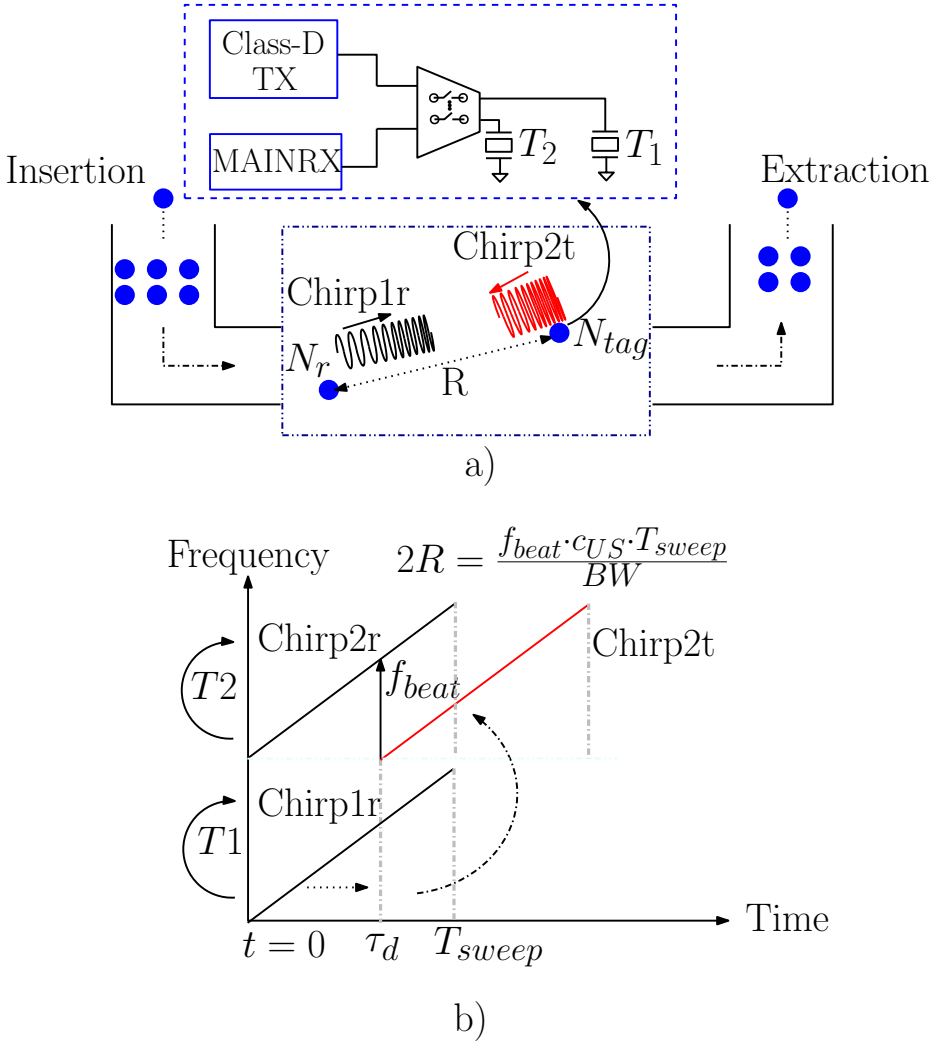

Figure 2.8: a) Concept of an FDD-FMCW based rangefinder system with a chirp exchange and basic building blocks of a node. b) Illustration of a chirp up-mixing.

The first type of the FDD-FMCW based rangefinder systems proposed in this thesis is presented in this section. This system is based on exchanging (properly designated) chirp signals among the nodes that can be configured to be e.g the ranger mode or active-tag mode. Fig. 2.8a visualizes the proposed concept by demonstrating a distance measurement being performed among a ranger node (N_r) and an active-tag (N_{tag}) at a distance R. As will be described in more detail in Chapter 3, the building blocks of these identical sensor nodes comprise a transmitter (e.g. two-level multiplexer-based Class-D TX (see Chapter 3)), a ranging receiver (MAINRX), and two transducers (T_1 and T_2). One can appreciate the FDD-FMCW method, thanks to the different frequencies of the signal sent by the ranger node and the signal sent

back by the active tag. Thus, the ranger node can distinguish echoes coming from passive reflectors from signals sent back by active tags, as discussed in the preceding section.

The principle of the proposed method (see also paper included in Appendix B) can be explained as follows: The ranger node N_r generates two Chirp signals, Chirp1r and Chirp2r. Chirp1r fits the bandwidth of T_1, and Chirp2r fits the bandwidth of T_2, which do not overlap. Chirp1r is broadcasted via T_1, and reaches the other node N_{tag} that is operating as an active tag, as shown in Fig. 2.8a. N_{tag} receives Chirp1r and modulates it to the same frequency band of Chirp2r, generating a signal named Chirp2t. This signal is sent back using T_2 and reaches the ranger node N_r, where it is multiplied by the original Chirp2r. As shown in Fig. 2.8b, the resulting spectrum, similar to the conventional FMCW method, will have a frequency beat corresponding to the round trip delay τ_d between the nodes. This can be easily understood, as the beat frequency will not depend on the frequency shift introduced by the modulation to both signals Chirp2t and Chirp2r. As a result, with knowledge of the bandwidth (BW) and the duration (T_{sweep}) of the Chirps, as well as the speed of US (c_{US}) in the medium, the distance R to the active tag can be calculated. In this method, e.g. up-modulating the chirp can be implemented in the digital domain by XORing the digital output of the tags with a fixed frequency signal generated in the tags (see Appendix B).

Fig. 2.9 illustrates another interesting embodiment of the FDD-FMCW based

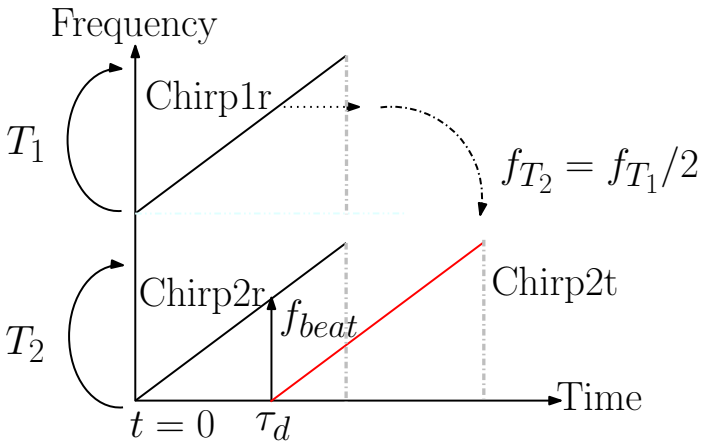

Figure 2.9: Illustration of the Harmonic FMCW method with a chirp division by two.

rangefinder system with a chirp exchange, where the resonance frequencies of T_1 and T_2 have a harmonic relation with each other. In this case, if the resonance frequency of T_1 is f_{T_1} and the resonance frequency of T_2 is f_{T_2}, N can be defined equal to $\frac{f_{T_1}}{f_{T_2}}$. Similar to the general case, the ranger node generates and broadcasts Chirp1r, and at the same time it generates Chirp2r, which is in the same harmonic relation to Chirp1r as f_{T_2} to f_{T_1}. Chirp1r has thus at each moment N times the frequency of Chirp2r and matches exactly the frequency range of the response generated by the active tag. The example depicted in Fig. 2.9 shows the case when Chirp2r is obtained

by simply dividing Chirp1r by two, thus N=2 [28]. The operation of division by an integer is simple to implement e.g. in the digital domain, and is compatible with the method described here, providing an efficient and hardware minimal way to embody the FDD-FMCW based rangefinder with a chirp exchange.
The rangefinder methods with Chirp exchange presented in this section satisfy the goals discussed in Section 2.2.1, while addressing the system-level challenges introduced in Section 2.2.3 and are thus suited for applications of the go-with-the-flow approach. As will be elaborated more in Chapter 4, an implementation of this distance measurement method based on custom ICs and commercial US transducers (see Appendix B) can achieve $2.7\mu J$ energy consumption per distance measurement with a 6.5mm range resolution up to 1m distance in air, which is in-line with the best state-of-the-art.

2.2.5.2 A Rangefinder System with a Wake-up Based FDD-FMCW

The second type of the FDD-FMCW based rangefinder systems proposed in this thesis is called a Wake-up Based FDD-FMCW and is presented in this section.
This rangefinder system aims to improve the performance obtained by the previous rangefinder system by addressing the following challenges:

- Lower the always-on power consumption of the nodes: As discussed in Section 2.1, energy-efficient US links can be achieved combining an ultra low-power always-on receiver with a duty-cycled transmitter that works only on demand. This feature can be applied to US rangefinder systems as well, specifically suited to the case when a node operates as a tag. According to this idea, the tag keeps only its receiver continuously on, to listen to the environment, and transmits a response chirp only when requested by a ranger node. Thus, when a node operates as a tag while exploiting an ultra low-power receiver, the active power consumption per node can be greatly reduced.

- Decrease the energy consumption per distance measurement: Further power saving could be possible if the ranger node can transmit a very short message, e.g. a few bits with a duration much shorter compared to the duration of the chirps T_{sweep}, to activate (wake-up) the tags and request them transmitting their response. This would enable lowering the transmission power needed for the signal broadcasted by the ranger node.

- Simplify the generation of chirp signals: Although the processing of the chirps in the tags by means of dividing or XORing with a fixed frequency in the digital domain can be done easily, it still costs in terms of power consumption and increases the complexity of the hardware needed. Alternatively, the chirps needed in the distance measurement can be digitally synthesized by reading at a constant rate suitable bit streams stored in a memory. Since the initial frequency, the stop frequency, and the duration of the response chirps are known apriori at system-level to fit inside the BW of transducers, the bit streams

needed to synthesize the chirps can be generated offline (e.g. in MATLAB) and preloaded to a node. Thus, the ranger node and active-tag do not need to modify the chirps, and whenever needed during the ranging, can synthesize their own chirp by reading a memory. Clearly, the clocks needed for digital synthesis in the ranger node and the tags should be sufficiently synchronous during the time T_{sweep}. This requirement can be easily achieved, considering the relatively short duration of T_{sweep}, which is typically in the order of milliseconds.

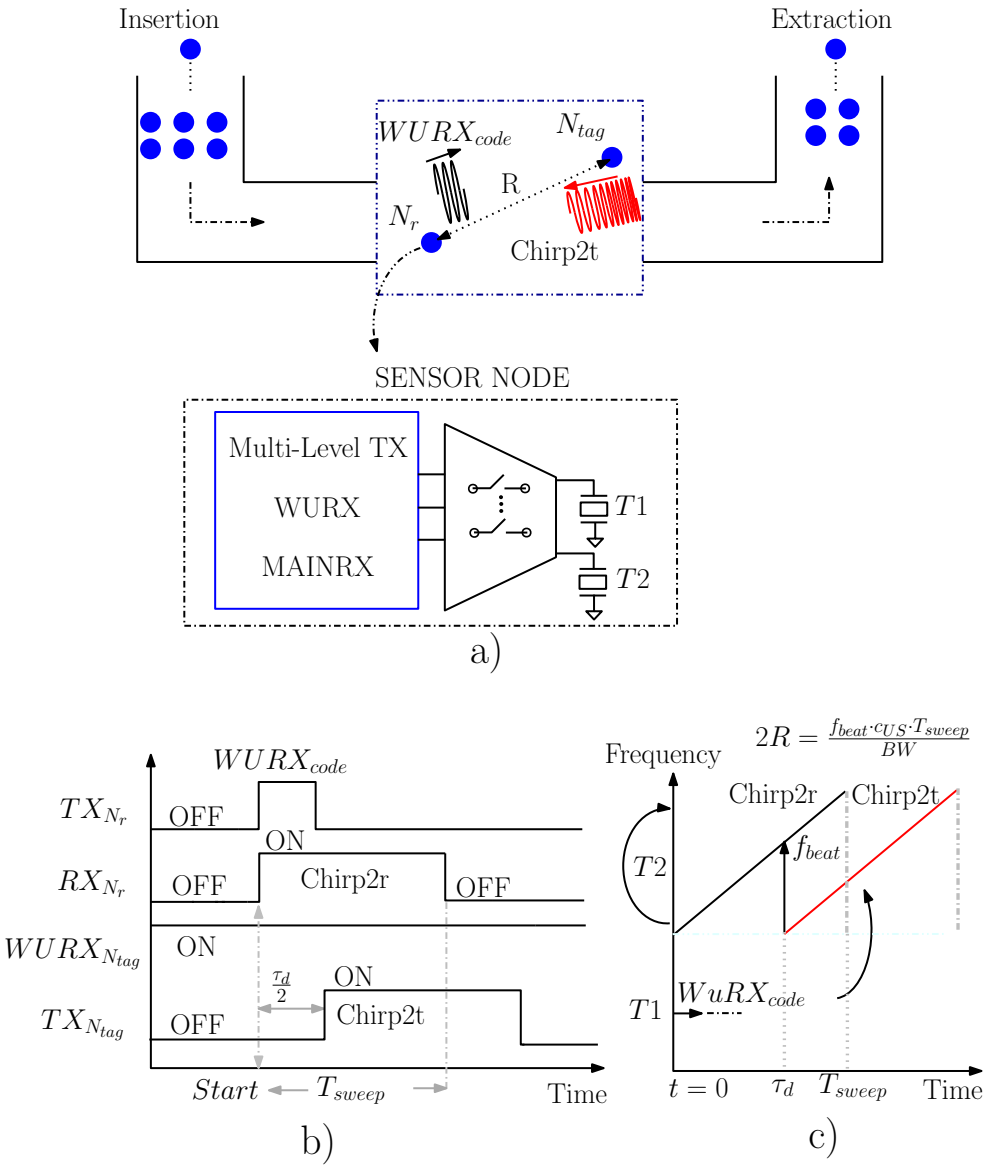

Figure 2.10: a) The concept of a rangefinder system with a wake-up based FDD-FMCW and basic building blocks of a node. b) Time diagram of the principle of the distance measurement. c) Illustration of the principle in Frequency vs Time axis.

Fig. 2.10a demonstrates an example of a new rangefinder system that answers all

the described challenges. The building blocks of the nodes consist of two transducers (T_1 and T_2), a transmitter (e.g. Multi-level TX (see Chapter 3)), a wake-up receiver (WURX), and a ranging receiver (MAINRX). Similar to the previous rangefinder system, the nodes use two different transducers, T_1 and T_2, which have different resonance frequencies and a separated operating frequency band to enable frequency division duplexing. In this system, the nodes exploit two different receivers. One is called a wake-up receiver (WURX), which is designed to enable ultra low-power consumption. An important feature of this rangefinder system is that the nodes that are operating as a tag activate only their wake-up receiver, while the transmitter and ranging receiver are switched-off. Therefore, power consumption in this mode can be significantly reduced. The other receiver is called the ranging receiver (MAINRX), which is similar to the one used in the previous rangefinder and is activated only during the ranging.
In Fig. 2.10a, a distance measurement between two sensor nodes, N_r and N_{tag} at a distance R, is shown. Here, N_r is the ranger node and starts the distance measurement by broadcasting a $WURX_{code}$ to the environment via T_1. At the same time, N_r activates its ranging receiver to listen to the responses from the nearby nodes. Fig. 2.10b shows the timing diagram illustrating the activation of the corresponding blocks in the nodes. The initiation of the ranger mode is controlled via a Start input generated by the nodes without any need for global synchronization in the swarm. As illustrated in Fig. 2.10b, a digitally synthesized US signal, Chirp1r, is used in N_r as a mixing signal in its ranging receiver, which listens to T_2. Chirp2r (Fig. 2.10c) is a frequency-modulated US signal that fits the bandwidth of T2 and whose frequency increases linearly with time in the interval 0 - T_{sweep}. Meanwhile, N_{tag} is operating as an active-tag. The $WURX_{code}$ reaches N_{tag} after a propagation delay $\frac{\tau_d}{2}$, is received by its T_1 and WURX. If the power of the $WURX_{code}$ captured by N_{tag} is sufficient to wake-up the tag, the TX in N_{tag} is immediately activated to broadcast a response, Chirp2t, via T_2. Chirp2t is a frequency-modulated US signal identical to Chirp2r, which is digitally synthesized by N_{tag}. Similar to the conventional FMCW method, the delay τ_d corresponds to the round trip time of flight between the nodes and equals to $\frac{2R}{c_{US}}$, where R is the distance between the nodes and c_{US} is the speed of US in the medium. Thus, the distance R to the active tag can be calculated by finding the frequency peak at the output of the ranger, f_{beat}.
The Wake-up based FDD-FMCW rangefinder system presented in this section satisfies the goals discussed in Section 2.2.1 as well as the system-level challenges introduced in Section 2.2.3. As will be elaborated more in Chapter 4, an implementation of this distance measurement method based on custom ICs and commercial US transducers (see Appendix A) achieves $1.25\mu J$ energy consumption per distance measurement with a 18.7mm range resolution up to 1m distance in air, which is the lowest energy consumption for an US ranging system demonstrated at the time of writing this manuscript.

2.2.5.3 Digital Processing needed for US Rangefinder Systems

The FDD-FMCW based rangefinder systems proposed in this thesis use the data at the output of the ranger node to perform distance measurements. The spectrum of these data contains the information needed for determining the relative distances. This spectrum is computed by Fast Fourier Transform (FFT), which is implemented outside of the nodes.
An important feature of the go-with-the-flow approach is that most of the digital processing tasks do not have to be performed inside a node, but can be performed off-line, after recuperating the nodes from the environment under test. As discussed in Chapter 1 and Section 2.2.1, at the Insertion point (See Fig. 2.8a and Fig. 2.10a), the swarm of sensor nodes is inserted in the volume to explore. During the exploration, mutual distance measurements are saved in a memory present in each node while the nodes are traversing the volume. These data are collected after recuperating the sensor nodes at the Extraction point. As a result, the post-processing needed to reconstruct the shape of the volume explored, and thus most of the digital computations including the signal processing (e.g. FFT) needed to derive the spectrum of the received data and calculating the distances can be performed outside the environment under test, after the nodes are recuperated at the end of the exploration. As a result, the power overhead for digital processing can be minimized in the actual application. Thus, the only relevant digital component that has not been explicitly included in the system-level discussion is the memory needed to store the data of the mutual distance measurements.
A key parameter to consider for the on-chip memories is their leakage, which increases proportionally with the operating temperature (up to tens of μW). A recent work presented in [76] describes a 1Mb NOR-based flash memory, which features a sleep mode operation with 12nW power consumption at room temperature. This example would suit well the proposed rangefinder systems as it has a sleep (always-on) memory power that is lower than the power consumption of the always-on receivers used in the proposed rangefinders ($23nW$ and $0.56\mu W$, respectively, (see Appendices A and B)). Moreover, the energy needed to write the data needed per distance measurement is negligible compared to the TX energy consumption of both rangefinder systems. Memory approaches as described in [77] even have no leakage power and still feature an energy needed to write (read) the data to (from) the memory that is negligible when compared to the energy per distance measurement reported in this thesis.

2.2.5.4 Clock requirement of FDD-FMCW methods

Considering the fact that the active-tags transmit back their response the moment that they receive the initiation signal from the ranger node, their response are independent of each other and start without any delay. As a result, the system does not depend on the synchronization of the active-tags and can be activated anytime by a ranger node. From a network perspective, a global synchronization in the network

to perform ranging is not needed, and the data stored in each node can be recovered independently from the swarm. Yet, a certain amount of accuracy is needed for both extracting the data from the nodes and for the accuracy of the ranging. During the experimental characterization of this work, all the clocks needed in each node, except the clocks needed in the tags in wake-up mode which are derived from an on-chip clock generator, are provided by an FPGA, and derived from an external 50MHz crystal oscillator on the Xilinx Spartan-3 board. In a full system implementation, an ultra low-power crystal oscillator (e.g. 32kHz) and an integer-N PLL would typically be needed as timing reference. There is no common system clock.
The typical accuracy of crystal real time clocks (RTCs) is sufficient for most of the applications considered in this thesis. The ranging accuracy of the proposed approaches depends on the frequency accuracy of the RTCs used in the ranger node and the tags. A typical frequency accuracy (i.e. the maximum deviation from the nominal crystal frequency) for RTC crystals is around 100ppm [70]. The accuracy of the ranging can be calculated by analyzing the effect on the (short-term) deviation of the nominal frequency of crystals on the beat frequency that is measured by the nodes. The measured beat frequency generated in FMCW has been given as $f_{beat} = \frac{BW \cdot \tau_d}{T_{sweep}}$, where BW is the chirp bandwidth, τ_d is the round trip time, and T_{sweep} is the duration of the Chirp signals. As a result, an inaccuracy on the T_{sweep} and BW would be reflected in inaccuracy of the distance measurement. For instance, using a T_{sweep} of 8ms would result in an FFT resolution of 125Hz, and considering a maximum expected beat frequency of ≈6kHz for a 1m distance in air, an inaccuracy that is lower than 2% on the measured f_{beat} is needed to avoid a resolution loss larger than the FFT quantization error. A 100ppm variation in the nominal frequency of the reference clock would translate an error in the sweep time that is lower than 0.01%, which will not affect in an appreciable way the resolution of the ranging system.
Another aspect to consider is the long-term accuracy of the RTCs. During the exploration, unsynchronized nodes will perform the ranging e.g. within a certain period. Thus, in order to accurately reconstruct the shape of the volumes that the nodes traversed during the exploration, the long-term frequency accuracy of the RTCs has to be taken into account. For this purpose, one can assume that the nodes travel with an average speed of 2.5m/s (a typical velocity e.g. in City water distribution systems is around 2.1m/s [78]) for 3 hours of exploration. This means that a total of 27km would be traveled, which is sufficient for our applications, enabling e.g. to localize a leak in the pipes used for water distribution systems. Long term RTC stability (e.g. drift from the nominal crystal frequency) of $\pm 5ppm$ is given in [70]. Thus, the max. error among the different nodes during the exploration would correspond to $\pm 13.5cm$ error in a 27km pipe. Such error is considered negligible in most of the applications considered in this thesis.

2.3 Conclusion

This chapter deals with system-level contributions proposed in this thesis for US communication and rangefinder systems suited to sensor swarms. In Section 2.1, the main system-level challenges of building energy-efficient communication links for sensor swarms in fluidic environments have been discussed. It has been concluded that US signals fit better to the miniature and low-power applications compared to RF and optical signals because of their relatively low attenuation in liquids. This is followed by a discussion on ultrasound communication links, where the system design approaches considering the type of transducers, modulation schemes, and frequency of operation have been discussed with an emphasis on low-power consumption. To reduce the complexity and lower the active power consumption of the nodes, a low-complexity OOK modulation scheme and a limited data-rate have been chosen. The asymmetry between the transmitter and receiver power consumption has been shown at the system-level. Accordingly, it has been concluded that a holistic design approach to balance the power consumption of the TX and RX functions is required for symmetrical ultrasound links. In Section 2.2, the desired functions of US rangefinder systems suited for the Phoenix project are discussed, where the nodes in a swarm need to perform measurements to find their relative distance. This is followed by describing the main implementation challenges when a swarm of sensor nodes is operated in an enclosed volume and according to the go-with-the-flow approach. These are related to collisions and multipath propagation of the US signals transmitted among the nodes. The Time of Flight is chosen as a distance measurement method as it offers to use only ultrasound signals without synchronization requirement in the swarm. Due to detrimental effects of collisions and multipath propagation of ultrasound echoes in enclosed environments, the existing rangefinder systems systems based on either Pulse Echo or Continuous Wave modes cannot be directly used for the go-with-the-flow approaches. Accordingly, two novel FDD-FMCW based rangefinder systems are proposed. They are based on using separate frequency bands for the ultrasound transmission and reception. The proposed methods make the distance measurement insensitive to the echoes generated by the boundary of the environment being explored and suit well our applications.

Chapter 3

Circuit-Level Contributions

This chapter discusses circuit-level contributions of this thesis, with a detailed focus on the hardware blocks needed in sensor swarms for the US communication and rangefinder systems presented in Chapter 2. The first two sections will deal with common critical interface circuits in the nodes, the low-noise amplifier (LNA) and the transmitter (TX). In addition, this chapter will present the circuit design of the wake-up receiver, which is used in the Wake-up based FDD-FMCW rangefinder system.

3.1 Low-noise Amplifier Design

Low-noise amplifiers (LNA) are used to amplify and condition the electrical signals generated by US transducers. The input-referred noise and the input SNR of the front-end is highly depend on the performance of the LNA (e.g. its gain and noise) and on the interface between US transducer and LNA. As a result, this section will first present the electrical model used for the transducers and then discuss the circuit design of LNAs suited for US transducers.

3.1.1 Transducer Model

The typical equivalent electrical model [62, 63] of piezoelectric US transducers (PZT) used in this thesis is shown in Fig. 3.1a. The series resonator comprising R_m, L_m and C_m models the transducer's mechanic resonance [45]. A large input parasitic capacitor, C_p, represents the dielectric capacitance of the piezoelectric material used in the transducer and added parasitics. The values of the different components in the equivalent model for the transducers T1 and T2 [20] used in this work have been estimated by impedance measurements and are reported in Fig. 3.1a.
When the transducer is used as a receiver, the incoming pressure waves (e.g. ultrasound waves) from the environment result in a mechanical excitation [38] proportional

	$T1$	$T2$
f_r	$40kHz$	$100kHz$
C_p	$2.3nF$	$0.88nF$
R_m	400Ω	434Ω
L_m	$48.6mH$	$23mH$
C_m	$355pF$	$131pF$
Q	29	30

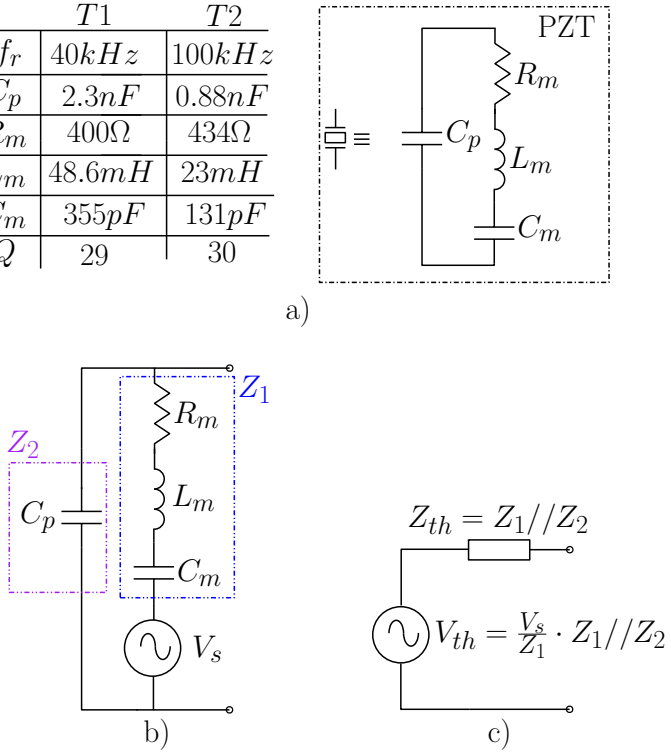

Figure 3.1: a) An equivalent electrical model of the unloaded transducer. b) The electrical model when the transducer is used as a receiver. c) Thevenin equivalent model of the circuit in b.

to the magnitude of the incoming pressure wave. This excitation is modeled by adding a voltage source, V_s, in series to the resonator [38]. Fig. 3.1b and c show the complete electrical model and its Thevenin equivalent circuit, respectively. The impedance of the resonator, Z_1, and the impedance of the parasitic capacitor, Z_2, are in parallel and determine the equivalent Thevenin impedance, Z_{th}. The Thevenin equivalent voltage, V_{th}, is found by multiplying the current due to the mechanical excitation with the equivalent impedance. An important observation can be made at series resonance, where the equivalent impedance of the transducer becomes resistive due to R_m. Thus, $Z_1//Z_2$ becomes equal to $Z_1 \approx R_m$, and thus $Z_{th} \approx R_m$ and $V_{th} \approx V_s$ can be estimated. As a result, in order to sense the voltage V_s without attenuation, a high input impedance voltage amplifier can be used.[1]

3.1.2 LNA design for US interfaces

In case a receiver comprises an LNA in the front-end to interface transducers [79–82], the Input Referred Noise Density (IRND) of the receiver is determined by that of the

[1]We note that in case Z_1 and Z_2 are comparable at resonance, as in the case for most CMUTs, one can model the mechanical excitation with a parallel current source, and sense the current with a low input impedance TIA [64].

LNA, assuming its gain is sufficiently high to make negligible the effect on the input noise of the rest of the front-end, combined with that of the transducer, which can be estimated by using the R_m in the impedance model as the noise source. In addition, the operating frequency band of the LNA has to be compatible with that of the transducer, which might be the highest in the front-end, thus requiring a larger static bias current than the rest of the circuits. For these reasons, this thesis investigates suitable low-power approaches to the LNAs for US interfaces.
The first approach to lower the power consumption of the LNA is to exploit a single-ended architecture due to the single-ended nature of the transducer. Moreover, an inverter-based architecture [79,83–85] can be used as both pMOS and nMOS transistors in the inverter contribute to the total transconductance for a given bias current, improving the current efficiency and thus the Noise Efficiency Factor (NEF). This architecture is called current-reuse amplifier [83] in recent prior-art. Indeed, the inverter-based architecture allows using about half of the needed static bias current compared to that of conventional amplifiers [54] for a similar input referred noise density and gain-bandwidth product (GBW). Although poor PSRR performance of the inverter-based topology is an important drawback, it can be tolerated in our application as we foresee a battery operated system, where the DC voltages will be provided via voltage regulators. Whenever the gain accuracy is not important, inverter-based amplifiers can be operated in open-loop to maximize their gain and reduce the noise contributions of the other blocks of the front-end, e.g. thermal noise of the mixers and quantization noise of the ADCs, to the input-referred noise. An important point in the inverter-based topology is the need to stabilize the output bias point against process variations and mismatches in the biasing networks. In a differential architecture [55], as shown in Fig. 3.2a, the DC output voltage can be stabilized by applying a negative feedback to control the pull-up or pull-down current provided by the transistors in series with the inverter. In this case, the gate voltage of either M_{cp} or M_{cn} can be set by a DC common mode feedback (CMFB) loop [47], improving the robustness of the output common-mode DC voltage against the mismatch between these two current sources and other sources of variation. However, single-ended architectures do not have a virtual ground node for the signal, V_{GND}, connected to the pull-up, M_{cp}, and pull-down, M_{cn}, transistors (Fig. 3.2a) that are providing the needed bias current, thus alternative methods are needed. In previous literature [79, 81, 86, 87], there are several works that focus on inverter-based amplifiers and their bias circuitry, as discussed here below:

- AC ground can be provided via a capacitor [88] placed between the source of M_1 and M_{cp}, as shown in Fig. 3.2b. In this case, M_1 and M_2 build the inverter, while their bias current is provided via M_{cp}, which is controlled via its gate voltage, V_{bp}. However, when this idea is used in a US application, where the operating frequency range is in the order of tens of kHz, the value of the capacitor needed to establish AC ground becomes impractical to integrate.

- Alternatively, the transistors M_1 and M_2 can be AC-coupled to the input, as shown in Fig. 3.2c. Here, the gate voltage of M_1 can be generated via a current

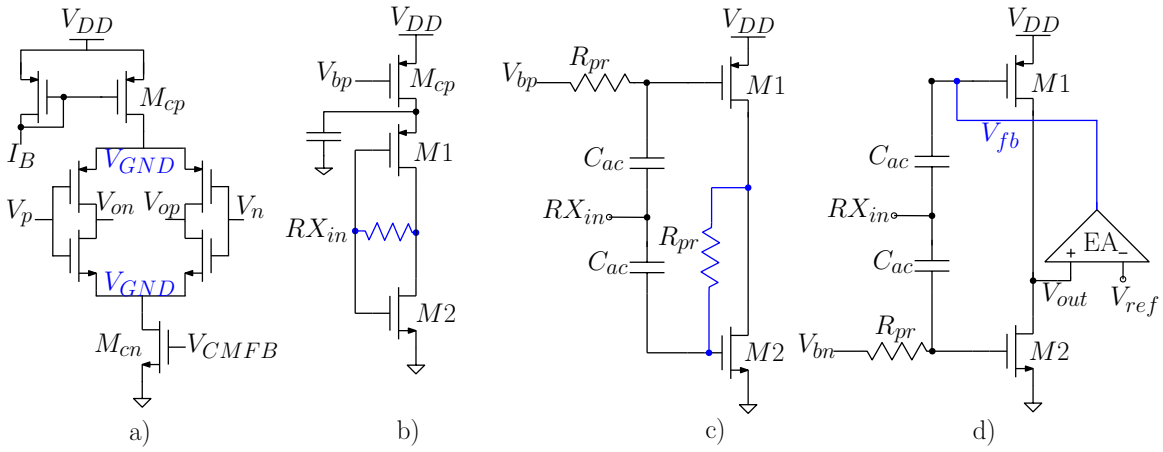

Figure 3.2: a) A differential inverter-based amplifier b) A single-ended inverter amplifier with a pseudo-resistor feedback c) An AC-coupled single-ended inverter amplifier with a pseudo-resistor feedback d) A single-ended amplifier with a DC feedback loop

mirror (setting V_{bp} at a desired voltage) and a series pseudo-resistor R_{pr}. The DC gate voltage of M_2 is provided by a feedback pseudo-resistor that connects the nMOS gate to the output node. With this approach [86], the output voltage is quite sensitive to process, voltage, temperature (PVT) variations. Indeed the DC output is not precisely fixed using an active DC feedback, which would help reducing sensitivity to PVT. A better control of the output DC point to the middle of the supply range is needed e.g. to improve the linearity of the LNAs.

- An active DC feedback loop in order to control the bias of the LNA output is proposed in [60, 86]. This is typically done applying the DC feedback to one of the gates of the transistors belonging to the LNA, e.g. to M_1 as shown in Fig. 3.2d. Although this method precisely controls the DC voltage of the output node, it adds the noise of the feedback network to the LNA input, leading to a decrease in SNR. This problem is solved in [79] by applying a dynamic bias control, however this approach requires pre-knowledge of the timing of arrival of the input signal, which is not available in our applications.

In order to address the above-mentioned challenges, alternative methods are proposed in this thesis, as described here below:

- ***Single-ended inverter with a bulk feedback loop*** As shown in Fig. 3.3a, this method is based on a control loop, where the feedback is applied to the bulk terminal of the pMOS transistor M_1 to control its threshold voltage via the body-effect (Appendix D). The output DC point is compared to a mid-rail reference voltage (V_{ref}) and the error signal is fed back to the bulk terminal by an error amplifier (EA), thereby separating the feedback network from the input of the amplifier. Although this method makes the DC output voltage robust

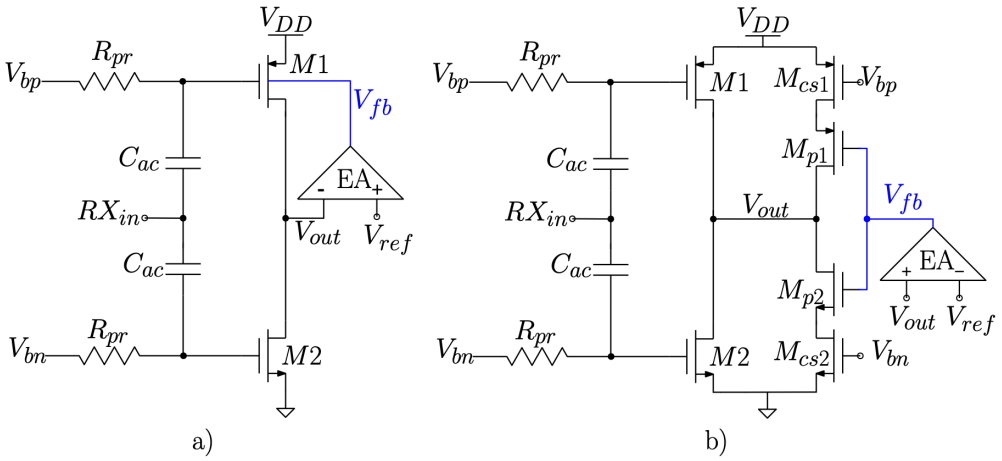

Figure 3.3: a) A single-ended LNA with a bulk feedback loop b) A single-ended LNA with an auxiliary inverter feedback loop.

against mismatch in the biasing network and to voltage drops on the pseudo-resistors due to leakage currents, the proposed method requires higher loop gain compared to the methods in [60, 86] due to reduced bulk transconductance. In addition, a supply voltage that is higher than the one used for the inverter (V_{DD}) is needed for the EA, as the EA DC output voltage level should be around V_{DD}.

- ***Single-ended inverter with an auxiliary inverter feedback loop*** A current starved auxiliary inverter, formed by M_{p1} and M_{p2}, is used in parallel to the main inverter (M_1 and M_2) to stabilize the DC level of the output node, V_{out}, as shown in Fig. 3.3b. The auxiliary inverter is current starved with the transistors M_{cs1} and M_{cs2} to limit its power consumption. M_1 and M_2 are AC coupled to the transducers input, RX_{in}, and these transistors are separately biased. The DC gate voltages of M_1, M_{cs1}, M_2, and M_{cs2} are provided via pseudo-resistors and internal current mirrors. The EA is designed as a differential pair with active load and uses the same supply as the LNA. The gate of the auxiliary inverter is controlled via feedback by comparing V_{out} to a reference voltage, V_{ref}, and feeding back the error signal, V_{fb}, amplified by the error amplifier, EA. The auxiliary inverter, similar to M_{cp} and M_{cn} in the differential topology, can either source or sink a suitable current to the output node, thus keeping the output DC voltage at the desired value. The proposed DC feedback can compensate the errors due to leakage of pseudo-resistors, R_{pr}, and mismatch between the biasing network and the LNA. The transconductance of the auxiliary inverter is much lower than the main inverter. This provides a small DC current, low power, and high output resistance, minimizing the impact of the auxiliary inverter on the LNA gain. Compared to previous works [60, 81, 86, 87], the proposed DC feedback allows the single-ended inverter to work in continuous-time. Besides, it applies the feedback to the output node instead of the LNA input, minimiz-

ing degradation of the SNR. Moreover, the supply voltage of the EA can be the same as the one used in LNA, thus solving the supply level complications of the previous method.

3.2 Transmitter design for US interfaces

The transmitter (TX) is used to drive the transducer to broadcast ultrasound signals to the environment. On the transmitter side, power-efficient class-D buffers without a static bias have been investigated due to their simplistic implementation and considering the relaxed linearity constraints of OOK-like schemes used in US communication systems. The circuit shown in Fig. 3.4a is a two-stage class-D buffer. It consists of a level shifter input stage and 6 cascaded inverting buffering stages. Each stage is tapered by a factor of 7 to drive large capacitive loads (e.g. up to 2nF). In this circuit, thick-oxide transistors have been used together with a separate supply level, V_{DDH}, which can be set higher than the one used for the receiver (V_{DD}). This design choice has been made considering that using a larger driving voltage can further increase the communication distance, or allows coping with mediums like air where the attenuation is larger than in water. The transistors in the inverter at the last stage are designed to avoid voltage division with the impedance of the transducers at their resonance. This architecture allows using a drive voltage up to 3.3V, which is the max. available in a standard 65nm technology, however, suffers from relatively high short-circuit current, decreasing its efficiency.

Alternatively, when a supply voltage VDD_{TX}, that is as low as the one used in the

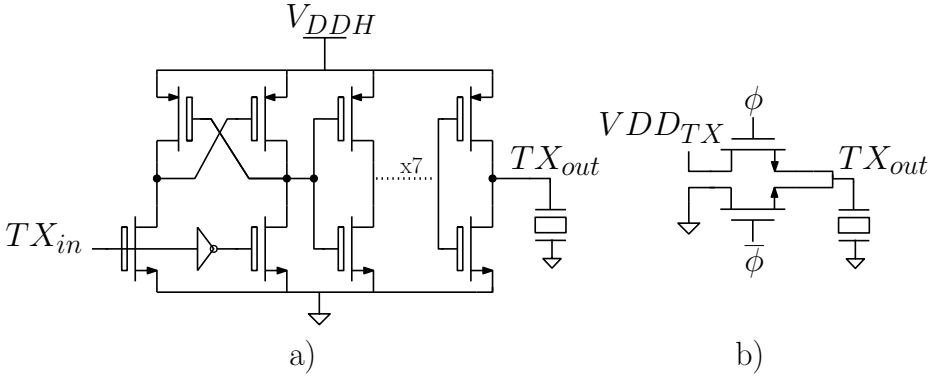

Figure 3.4: Class-D Buffers: a) Level-shifter based buffer b) Multiplexer based buffer

receivers (e.g. 0.6V), can be used to save power, a simple multiplexer as shown in Fig. 3.4b can be exploited to build the TX. This architecture comprises 2 nMOS transistors that connect the desired DC voltage to the transducer load. The switches are designed to avoid voltage division with the impedance of the transducers at their resonance. The period of the driving signal is controlled by activating the non-overlapping clocks ϕ and $\overline{\phi}$, which are distributed to the switch transistors with on-chip buffers

having a separate supply (e.g. can be 1.2V or 2.4V). Thanks to the non-overlapping clocks controlling the switches, the short-circuit conduction can be significantly reduced, improving the performance compared to the previous class-D buffer. When US transducers are driven in resonance, the resistance R_m and C_p are in parallel (Fig. 3.5), and the impedance of the transducer becomes resistive due to R_m. In this region of operation the efficiency of class-D buffers can be very high. It can be approximated by the ratio between the on-resistance r_{on} of the nMOS switches and the resistive load R_m, if the power needed to operate the switches is negligible compared to the output power. However, in US rangefinder systems described in Chapter 2, the transducers

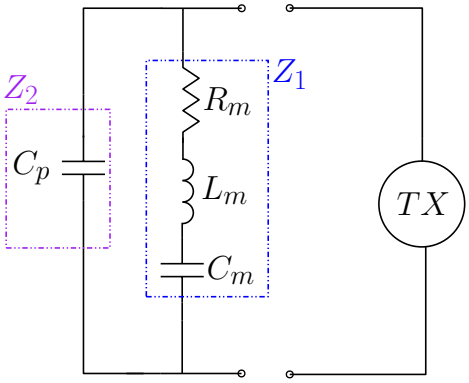

Figure 3.5: The interface between transmitters and US transducers.

are driven mostly outside of their resonance when transmitting a chirp signal. Out of resonance, the equivalent impedance that the TX drives becomes basically capacitive and is equal to C_p. An important bottleneck when interfacing piezoelectric transducers out of resonance, as shown in Fig. 3.5, is the dissipation of a large amount of energy to charge and discharge the large parasitic capacitance C_p. In this thesis, as the miniaturization of the nodes is highly desired, using an inductance (mH range) to cancel out C_p is considered impractical, since it would require large volumes. To reduce capacitive losses, a well-known step-wise charging method [89], [90] has been used in literature. A similar method has been thus chosen here to drive the US transducers, e.g. T1 and T2 as used in Chapter 2. For each transducer, a step-wise charging/discharging using a multi-level driving signal is more energy-efficient than the conventional two-level class-D driving schemes, as discussed here below:

- Multi-level driving reduces the losses associated to charging and discharging the parasitic transducer capacitance C_p. A step-wise charging of a capacitor in N equal steps reduces the energy spent to charge the capacitor to $\frac{1}{N}$ of the energy needed when charging the capacitor directly to the final voltage level [89].
- Multi-level periodic signals have a higher ratio between the energy at the fundamental frequency and the energy in the harmonics. Multi-level driving at the same driving frequency as the two-level driving contains less energy in the harmonics, while having a similar energy at the fundamental tone. For this

reason, multi-level signals can excite more efficiently the resonator branch (Z_1) of the transducer and transform electric energy into acoustic energy when the transducer is excited close to resonance.

To realize an efficient transmitter, thus, a multi-level TX is used in this work, as shown in Fig. 3.6a. The transmitter includes two switched-capacitor converters and

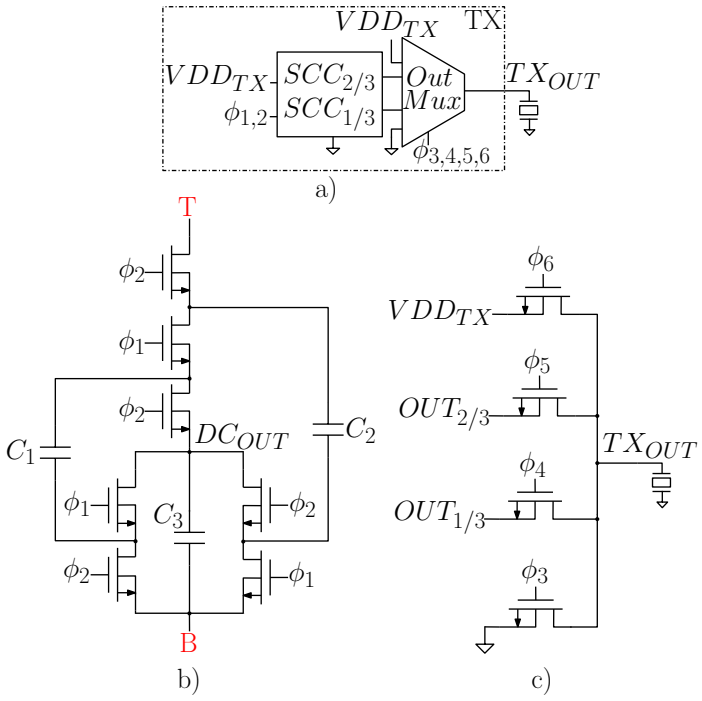

Figure 3.6: a) A detailed top-level implementation of the TX b) Schematic of the Dickson topology c) Output multiplexer.

an output multiplexer to generate a four-level driving signal and broadcast either a wake-up sequence or a digitally synthesized US chirp signal. A 4-level driving signal has been chosen considering the area and switching power of the switched capacitor converters (SCC) needed. The four-levels are generated connecting the transducer periodically to VDD_{TX}, the maximum voltage level applied to the load, two intermediate voltage levels ($2/3 \cdot VDD_{TX}$ and $1/3 \cdot VDD_{TX}$), and ground, as shown in Fig. 3.6a. The intermediate DC voltage levels are obtained from VDD_{TX} by using two Switched-Capacitor Converters ($SCC_{1/3,2/3}$). These converters use two 50% duty-cycled non-overlapping clocks, $\phi_{1,2}$. Each DC level is connected to the transducer for a time span and in an order that are controlled via the output multiplexer by the clocks $\phi_{3,..6}$.
An SCC can be modeled [91] as an ideal transformer (whose voltage ratio is defined by the SCC topology) in series with an output resistor, R_{out}. The DC level of the output of the TX is determined by the voltage division between R_{out} and the load impedance. Here, R_{out} represents the output resistance of the corresponding SCCs

with an additional series resistance due to the output multiplexer. To reduce the power consumption of the TX, 0.6V is chosen as VDD_{TX}. Each clock phase ϕ is buffered to the switching transistors in the SSCs and output multiplexer by on-chip drivers, which use a $VDD_{driver} = 1.2V$ supply. The transistor-level implementation of the TX is shown in Fig. 3.6b and Fig. 3.6c. All switches are implemented using insulated well nMOS transistors. A Dickson topology is chosen to implement the SCCs, since the same topology can be reused to obtain the intermediate voltage levels with a minor change in top-level connection. As shown in Fig. 3.6a, a voltage conversion ratio of 3:1 is obtained when VDD_{TX} and ground are connected to the top node, T, and the bottom node, B, respectively. The division ratio of 3:2 is obtained by interchanging the top node and the bottom node. The SCC output node is marked DC_{out} in Fig. 3.6b. $OUT_{1/3}$ and $OUT_{2/3}$ correspond to the output of $SCC_{1/3}$ and $SCC_{2/3}$, respectively. The capacitors $C_{1,2,3}$ are off-chip flying capacitors. The output multiplexer (Fig. 3.6c) comprises 4 nMOS transistors that connect the desired DC voltage to the transducer load. In $SCC_{2/3}$ and the output multiplexer, a parallel connection of four of these unit switches is used. This improves the driving efficiency of the TX as a lower SCC output resistance is assigned to a higher DC voltage level.

3.3 Wake-up Receiver Design

An important feature of the Wake-up Based FDD-FMCW rangefinder, as discussed in more detail in Chapter 2, is that the sensor nodes in the swarm use a wake-up link, which provides ultra low power consumption, while the FMCW method is exploited in a separate ranging link to find the relative distance among the nodes in the swarm. When the sensor nodes use the wake-up link (e.g. the sensor nodes are configured as tags), they use their wake-up receiver which is always-on. As a result, reducing the active power consumption of this receiver is important, while keeping a moderate sensitivity is needed to avoid excessive imbalance between the transmitter and receiver power consumption which would increase the energy per measurement. Previous literature exploits either an LNA-first architecture [45, 49, 50, 92] to achieve a very good sensitivity (e.g. around $-81dBm$ (see Appendix C)) or an envelope-detector (ED) first architecture [48] to aggressively reduce the active power consumption (e.g. down to 8nW [46]). The former approach leads to a large power consumption (e.g. up to a few μW [45]), while the latter approach sacrifices the achievable sensitivity (e.g. ≈ -60dBm [46]).
To derive the requirements needed for the wake-up receiver, a system-level design approach, as explained in Chapter 2, is followed by performing a link characterization in air among two identical transducers (e.g. T1). The outcome of this characterization is reported in Appendix A, where the received power at 1m distance in air while using two identical transducers T1 is measured as $-72dBm$. This requirement can be satisfied with an LNA-first topology, while an ED-based topology is not sufficient. As a result, an alternative method able to provide a moderate sensitivity, while satisfying

the ultra low-power constraint is needed for our application.
Considering that at the input of the receiver ≈12dB SNR is sufficient to have a 90% detection probability with a $<10^{-3}$ false alarm ratio [53], the integrated Input-Referred Noise (IRN) of the wake-up receiver should be lower than $14\mu V_{rms}$. To reduce the always-on power consumption of the nodes, a low-complexity communication scheme (e.g. On Off Keying) with a limited data-rate (e.g $\leq 0.5kbps$) can be exploited in the wake-up link [17]. This allows allocating a ≈1kHz baseband bandwidth (BW_{WURX}), thus an Input-Referred Noise Density (IRND) of $443\frac{nV}{\sqrt{Hz}}$ for the wake-up receiver is estimated.
Based on these requirements, a mixer-first topology has been chosen for the wake-up

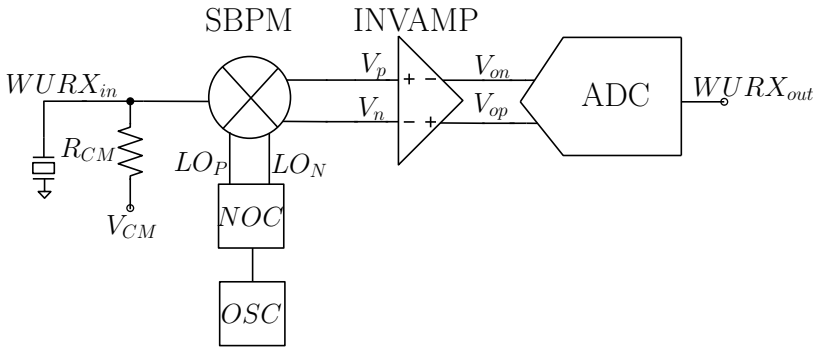

Figure 3.7: Top-level implementation of the wake-up receiver.

receiver, as shown in Fig. 3.7. A single-balanced passive mixer (SBPM) is used at the input of the wake-up receiver. Although the input-referred noise density of the front-end increases without an LNA preceding the mixer, the target integrated noise level (e.g. $\approx 14\mu V_{rms}$) can be achieved with this topology considering a BW limited to about 1kHz in the baseband amplifier. Such BW is sufficient, as the transducer T1 is used at its resonance frequency, and only the fundamental component is needed to transmit the wake-up message. The SBPM does not consume DC power, but enables single-ended to differential conversion, thus providing a theoretical gain of 1.48dB [93]. The mixer transforms the baseband impedance to an equivalent impedance seen at the transducer. The input impedance of the front-end remains high-impedance, enabling to sense the voltage produced without loading the transducer. Thanks to the use of a mixer-first front-end, the low-conversion gain of the ED is avoided and the sensitivity of the receiver can be improved. This allows reaching a moderate sensitivity (e.g. -69.5 dBm) while dissipating ultra low-power (e.g. around 23nW). After the SBPM, the wake-up receiver comprises an open-loop inverter-based baseband amplifier, INVAMP, and a 10-bit SAR ADC [55], as shown in Fig. 3.7. The down-conversion signal of the SBPM, LO, as well as the ADC clock, are provided by an on-chip oscillator, OSC. A single supply of 0.6V has been used in the front-end to save power. The transducer is DC coupled to the front-end, and the DC common-mode bias of the front-end, $V_{CM} = V_{DD}/2$, is provided through an off-chip resistance, R_{CM}, of 5MΩ.
Fig. 3.8 shows the full transistor-level implementation of the wake-up receiver until the ADC. The SBPM (Fig. 3.8a) comprises two nMOS transistors and sampling

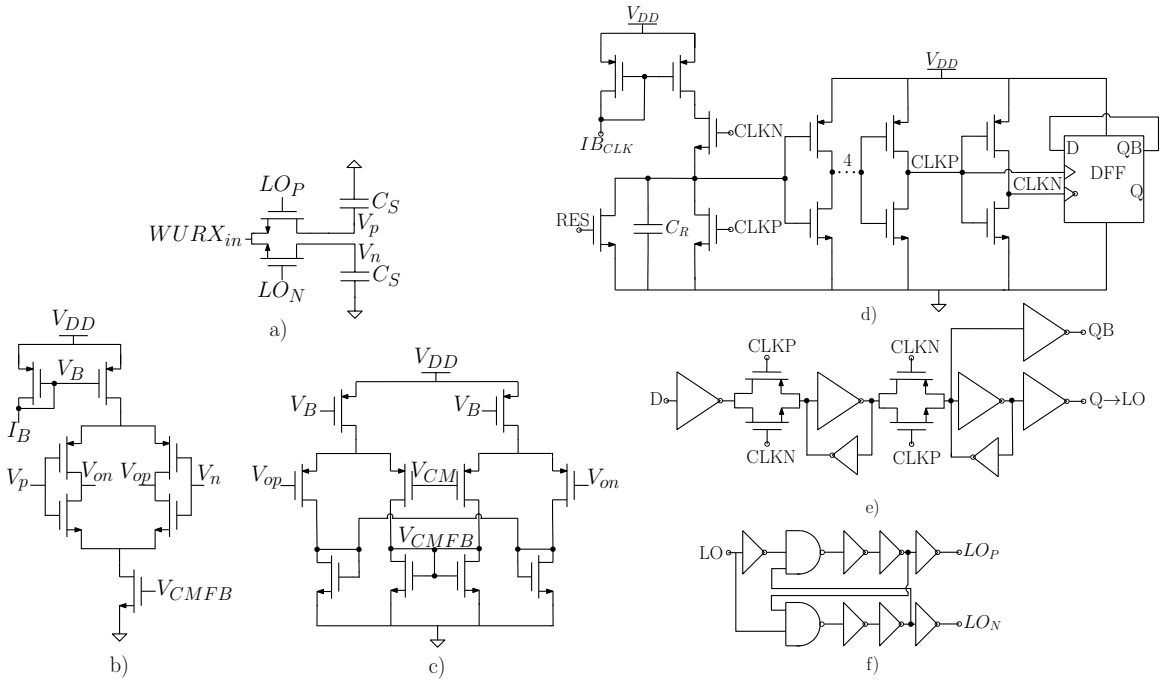

Figure 3.8: Building blocks of the wake-up receiver a) Single-balanced passive mixer, b) Inverter based baseband amplifier, c) Its CMFB. d) Schematic of the on-chip clock generator (OSC) e) Flip-flop f) Non-overlapping clock generator.

capacitors, C_S. The size of the transistors ($400nm/60nm$) is chosen to reduce the dynamic power. A C_S of $8.5pF$ is used to lower the noise contribution of the mixer. Considering the large capacitance of US transducers, the loading introduced by these capacitors is negligible. Fig. 3.8b and Fig. 3.8c show the implementation of the inverter-based baseband amplifier and its common-mode feedback (CMFB) [47], respectively. An inverter-based topology is chosen to increase the power efficiency while all transistors are biased in the weak-inversion region with a g_m/I_D ratio of 31 V^{-1}. The digital output of the wake-up receiver will be followed by a digital thresholding, to decide whether or not to wake-up the node, which is robust to variations of the LO over PVT. Thereby, the accuracy requirement of the LO frequency can be relaxed. This allows using a simple on-chip clock generator, as shown Fig. 3.8d. In the LO generator, an external reference current, IB_{CLK}, is integrated on the capacitor, C_R, to generate a ramp voltage. Then, a feedback loop comprising 6 stages of inverters resets the voltage on C_R when the threshold of the first inverter is reached. An external reset signal, RES, is used only at start-up. High-threshold transistors are used in the inverter chain to limit the power consumption, while 6 stages of inverters are used to provide enough on-time for the generated pulse signal. To obtain a 50% duty-cyle LO, the inverter chain is followed by a Master/Slave D-type flip-flop, which is implemented with two pass gate latches, as shown in Fig. 3.8e. The Q output of the DFF is used as an input to the non-overlapping clock generator circuit (Fig. 3.8f), which provides the signals, LO_P and LO_N, used by the SBPM for down-conversion.

As will be elaborated more in Chapter 4, the experimental characterization of the receiver shows that its measured integrated in-band noise is about $14\mu V_{rms}$, satisfying the design specs as discussed in this section, while dissipating only 23.6nW of power consumption, enabling a FOM_{WuRx} of 0.79 $(J/b) \cdot W \cdot 10^{-20}$, which is the best reported to date.

3.4 Conclusion

This chapter deals with circuit-level contributions proposed in this thesis for ultrasound communication and rangefinder systems for sensor swarms. In Section 3.1, the electrical model and its extracted parameters of ultrasound transducers used in this thesis are provided. Then, the circuit design steps of low-power low-noise ultrasound amplifiers suited to the piezoelectric transducers are given. Specifically, an inverter-based architecture is chosen thanks to to its current efficiency. To stabilize the output DC level of the single ended inverter-based amplifiers, a novel auxiliary-inverter based DC feedback loop is presented. The proposed DC feedback allows the single-ended inverter to work in continuous-time, minimizes degradation of the SNR at the input, and operates at a single supply voltage. The next section deals with the design of transmitters for US interfaces. First, Class-D buffers to drive ultrasound transducers at resonance with a high efficiency are presented. This is followed by introducing a novel four-level transmitter optimized for high energy-efficiency when driving the large parasitic capacitance of ultrasound transducers. Finally, the full implementation of the wake-up receiver at transistor level is presented. It has been concluded that an envelope detector first architecture is not sufficient in terms of sensitivity, while the LNA-first architecture is the best in terms of sensitivity but has the highest power consumption. Accordingly, the Mixer first architecture is chosen as it offers a solution with sufficient sensitivity and ultra lower-power consumption thanks to the immediate translation of the input signal to baseband before all active circuits.

Chapter 4

Main Experimental Results

This chapter presents the main experimental results of the US communication and US rangefinder systems presented in the preceding chapters. The system-level principles of these systems have been discussed in Chapter 2, and the critical hardware blocks needed to build the sensor nodes have been discussed in Chapter 3. This chapter is dedicated to describe the most important measurement setups build for the experimental characterization and to summarize the main experimental results obtained in this research. The readers are referred to the Appendices for a more detailed discussion on the experimental characterization of the proposed communication and rangefinder systems.

4.1 US Communication System Characterization

This section will deal with the experimental results of the US communication system, where a Class-D buffer with cascaded inverter stages (see Fig. 3.4a) and an inverter-based low-noise amplifier (see Fig. 3.2b) with a 10-bit SAR ADC were used as TX and RX, respectively (Fig. 4.2). A 65nm CMOS process is used for fabrication and the die photo (Chip 1) of the proposed ultrasound transceiver was shown in Fig. 1.2. The measured voltage gain, the 3dB bandwidth, and the integrated noise of the receiver are 30.7dB, 40kHz, and $2.2\mu V_{rms}$, respectively (see Appendix C).
The experimental characterization of the sensitivity level that can be reached with this front-end is first validated with electrical BER measurements. In these measurements, OOK modulated 40kHz input signals with different amplitudes at 1kbps data-rate are provided to the input of the RX via a bench-top arbitrary signal generator (AWG Keysight 33500B). External attenuators are applied to the AWG output to bring the signal amplitude to the desired level. Fig. 4.1 shows BER plots for this electrical input signal, where a $-83dBm$ input signal is demodulated with a 10^{-3} BER. Afterwards, a physical experimental test setup is built in air with the TX, RX, and two US transducers (T_1), as shown in Fig. 4.2 and Fig. 4.3. In this setup, OOK modulated random bits are generated in MATLAB and applied via an AWG to the

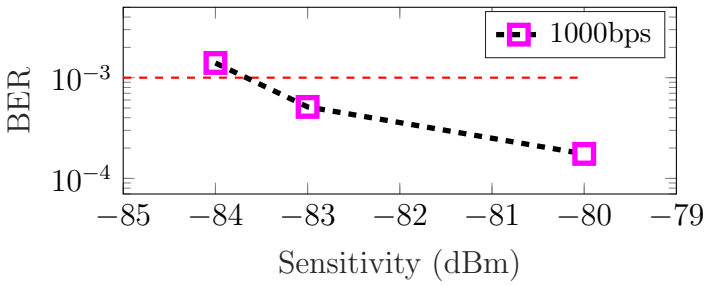

Figure 4.1: BER plots for an electrical input signal of variable amplitude provided to the receiver.

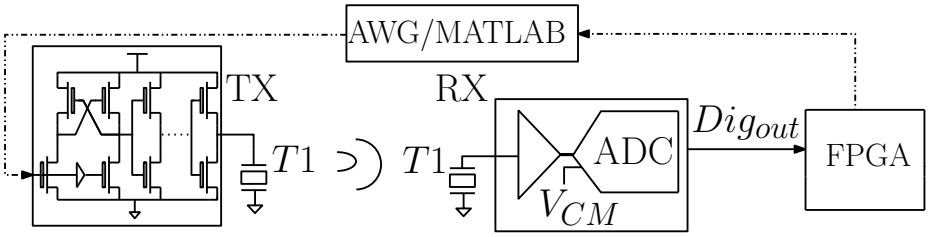

Figure 4.2: Experimental setup for the US communication system.

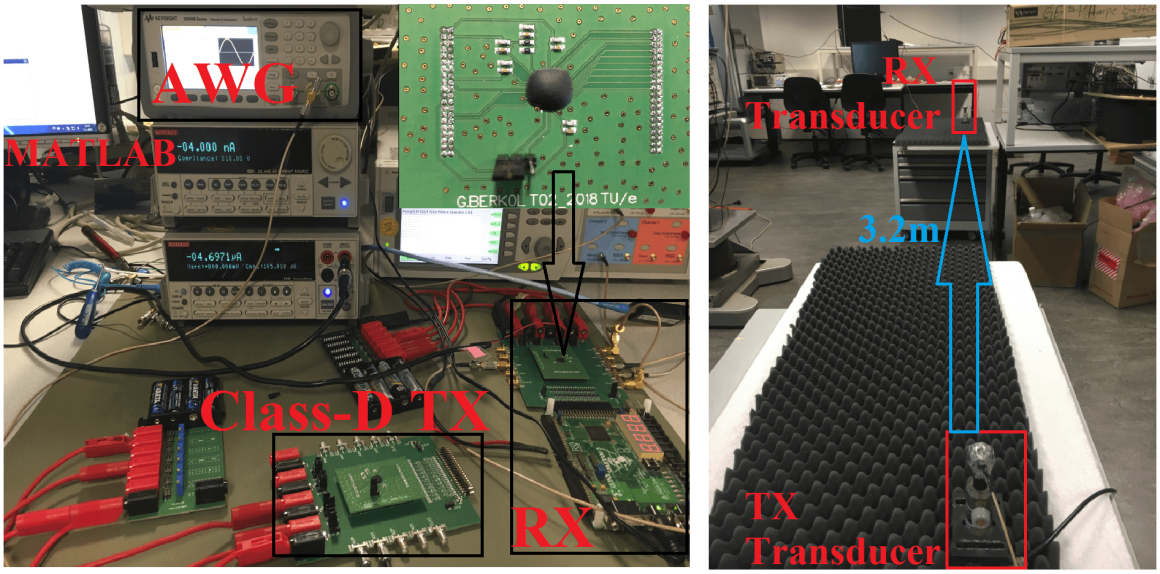

Figure 4.3: Measurement equipment and PCBs are shown on the left. The transmitting and receiving transducers at 3.2m distance are shown on the right.

transmitter chip, which drives the transmitting transducer. The resulting ultrasonic signal from the receiving transducer is read-out via the RX front-end and the ADC output, Dig_{out}, is recorded via an external FPGA and transferred to a computer (MATLAB). There, a simple demodulation algorithm based on a band-pass filtering

and a thresholding is implemented to detect the incoming bits. Due to the additional noise and echoes coming from the setup environment, a 10^{-3} BER with a sensitivity of -81.6dBm is achieved at a communication distance of 3.2m in air, as shown in Fig. 4.3.
Fig. 4.4 shows the measured output of the RX corresponding to the simple communication link implemented in this work. The communication starts by broadcasting a sequence of two consecutive high levels as a header (HDR). The rest of the transmitted data is Manchester encoded, where the transition from high-level to low-level is regarded as '0', and the transition from low-level to high-level is regarded as '1'. The demodulation of these encoded data is implemented in MATLAB.
The total receiver power consumption of the LNA and ADC is measured as $1.18\mu W$.

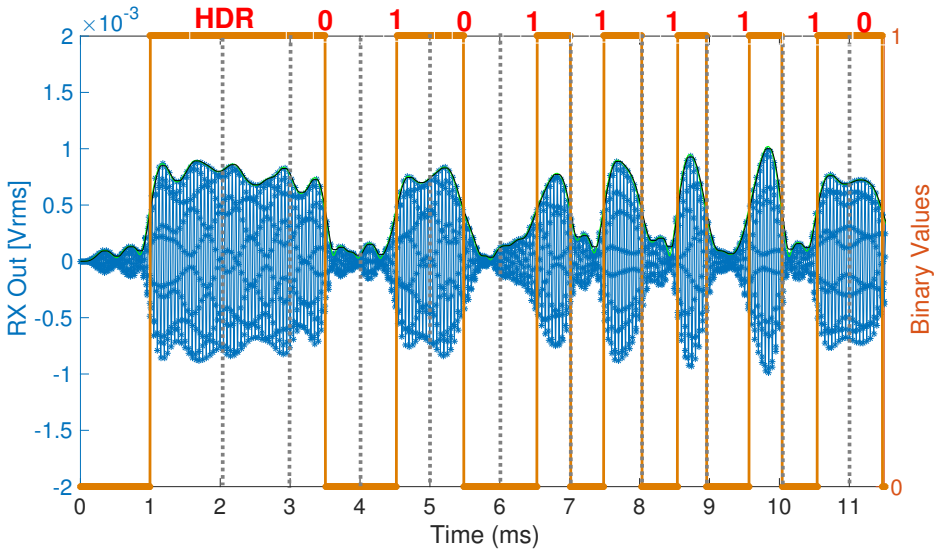

Figure 4.4: Measured sequence of OOK communication with Manchester encoded data. The data rate is 1kbps.

The measured power consumption of the transmitter at a 1kbps data-rate is $50\mu W$. As a result, the overall energy consumption of the TX+RX link is measured to be 51.18 nJ/bit. The proposed receiver achieves a measured sensitivity of -81.6dBm, which corresponds to a communication distance of 3.2m in air with the transducers used (see Fig. 4.3). The proposed transceiver achieves the lowest energy per bit performance of 51.18nJ/b and the best sensitivity reported among US transceivers at the time of writing this manuscript. In this communication system, the transmitter can be duty cycled (DC_{TX}) by a factor 2.5%, e.g. assuming that the transmitting node sends once per second a 25b message. In this case, the duty-cycling of the TX brings its average power consumption down to $\approx 1.2\mu$W, balancing the power consumption of the RX and TX functions.

4.2 US Rangefinder Systems Characterization

This section will present the experimental results of the FDD-FMCW based US rangefinder systems. The conceptual experimental setup to demonstrate the proof-of-

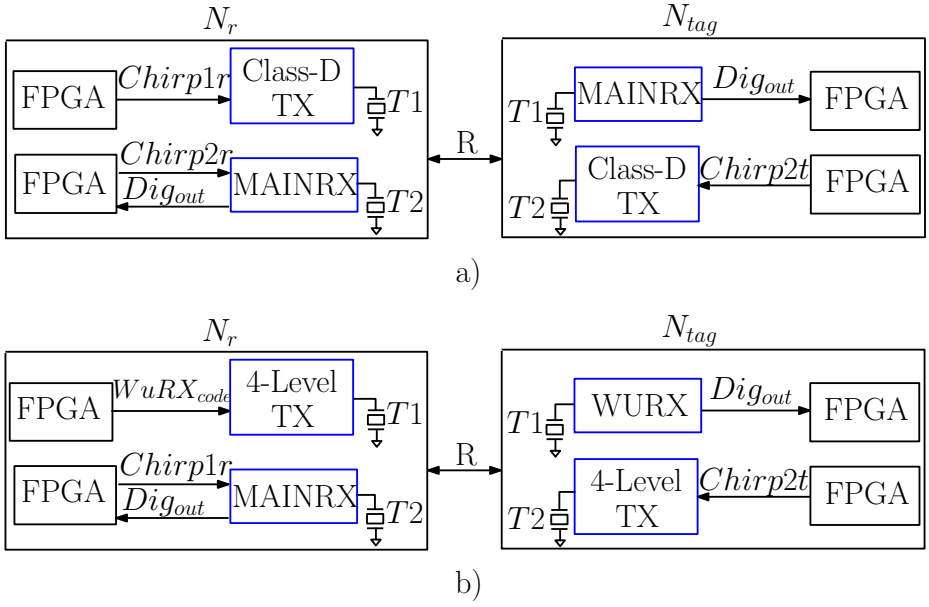

Figure 4.5: Conceptual illustration of the experimental setup for the US rangefinder systems. a) The hardware of the nodes in the rangefinder system with a chirp exchange b) The hardware of the nodes in the wake-up based rangefinder system.

concept principle of the proposed systems is depicted in Fig. 4.5, where the ranging between a ranger node N_r and an active-tag N_{tag} at a distance R is illustrated. Fig. 4.5a and Fig. 4.5b depict the specific implementation of the nodes hardware for the rangefinder system with a chirp exchange and the wake-up based rangefinder system, respectively. A Xilinx Spartan-3 FPGA Board has been used for each transmitter or receiver of the nodes to implement the digital functions. The Chirp needed in the ranging receiver and the control clocks of the transmitters are digitally synthesized by reading at a constant rate (1MHz) suitable bit streams preloaded to the FPGA. The time reference for each node is provided *separately* by an external 50MHz crystal oscillator, which is available on the FPGA boards (Fig. 4.6). The digital signal processing, such as the FFT needed to determine the beat frequency in the FMCW ranging, are performed outside the nodes. The output data generated from the ranging receiver of N_r by mixing the Chirp signals during the ranging are thus saved to a memory in the FPGA and transferred to MATLAB, where the post-processing to find the frequency peaks is performed. The proof-of-concept characterization is performed by using only one ranger node and a tag to simplify the complexity of the measurement setup. A 65nm CMOS process is used for fabrication of the node circuits and the die photos of the circuits (Chip 2 for the receivers and Chip 3 for the transmitters) were shown

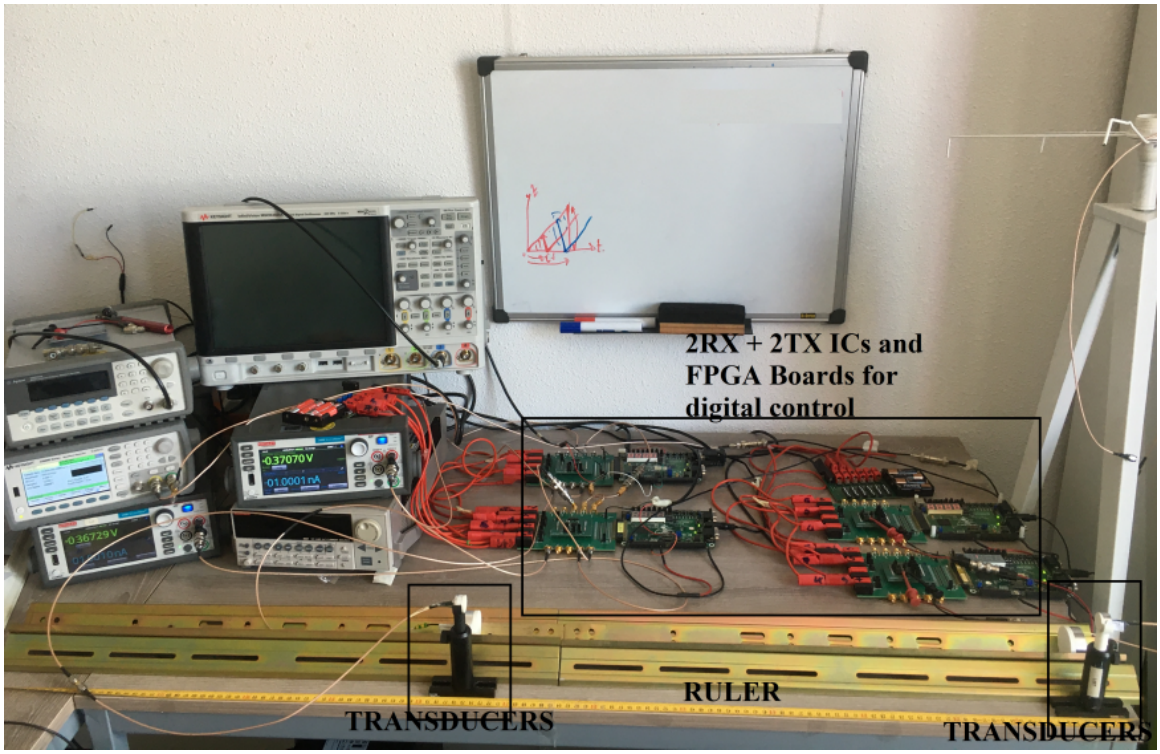

Figure 4.6: Experimental setup built in air *at the authors home* to characterize the proposed rangefinder systems during Covid-19 pandemic.

in Fig. 1.2. Fig. 4.6 shows the corresponding physical experimental setup with the custom-made hardware, which is built in air at room temperature without external synchronization among the nodes N_r and N_{tag}. A detailed characterization of the individual circuits and the proposed ranging systems are presented in Appendices A and B.

4.2.1 FDD-FMCW based Rangefinder System with a Chirp Exchange: Main Experimental Results

In this experiment, the MAINRX (see Chip 2 in Fig. 1.2) is used as receiver and the two-level multiplexer based Class-D transmitter (see Fig. 3.4b and Chip 3 in Fig. 1.2) is used as transmitter in both nodes, as illustrated in Fig. 4.5a. The measured conversion gain, the 3-dB BW, and the integrated noise of the MAINRX for an LO=100kHz are 42.4dB @1kHz offset, 21.4kHz, and 8.8μV_{rms}, respectively. The MAINRX draws a total measured current of 930nA from a 0.6V supply, therefore, dissipates a total power of 0.56μW. The TX dissipates 1.59μJ per Chirp2t when driving T2, and dissipates 1.07μJ per Chirp1r when it drives T1. The proposed rangefinder system thus requires 2.67μJ energy per distance measurement, which is in line with the relevant state-of-the-art (see Appendix B).

A proof-of-concept characterization of the proposed FDD-FMCW based rangefinder

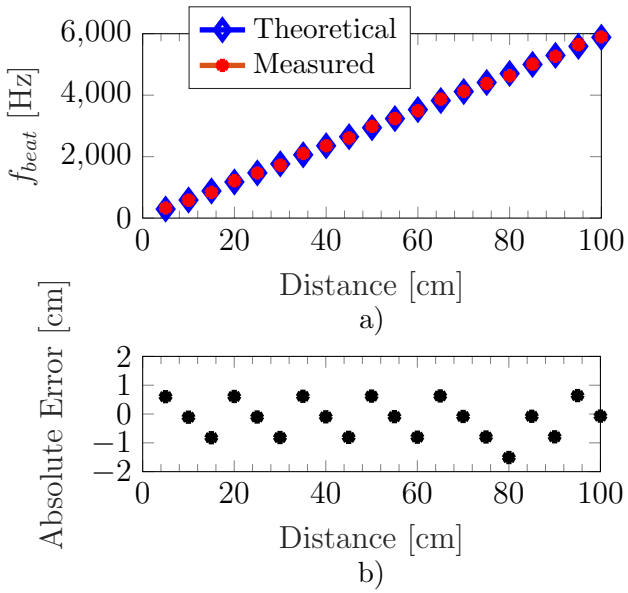

Figure 4.7: a) FMCW ranging link characterization b) Absolute error in the distance measurement.

system with a chirp exchange up to 1m in air is summarized in Fig. 4.7a, and the calculated absolute distance error is depicted in Fig. 4.7b. The main factor limiting measurement accuracy of this experiment is the quantization error due to the Fast Fourier Transform (FFT) applied to the receiver output. As discussed in more detail in Chapter 2, at a specific distance, the ranger node initiates the ranging protocol, and mixes in its receiver the chirp sent by the active tag (Chirp2t) with a chirp that is generated locally in the initiator node (Chirp2r). The ADC output data (Dig_{out}) of the ranger node are recorded during one sweep time, T_{sweep}, of 8ms (Appendix B). Afterwards, the FFT of the recorded data is calculated in MATLAB, where the frequency resolution of the derived spectrum is given by the inverse of the signal duration, which is equal to $\Delta f = 125$Hz. Using the equation to determine the distance between nodes ($\frac{\Delta f \cdot c_{US} \cdot T_{sweep}}{2BW}$), this corresponds to a minimum measurable distance $R_{min} = 21$mm in the experiment. Since a smaller distance cannot be resolved by this experiment, a quantization error of amplitude R_{min} is made when calculating the distance R. A common assumption for the analysis of quantization errors is that they are uniformly distributed [94]. This error will thus have ideally an average value of 0 and a standard deviation of $\frac{R_{min}}{\sqrt{12}}$. In our experiment R_{min}=21mm, thus one would expect for the experimental error a 0 mean and a standard deviation of $\approx 6.1mm$. The characterization results summarized in Fig. 4.7b give a 2mm mean with a 6.5mm standard deviation. The measurement outcome is in good agreement with the theoretical expectation, thus the FFT quantization is indeed the main limiting factor to the ranging resolution in this experiment. Besides, the saw-tooth shape of the error distribution (Fig. 4.7b) is what one would expect in a system dominated by quantization errors. If a lower FFT quantization error is desired, a longer sweep

time can be used at the cost of an increased energy consumption during the ranging.

4.2.2 Wake-up based Rangefinder System: Main Experimental Results

In this experiment, the WURX (see Chip 2 in Fig. 1.2) has been used as receiver on the tag, the four-level TX (see Chip 3 in Fig. 1.2) has been used for both transmitters, and the MAINRX (see Chip 2 in Fig. 1.2) has been used as receiver in the ranger node, as shown in Fig. 4.5b. For the wake-up receiver, using an LO=39kHz, the measured conversion gain, the 3-dB BW, and the integrated noise are 32.8dB @200Hz offset, 1.2kHz, and $14\mu V_{rms}$, respectively (see Appendix A). With a total of 23.6nW power consumption, the wake-up receiver achieves a FOM_{WuRx} of $0.79{\cdot}10^{-20}(J/b){\cdot}W$, which is the best among prior-art US wake-up receivers. The four-level TX (see Fig. 3.6) dissipates $0.82\mu J$ per Chirp2t when driving T2, and dissipates $0.43\mu J$ per broadcasting a wake-up sequence when it drives T1. The proposed wake-up based rangefinder system thus dissipates $1.25\mu J$ per measurement, which is the lowest reported to date among prior-art US rangefinder systems. A proof-of-concept characterization of the

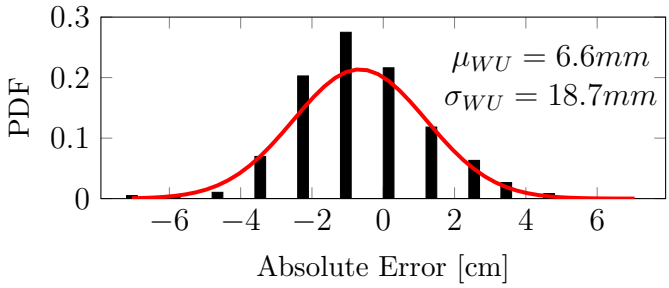

Figure 4.8: A normalized histogram of the 10000 measurements at 0.55m.

full proposed system, including the wake-up and ranging links, is demonstrated with the setup shown in Fig. 4.6. The ADC data of the ranging receiver is recorded during a sweep time, T_{sweep}, of 10ms (Appendix A). The ranging experiment is performed in air at room temperature without external synchronization. The LO from the on-chip clock generator is used in the wake-up receiver. To quantify the overall ranging error, N_r and N_{tag} are placed at 0.55m apart and the distance measurement of the full rangefinder system is repeated 10000 times. Fig. 4.8 shows the histogram of the absolute error, which is fitted to a normal distribution with a mean (μ_{WU}) of 6.6mm and a standard deviation (σ_{WU}) of 18.7mm. In this experiment, the jitter of the LO in the wake-up link and the ADC sampling in the wake-up receiver result in an uncertainty of the wake-up time of the node, which is reflected as an error in the distance measurement and dominates the observed standard deviation.
In Fig. 4.9a, the rangefinder system measurements of the f_{beat} up to 1m are shown, where at each point an average of N=15 measurements is reported. The averaging results in a decrease of the standard deviation due to random sources of uncertainty

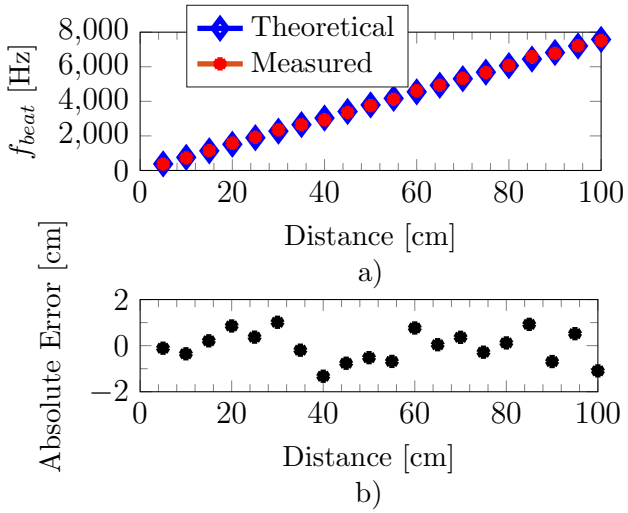

Figure 4.9: a) Full-system ranging link characterization. b) Absolute error of the rangefinder system. Each point is an average of 15 independent measurements.

in the wake-up receiver. The deterministic error caused by the FFT resolution for the two-way ranging can be estimated using the equation to determine the distance between nodes ($\frac{\Delta f \cdot c_{US} \cdot T_{sweep}}{2BW}$), which corresponds a minimum measurable distance $R_{min} = 13mm$. Changing the measurement distance will thus cause a uniformly distributed ranging error with a standard deviation $\sigma_{FFT2} = \frac{R_{min}}{\sqrt{(12)}} = 3.7mm$. Combining the two uncorrelated error sources (LO jitter in the wake-up receiver and FFT quantization), one would predict for the full system measurements a standard deviation σ_{tot}, which can be estimated as $\sigma_{tot} = \sqrt{\frac{\sigma_{WU}^2}{N} + \sigma_{FFT2}^2} = 6.1$mm. The measured error in Fig. 4.9b has a mean of 0.5mm and a standard deviation of 7mm, which is close to the expected value. It can be observed that the addition of the wake-up uncertainty randomizes the shape of the error in Fig. 4.9b compared to the sawtooth behavior observed in Fig. 4.7b. Using a separate wake-up link worsens the ranging resolution (18.7mm) compared to the ranging resolution (6.5mm) of the rangefinder system with a chirp exchange, which is tolerable in our applications. The advantages of the proposed wake-up based FDD-FMCW rangefinder system are the reduced always-on power consumption of the nodes (which is only 23.6nW) and the improved energy per measurement ($1.25\mu J$), which is at least 2x better compared to prior art US rangefinders.

4.3 Conclusion

This chapter first presents the experimental setup and experimental characterization of the US communication system. OOK modulated data have been used to achieve low-bit rate low-energy data exchange among the nodes. Measurement results show that the proposed circuits achieve this goal at 1kbps data-rate with a state-of-the-art

sensitivity (-81.6dBm) and energy per bit (51.18nJ/b) for a US transceiver. The following sections present the experimental setup and characterization of two rangefinder systems proposed in this thesis. The rangefinder system with a chirp exchange dissipates $2.67\mu J$ energy per distance measurement, while achieving a ranging resolution of 6.5mm. It has been concluded that the range resolution is limited by the FFT quantization. The wake-up based rangefinder system uses a separate wake-up link, enabling to minimize the always-on power consumption of the nodes. In addition, this rangefinder system exploits an energy-efficient four-level transmitter, reducing the energy per distance measurement to $1.25\mu J$. In this case, the uncertainty of the wake-up time of the tags increases the ranging resolution of the distance measurement to 18.7mm.

Chapter 5

Conclusions and Future work

5.1 Conclusions

The Phoenix project aims at developing novel techniques to explore liquid-filled enclosed environments. Example applications include the exploration of the ocean floor, underground infrastructures, water distribution systems, and industrial tanks for processing chemicals. Due to the fact that human access (either direct or remote) to these environments is significantly limited, sensor swarms will be used to collect data from the operating environment. This is a novel approach for such challenging exploration tasks.
The Phoenix project exploits the go-with-the-flow approach to enable gathering data among the resource-limited sensor nodes to extract information about the geometry of the volumes explored by the swarm. This approach is based on inserting the swarm of sensor nodes into the volume to explore and recuperating them at the end of the exploration. Inside the volume, sensor nodes cannot communicate to the outside world and must be autonomous. While they traverse with the flow of the medium, the nodes perform distance measurements among each other. These mutual distance measurements are recorded in their memory and used at the post-processing to build a map of the volume being explored.
There are, however, significant constraints imposed on the nodes. First of all, their size has to be sufficiently small to enable injection inside these volumes. As a result, the available energy is limited due to the small physical size requirement to a node in the swarm. Furthermore, the nodes cannot use electromagnetic signals, due to their severe attenuation in conductive mediums, preventing to use conventional position tracking systems like GPS. Furthermore, the propagation in the enclosed volumes is susceptible to multipath propagation and collisions (interferences) among different sensor nodes in the swarm, increasing the complexity of extracting distance information from the measurements and decreasing the reliability when reconstructing the geometry of the explored volumes.
Except for the common requirements to have a system suited to the go-with-the-flow approach, such as having identical, miniaturized, and resource-limited sensor nodes

that will build a swarm, there are no other specifications defined for the applications considered in this thesis. As a result, this work investigates first suitable design approaches at the system-level, e.g. the type of propagation signal, modulation schemes, frequency of operation, distance measurement protocol, distance measurement technique, etc., circuit-level implementations are then considered studying transistor-level hardware implementation to develop low-power communication and rangefinder systems for sensor swarms.

To build such a challenging system, the research questions this thesis aims to answer are summarized as:

1. Can we establish an energy-efficient ultrasound communication link among the resource-limited sensor nodes?
2. Can we devise an ultrasound rangefinder system for a swarm of sensor nodes that can successfully operate in collision and multipath rich enclosed volumes?
3. Can we design critical building blocks of these systems at a transistor-level and experimentally demonstrate the proof-of-concept principle of the proposed systems?

This thesis, in general terms, answers positively to these questions, as described here below in more detail:

1. In Chapter 2, the design steps towards building energy-efficiency ultrasound links are provided. It has been shown that ultrasound signals propagate with a lower attenuation compared to RF signals, and thus can be used for data-exchange among the nodes. To reduce the complexity of the baseband demodulation circuits and transmitter architecture, a low-complexity OOK modulation scheme has been chosen. Furthermore, a novel design approach suited to symmetrical ultrasound links is presented, which is based on exploiting a holistic optimization to consider both ultrasound transmission and reception. The experimental outcome of this design is given in Chapter 4, which shows a -81.6dBm sensitivity and energy per bit of 51.18nJ/b for an ultrasound transceiver, establishing an energy-efficient link among resource-limited nodes at 3.2m distance in air. These results are published in a scientific paper (see Appendix C), and are the best reported figures among prior-art ultrasound transceivers at the time of writing this manuscript.
2. In Chapter 2, the requirements of ultrasound rangefinder systems suited for the go-with-the-flow approach are presented. The nodes in a swarm need to perform measurements to find their relative distance without a global synchronization when they are operated in multipath and collision rich enclosed environments. For this purpose, a distance measurement method based on Time of Flight has

been chosen. However, the conventional rangefinder systems are shown to be unsuited to our applications, as they are sensitive to interferences caused by echoes from the boundaries of the volume to explore. To address this challenge, two novel Frequency Division Duplexing (FDD) Frequency Modulated Continuous Wave (FMCW)-based rangefinder systems are proposed. The first rangefinder system, named FDD-FMCW rangefinder system with a chirp exchange, is based on broadcasting and receiving frequency modulated ultrasound signals, which are useful in collision and multipath rich environments. The second system, named wake-up based FDD-FMCW rangefinder system, exploits a wake-up link in addition to the ranging link to minimize the always-on node power consumption. These rangefinders are based on using separate frequency bands for the ultrasound transmission and reception, making the distance measurement insensitive to the echoes generated by the boundary of the environment being explored while allowing to distinguish the multipath propagation of the active responses. To the best of the authors' knowledge, these systems are first in literature to provide experimentally validated ultrasound distance measurement methods that simultaneously address the multipath and collision phenomena while avoiding synchronization requirements of the sensor nodes in a swarm.

3. In Chapter 3, the circuit design of critical building blocks of sensor nodes is presented. These blocks include an ultrasound low-noise amplifier, an ultrasound transmitter, and a wake-up receiver to complete the rangefinder systems proposed in this thesis. Regarding the low-noise amplifier, a single-ended inverter-based architecture is chosen due to its power efficiency. The design challenge of single-ended amplifiers is stabilizing their output DC point. For this reason, this thesis proposes a novel auxiliary inverter-based DC feedback loop to stabilize the output DC point of an inverter-based amplifiers.
   On the transmitter side, this thesis first investigates simple class-D buffers to drive ultrasound transducers. The main challenge of these drivers is their large energy consumption due to the large parasitic capacitance of the transducers. To alleviate this bottleneck, this thesis proposes a novel four-level ultrasound transmitter to drive ultrasound transducers.
   In Chapter 3, previous literature based on ultrasound wake-up receivers is also provided. It has been shown that a new solution is needed for the applications considered in this thesis with an emphasis on ultra low-power consumption and moderate sensitivity. For this purpose, this thesis proposes a mixer-first based topology for ultrasound wake-up receivers. The above mentioned critical circuits are all designed at a transistor-level, taped-out, and measured.
   Chapter 4 describes the main experimental results obtained when combining the custom made integrated circuits, where the physical characterization setup and the proof-of-concept principle of the proposed ultrasound rangefinder systems are shown. The FDD-FMCW rangefinder system with a chirp exchange dissipates a $2.67\mu J$ energy per distance measurement while achieving a ranging resolution of 6.5mm up to 1m distance in air. The wake-up based FDD-FMCW

rangefinder system exploits a separate wake-up link to reduce the always-on power consumption of the nodes down to 23.6nW. The measurement results show that the wake-up based FDD-FMCW rangefinder system achieves an energy consumption of $1.25\mu J$ per measurement with a 18.7mm range resolution up to 1m distance in air. The energy per measurement figure is the lowest reported to date. These results are presented in scientific journal papers (see Appendices A and B).

5.2 Future work

The developed work could be further extended or exploited in the future as follows:

- This work uses commercial piezoelectric ultrasound transducers for a proof-of-concept demonstration. Full miniaturization of the nodes for more challenging future applications e.g. exploration of underground reservoirs or water droplets in space missions is needed. For this purpose, the proposed systems and circuits can be used together with MEM transducers, enabling to shrink impressively the form factor of the nodes.

- The experimental characterizations of the proof-of-concept principle of the proposed ultrasound communication and rangefinder systems have been performed in air. The experimental setup used for characterization of the rangefinder systems was shown in Fig. 4.6. The attenuation of ultrasound in air is much larger than in water, allowing to test the communication and rangefinder systems at a manageable distance between the nodes. Future work focusing on experimentally demonstrating the proposed systems when the nodes are operated in fluidic mediums, e.g. in a water pool, would significantly increase the impact of this work.

- The focus in this thesis is to demonstrate that a node in the system can find its relative distance to the other nodes (e.g. tags) in a swarm. Thus, the scope is limited to finding the relative distances rather than decoding the identification payload of the tags. This payload has not been implemented in the current work. The proposed systems can be extended by developing a joint communication system while performing the FMCW ranging.

- The experimental characterizations of the proposed systems do not include multi-tag detection. This work includes experimental characterizations for only the case where a ranger node finds its relative distance to one other tag. However, the proposed approach allows performing distance measurements when there are multi-tags present and respond back to the ranger node. Future work that builds a setup to characterize this property would significantly add to the contributions of this thesis.

- The transducers used in this work require a line-of-sight deployment, whereas the proposed systems can be used with omni-directional transducers as well. For this purpose, commercial underwater transducers (DualSense 115 from Chelsea Technologies) are acquired, however, they have not been tested with the chips designed in this thesis yet. It would be meaningful to build test setup suitable to mimic enclosed fluidic environments using the above-mentioned underwater transducers.

- The peripheral circuit blocks needed to complete the rangefinder system, such as power management, voltage regulation, and bias generation can be integrated together with the proposed interface circuits. This will allow further miniaturization of the nodes.

- The peripheral digital circuits such as digital comparators and the digital backend needed in the proposed systems are implemented in a Xilinx FPGA Development Board. However, top-level reconstruction algorithms needed to obtain the final outcome, e.g. geometry of the enclosed volumes traveled by the swarm, have not been tested with the proposed systems. Future work focusing on demonstrating a full cycle of the Phoenix concept with a suitable miniature digital backend would significantly add to the contributions of this work.

References

[1] C. Darwin, *The Origin of Species; And, the Descent of Man.* Modern library, 1859.

[2] G. Berkol, E. Afacan, G. Dündar, A. E. Pusane, and F. Başkaya, "A novel yield aware multi-objective analog circuit optimization tool," in *2015 IEEE International Symposium on Circuits and Systems (ISCAS).* IEEE, 2015, pp. 2652–2655.

[3] E. Afacan, G. Berkol, G. Dundar, A. E. Pusane, and F. Baskaya, "An analog circuit synthesis tool based on efficient and reliable yield estimation," *Microelectronics Journal*, vol. 54, pp. 14–22, 2016.

[4] E. Vassev, R. Sterritt, C. Rouff, and M. Hinchey, "Swarm technology at NASA: building resilient systems," *IT Professional*, vol. 14, no. 2, pp. 36–42, 2012.

[5] G. Berkol, A. Unutulmaz, E. Afacan, G. Dündar, F. V. Fernandez, A. E. Pusane, and F. Başkaya, "A two-step layout-in-the-loop design automation tool," in *2015 IEEE 13th International New Circuits and Systems Conference (NEWCAS).* IEEE, 2015, pp. 1–4.

[6] C. A. Rouff, "Intelligence in future NASA swarm-based missions." in *AAAI Fall Symposium: Regarding the Intelligence in Distributed Intelligent Systems*, 2007, pp. 112–115.

[7] M. G. Hinchey, J. L. Rash, W. F. Truszkowski, C. A. Rouff, and R. Sterritt, "Autonomous and autonomic swarms," 2005.

[8] (2020) Phoenix project. [Online]. Available: https://www.phoenix-project.eu/

[9] M. Andraud, G. Berkol, J. De Roose, S. Gannavarapu, H. Xin, E. Cantatore, P. J. A. Harpe, M. Verhelst, and P. G. M. Baltus, "Exploring the unknown through successive generations of low power and low resource versatile agents," in *Design, Automation & Test in Europe Conference & Exhibition (DATE), 2017.* IEEE, 2017, pp. 290–293.

[10] E. H. Duisterwinkel, G. Dubbelman, E. Talnishnikh, J. J. Bergmans, H. J. Wörtche, and J.-P. M. Linnartz, "Go-with-the-flow swarm sensing in inaccessible viscous media," *IEEE Sensors Journal*, 2019.

[11] E. Talnishnikh, J. van Pol, and H. Wörtche, "Micro motes: A highly penetrating probe for inaccessible environments," in *Intelligent Environmental Sensing*. Springer, 2015, pp. 33–49.

[12] J. Jang and F. Adib, "Underwater backscatter networking," in *Proceedings of the ACM Special Interest Group on Data Communication*, 2019, pp. 187–199.

[13] H. A. Duisterwinkel, "Exploring enclosed environments with floating sensors: mapping using ultrasound," Ph.D. dissertation, Technische Universiteit Eindhoven, 2019.

[14] S. Schlupkothen, A. Hallawa, and G. Ascheid, "Evolutionary algorithm optimized centralized offline localization and mapping," in *2018 International Conference on Computing, Networking and Communications (ICNC)*. IEEE, 2018, pp. 625–631.

[15] S. Schlupkothen and G. Ascheid, "Localization of ambiguously identifiable wireless agents: complexity analysis and efficient algorithms," *EURASIP Journal on Advances in Signal Processing*, vol. 2018, no. 1, p. 30, 2018.

[16] J. Lloret, S. Sendra, M. Ardid, and J. J. Rodrigues, "Underwater wireless sensor communications in the 2.4 GHz ISM frequency band," *Sensors*, vol. 12, no. 4, pp. 4237–4264, 2012.

[17] S. Sendra, J. Lloret, J. M. Jimenez, and L. Parra, "Underwater acoustic modems," *IEEE Sensors Journal*, vol. 16, no. 11, pp. 4063–4071, 2015.

[18] M. J. Weber, Y. Yoshihara, A. Sawaby, J. Charthad, T. C. Chang, and A. Arbabian, "A miniaturized single-transducer implantable pressure sensor with time-multiplexed ultrasonic data and power links," *IEEE Journal of Solid-State Circuits*, vol. 53, no. 4, pp. 1089–1101, 2018.

[19] H.-Y. Tang, D. Seo, U. Singhal, X. Li, M. M. Maharbiz, E. Alon, and B. E. Boser, "Miniaturizing ultrasonic system for portable health care and fitness," *IEEE transactions on biomedical circuits and systems*, vol. 9, no. 6, pp. 767–776, 2015.

[20] MCUSR18A40B12RS-MCUSD40A100B17RS70C-MCUSD19A200B11RS. (2020) Multicomp ultrasonic sensors. [Online]. Available: https://uk.farnell.com/multicomp-ultrasonic-transducers

[21] G. Kokossalakis, "Acoustic data communication system for in-pipe wireless sensor networks," Ph.D. dissertation, Massachusetts Institute of Technology, 2006.

[22] M. Stojanovic and J. Preisig, "Underwater acoustic communication channels: Propagation models and statistical characterization," *IEEE communications magazine*, vol. 47, no. 1, pp. 84–89, 2009.

[23] H.-P. Tan, R. Diamant, W. K. Seah, and M. Waldmeyer, "A survey of techniques and challenges in underwater localization," *Ocean Engineering*, vol. 38, no. 14-15, pp. 1663–1676, 2011.

[24] M. Erol-Kantarci, H. T. Mouftah, and S. Oktug, "Localization techniques for underwater acoustic sensor networks," *IEEE Communications Magazine*, vol. 48, no. 12, pp. 152–158, 2010.

[25] R. M. Eustice, H. Singh, and L. L. Whitcomb, "Synchronous-clock, one-way-travel-time acoustic navigation for underwater vehicles," *Journal of Field Robotics*, vol. 28, no. 1, pp. 121–136, 2011.

[26] J. Liu, Z. Wang, J.-H. Cui, S. Zhou, and B. Yang, "A joint time synchronization and localization design for mobile underwater sensor networks," *IEEE Transactions on Mobile Computing*, vol. 15, no. 3, pp. 530–543, 2015.

[27] E. H. Duisterwinkel, N. A. Puts, and H. J. Wörtche, "Asymmetric multi-way ranging for resource-limited nodes," in *Ad Hoc Networks*. Springer, 2017, pp. 50–63.

[28] G. Berkol, P. G. M. Baltus, and E. Cantatore, "An ultrasound rangefinder system and distance measurement technique based on a harmonic FMCW method," *Submitted to Dutch Patent Office*, 2020.

[29] G. Berkol, P. G. M. Baltus, P. J. A. Harpe, and E. Cantatore, "Design of a low-power ultrasound transceiver for underwater sensor networks," in *2018 14th Conference on Ph. D. Research in Microelectronics and Electronics (PRIME)*. IEEE, 2018, pp. 129–132.

[30] ——, "A 2.67 μJ per measurement FMCW ultrasound rangefinder system for the exploration of enclosed environments," *IEEE Solid-State Circuits Letters*, vol. 3, pp. 326–329, 2020.

[31] P. G. M. Baltus, "Minimum power design of RF front ends." Ph.D. dissertation, Technische Universiteit Eindhoven, 2002.

[32] A. I. Al-Shamma'a, A. Shaw, and S. Saman, "Propagation of electromagnetic waves at MHz frequencies through seawater," *IEEE Transactions on antennas and propagation*, vol. 52, no. 11, pp. 2843–2849, 2004.

[33] X. Che, I. Wells, G. Dickers, P. Kear, and X. Gong, "Re-evaluation of RF electromagnetic communication in underwater sensor networks," *IEEE Communications Magazine*, vol. 48, no. 12, pp. 143–151, 2010.

[34] B. Benson, Y. Li, R. Kastner, B. Faunce, K. Domond, D. Kimball, and C. Schurgers, *Design of a low-cost, underwater acoustic modem for short-range sensor networks*. IEEE, 2010.

[35] D. Anguita, D. Brizzolara, and G. Parodi, "Optical wireless communication for underwater wireless sensor networks: Hardware modules and circuits design and implementation," in *OCEANS 2010 MTS/IEEE SEATTLE*. IEEE, 2010, pp. 1–8.

[36] I. F. Akyildiz, D. Pompili, and T. Melodia, "Underwater acoustic sensor networks: research challenges," *Ad hoc networks*, vol. 3, no. 3, pp. 257–279, 2005.

[37] M. Stojanovic, "On the relationship between capacity and distance in an underwater acoustic communication channel," *ACM SIGMOBILE Mobile Computing and Communications Review*, vol. 11, no. 4, pp. 34–43, 2007.

[38] Z. Yu, "Low-power receive-electronics for a miniature 3D ultrasound probe," Ph.D. dissertation, Technische Universiteit Delft, 2012.

[39] C. E. Shannon, "Communication in the presence of noise," *Proceedings of the IRE*, vol. 37, no. 1, pp. 10–21, 1949.

[40] G. Gurun, C. Tekes, J. Zahorian, T. Xu, S. Satir, M. Karaman, J. Hasler, and F. L. Degertekin, "Single-chip CMUT-on-CMOS front-end system for real-time volumetric IVUS and ICE imaging," *IEEE transactions on ultrasonics, ferroelectrics, and frequency control*, vol. 61, no. 2, pp. 239–250, 2014.

[41] X. Jin, O. Oralkan, F. L. Degertekin, and B. T. Khuri-Yakub, "Characterization of one-dimensional capacitive micromachined ultrasonic immersion transducer arrays," *IEEE Transactions on Ultrasonics, Ferroelectrics, and Frequency Control*, vol. 48, no. 3, pp. 750–760, 2001.

[42] K. Chen, H.-S. Lee, and C. G. Sodini, "A column-row-parallel ASIC architecture for 3-D portable medical ultrasonic imaging," *IEEE Journal of Solid-State Circuits*, vol. 51, no. 3, pp. 738–751, 2015.

[43] C. Pelekanakis, M. Stojanovic, and L. Freitag, "High rate acoustic link for underwater video transmission," in *Oceans 2003. Celebrating the Past... Teaming Toward the Future (IEEE Cat. No. 03CH37492)*, vol. 2. IEEE, 2003, pp. 1091–1097.

[44] J. Huang, S. Zhou, J. Huang, C. R. Berger, and P. Willett, "Progressive inter-carrier interference equalization for OFDM transmission over time-varying underwater acoustic channels," *IEEE Journal of Selected Topics in Signal Processing*, vol. 5, no. 8, pp. 1524–1536, 2011.

[45] K. Yadav, I. Kymissis, and P. R. Kinget, "A $4.4\mu W$ wake-up receiver using ultrasound data," *IEEE Journal of Solid-State Circuits*, vol. 48, no. 3, pp. 649–660, 2013.

[46] A. S. Rekhi and A. Arbabian, "A $14.5mm^2$ 8nW -59.7dBm-sensitivity ultrasonic wake-up receiver for power-, area-, and interference-constrained applications,"

in *Solid-State Circuits Conference-(ISSCC), 2018 IEEE International*. IEEE, 2018, pp. 454–456.

[47] S. Jeong, Y. Chen, T. Jang, J. M.-L. Tsai, D. Blaauw, H.-S. Kim, and D. Sylvester, "Always-on 12-nW acoustic sensing and object recognition microsystem for unattended ground sensor nodes," *IEEE Journal of Solid-State Circuits*, vol. 53, no. 1, pp. 261–274, 2017.

[48] A. S. Rekhi and A. Arbabian, "Ultrasonic wake-up with precharged transducers," *IEEE Journal of Solid-State Circuits*, vol. 54, no. 5, pp. 1475–1486, 2019.

[49] K. Yadav, I. Kymissis, and P. R. Kinget, "A 4.4 μW wake-up receiver using ultrasound data communications," in *VLSI Circuits (VLSIC), 2011 Symposium on*. IEEE, 2011, pp. 212–213.

[50] H. Fuketa, S. O′uchi, and T. Matsukawa, "A 0.3V 1μW super-regenerative ultrasound wake-up receiver with power scalability," *IEEE Transactions on Circuits and Systems II: Express Briefs*, vol. 64, no. 9, pp. 1027–1031, 2017.

[51] M. L. Wang, S. Baltsavias, T. C. Chang, M. J. Weber, J. Charthad, and A. Arbabian, "Wireless data links for next-generation networked microimplantables," in *2018 IEEE Custom Integrated Circuits Conference (CICC)*. IEEE, 2018, pp. 1–9.

[52] F. Mazzilli, C. Lafon, and C. Dehollain, "A 10.5 cm ultrasound link for deep implanted medical devices," *IEEE transactions on biomedical circuits and systems*, vol. 8, no. 5, pp. 738–750, 2014.

[53] M. I. Skolnik, *Introduction to RADAR systems*. McGraw-Hill, NY, 2001.

[54] W. M. Sansen, *Analog design essentials*. Springer Science & Business Media, 2007, vol. 859.

[55] P. Harpe, H. Gao, R. van Dommele, E. Cantatore, and A. H. van Roermund, "A 0.20 mm^2 3nW signal acquisition IC for miniature sensor nodes in 65 nm CMOS," *IEEE Journal of Solid-State Circuits*, vol. 51, no. 1, pp. 240–248, 2015.

[56] S. Schlupkothen, B. Prasse, and G. Ascheid, "Backtracking-based dynamic programming for resolving transmit ambiguities in wsn localization," *EURASIP Journal on Advances in Signal Processing*, vol. 2018, no. 1, p. 20, 2018.

[57] R. J. Przybyla, H.-Y. Tang, A. Guedes, S. E. Shelton, D. A. Horsley, and B. E. Boser, "3D ultrasonic rangefinder on a chip," *IEEE Journal of Solid-State Circuits*, vol. 50, no. 1, pp. 320–334, 2015.

[58] M. Kunita, M. Sudo, and T. Mochizuki, "Range measurement using ultrasound FMCW signals," in *2008 IEEE Ultrasonics Symposium*. IEEE, 2008, pp. 1366–1369.

[59] C. Medina, J. C. Segura, and S. Holm, "Feasibility of ultrasound positioning based on signal strength," in *2012 International Conference on Indoor Positioning and Indoor Navigation (IPIN)*. IEEE, 2012, pp. 1–9.

[60] C. Chen, Z. Chen, D. Bera, S. B. Raghunathan, M. Shabanimotlagh, E. Noothout, Z.-Y. Chang, J. Ponte, C. Prins, H. J. Vos *et al.*, "A front-end ASIC with receive sub-array beamforming integrated with a 32x32 PZT matrix transducer for 3-D transesophageal echocardiography," *IEEE Journal of Solid-State Circuits*, vol. 52, no. 4, pp. 994–1006, 2017.

[61] H.-Y. Tang, Y. Lu, X. Jiang, E. J. Ng, J. M. Tsai, D. A. Horsley, and B. E. Boser, "3-D ultrasonic fingerprint sensor-on-a-chip," *IEEE Journal of Solid-State Circuits*, vol. 51, no. 11, pp. 2522–2533, 2016.

[62] R. J. Przybyla, S. E. Shelton, A. Guedes, I. I. Izyumin, M. H. Kline, D. A. Horsley, and B. E. Boser, "In-air rangefinding with an aln piezoelectric micromachined ultrasound transducer," *IEEE Sensors Journal*, vol. 11, no. 11, pp. 2690–2697, 2011.

[63] J. Johansson, "Microelectronics for the thumb-size ultrasound measurement system," Ph.D. dissertation, Luleå tekniska universitet, 2004.

[64] G. Gurun, P. Hasler, and F. L. Degertekin, "Front-end receiver electronics for high-frequency monolithic CMUT-on-CMOS imaging arrays," *IEEE transactions on ultrasonics, ferroelectrics, and frequency control*, vol. 58, no. 8, pp. 1658–1668, 2011.

[65] T. Mitomo, N. Ono, H. Hoshino, Y. Yoshihara, O. Watanabe, and I. Seto, "A 77 GHz 90nm CMOS transceiver for FMCW radar applications," *IEEE journal of solid-state circuits*, vol. 45, no. 4, pp. 928–937, 2010.

[66] S. Suleymanov, "Design and implementation of an FMCW radar signal processing module for automotive applications," Master's thesis, University of Twente, 2016.

[67] S. Roehr, P. Gulden, and M. Vossiek, "Precise distance and velocity measurement for real time locating in multipath environments using a frequency-modulated continuous-wave secondary radar approach," *IEEE Transactions on Microwave Theory and Techniques*, vol. 56, no. 10, pp. 2329–2339, 2008.

[68] L. Battaglini, M. Ricci, and L. Senni, "Frequency modulated continuous wave ultrasonic radar," in *2013 18th International Conference on Digital Signal Processing (DSP)*. IEEE, 2013, pp. 1–8.

[69] M. Kunita, M. Sudo, S. Inoue, and M. Akahane, "A new method for blood velocity measurements using ultrasound FMCW signals," *IEEE transactions on ultrasonics, ferroelectrics, and frequency control*, vol. 57, no. 5, pp. 1064–1076, 2010.

[70] Texas-Instruments, *Understanding CW Mode for Ultrasound AFE Devices*, Texas Instruments, 2017, application Note SLOA253.

[71] F. Lampel, R. F. Tigrek, A. Alvarado, and F. M. Willems, "A performance enhancement technique for a joint FMCW radcom system," in *2019 16th European Radar Conference (EuRAD)*. IEEE, 2019, pp. 169–172.

[72] S. O. Piper, "Homodyne FMCW radar range resolution effects with sinusoidal nonlinearities in the frequency sweep," in *Proceedings International Radar Conference*. IEEE, 1995, pp. 563–567.

[73] V. Winkler, "Range doppler detection for automotive FMCW radars," in *2007 European Radar Conference*, 2007, pp. 166–169.

[74] L. Laughlin, C. Zhang, M. A. Beach, K. A. Morris, J. L. Haine, M. K. Khan, and M. McCullagh, "Tunable frequency-division duplex RF front end using electrical balance and active cancellation," *IEEE Transactions on Microwave Theory and Techniques*, vol. 66, no. 12, pp. 5812–5824, 2018.

[75] P. Barrenechea, F. Elferink, and J. Janssen, "FMCW radar with broadband communication capability," in *2007 European Radar Conference*. IEEE, 2007, pp. 130–133.

[76] Q. Dong, Y. Kim, I. Lee, M. Choi, Z. Li, J. Wang, K. Yang, Y.-P. Chen, J. Dong, M. Cho *et al.*, "11.2 a 1Mb embedded NOR flash memory with 39μW program power for mm-scale high-temperature sensor nodes," in *2017 IEEE International Solid-State Circuits Conference (ISSCC)*. IEEE, 2017, pp. 198–199.

[77] S. C. Bartling, S. Khanna, M. P. Clinton, S. R. Summerfelt, J. A. Rodriguez, and H. P. McAdams, "An 8MHz 75μA/MHz zero-leakage non-volatile logic-based Cortex-M0 MCU SoC exhibiting 100% digital state retention at VDD= 0V with $<$ 400ns wakeup and sleep transitions," in *2013 IEEE International Solid-State Circuits Conference Digest of Technical Papers*. IEEE, 2013, pp. 432–433.

[78] M. L. Nayyar *et al.*, *Piping handbook*. Mcgraw-hill New York, 1992, vol. 1, no. 45370771.

[79] C. Chen, Z. Chen, Z.-y. Chang, and M. A. Pertijs, "A compact 0.135-mW/channel LNA array for piezoelectric ultrasound transducers," in *European Solid-State Circuits Conference (ESSCIRC), ESSCIRC 2015-41st*. IEEE, 2015, pp. 404–407.

[80] J. Tillak and J. Yoo, "A 23μW digitally controlled pMUT interface circuit for doppler ultrasound imaging," in *2015 IEEE International Symposium on Circuits and Systems (ISCAS)*. IEEE, 2015, pp. 1618–1621.

[81] P. Wang and T. Ytterdal, "A 54 μW inverter-based low-noise single-ended to differential VGA for second harmonic ultrasound probes in 65-nm CMOS," *IEEE Transactions on Circuits and Systems II: Express Briefs*, vol. 63, no. 7, pp. 623–627, 2016.

[82] S.-J. Jung, S.-K. Hong, and O.-K. Kwon, "Low-power low-noise amplifier using attenuation-adaptive noise control for ultrasound imaging systems," *IEEE Transactions on Biomedical Circuits and Systems*, vol. 11, no. 1, pp. 108–116, 2016.

[83] S. Song, M. J. Rooijakkers, P. Harpe, C. Rabotti, M. Mischi, A. H. van Roermund, and E. Cantatore, "A 430nW 64nV/$\sqrt{Hz}$ current-reuse telescopic amplifier for neural recording applications," in *2013 IEEE Biomedical Circuits and Systems Conference (BioCAS)*. IEEE, 2013, pp. 322–325.

[84] S. Lee, W. Jo, S. Song, and Y. Chae, "A 300-μW audio $\Delta\Sigma$ modulator with 100.5-dB DR using dynamic bias inverter," *IEEE Transactions on Circuits and Systems I: Regular Papers*, vol. 63, no. 11, pp. 1866–1875, 2016.

[85] L. Lv, X. Zhou, Z. Qiao, and Q. Li, "Inverter-based subthreshold amplifier techniques and their application in 0.3-V $\Delta\Sigma$ modulators," *IEEE Journal of Solid-State Circuits*, vol. 54, no. 5, pp. 1436–1445, 2019.

[86] J. Holleman and B. Otis, "A sub-microwatt low-noise amplifier for neural recording," in *2007 29th Annual International Conference of the IEEE Engineering in Medicine and Biology Society*. IEEE, 2007, pp. 3930–3933.

[87] S. Robert, O. Abed-Meraim, and L. L. Coco, "Wide-band variable-gain LNA in 65 nm CMOS with inverter based amplifier for multi-tuners cable TV reception," in *2009 Proceedings of ESSCIRC*. IEEE, 2009, pp. 104–107.

[88] J. W. Park and B. Razavi, "20.8 a 20mW GSM/WCDMA receiver with RF channel selection," in *2014 IEEE International Solid-State Circuits Conference Digest of Technical Papers (ISSCC)*. IEEE, 2014, pp. 356–357.

[89] L. Svensson and J. Koller, "Driving a capacitative load without dissipating fCV^2, 1994 IEEE Symp. on Low Power Electronics, Digest of Tech," 1994.

[90] K. Chen, H.-S. Lee, A. P. Chandrakasan, and C. G. Sodini, "Ultrasonic imaging transceiver design for CMUT: A three-level 30-Vpp pulse-shaping pulser with improved efficiency and a noise-optimized receiver," *IEEE Journal of Solid-State Circuits*, vol. 48, no. 11, pp. 2734–2745, 2013.

[91] M. D. Seeman and S. R. Sanders, "Analysis and optimization of switched-capacitor DC-DC converters," *IEEE Transactions on Power Electronics*, vol. 23, no. 2, pp. 841–851, 2008.

[92] G. Berkol, P. G. M. Baltus, P. J. A. Harpe, and E. Cantatore, "A- 81.6 dBm sensitivity ultrasound transceiver in 65nm CMOS for symmetrical data-links," in *ESSCIRC 2019-IEEE 45th European Solid State Circuits Conference (ESSCIRC)*. IEEE, 2019, pp. 145–148.

[93] B. Razavi, *RF Microelectronics (Prentice Hall Communications Engineering and Emerging Technologies Series)*. Prentice Hall Press, 2011.

[94] R. M. Gray and D. L. Neuhoff, "Quantization," *IEEE Transactions on Information Theory*, vol. 44, no. 6, pp. 2325–2383, 1998.

[95] H. Attarzadeh, Y. Xu, and T. Ytterdal, "A low-power high-dynamic-range receiver system for in-probe 3-D ultrasonic imaging," *IEEE Transactions on Biomedical Circuits and Systems*, vol. 11, no. 5, pp. 1053–1064, 2017.

[96] J. Lim, C. Tekes, F. L. Degertekin, and M. Ghovanloo, "Towards a reduced-wire interface for CMUT-based intravascular ultrasound imaging systems," *IEEE Transactions on Biomedical Circuits and Systems*, vol. 11, no. 2, pp. 400–410, 2017.

[97] P. Behnamfar, R. Molavi, and S. Mirabbasi, "Transceiver design for CMUT-based super-resolution ultrasound imaging," *IEEE Transactions on Biomedical Circuits and Systems*, vol. 10, no. 2, pp. 383–393, 2016.

[98] *Effects of Anthropogenic Noise on Animals*. Springer Handbook of Auditory Research, 2018, pp. 119–120.

[99] K. Choi, H. G. Yeo, H. Choi, and D. Jee, "A 28.7V modular supply multiplying pulser with 75.4% power reduction relative to CV^2f," *IEEE Transactions on Circuits and Systems II: Express Briefs*, pp. 1–1, 2020.

[100] G. Jung, C. Tekes, M. W. Rashid, T. M. Carpenter, D. Cowell, S. Freear, F. L. Degertekin, and M. Ghovanloo, "A reduced-wire ICE catheter ASIC with Tx beamforming and Rx time-division multiplexing," *IEEE Transactions on Biomedical Circuits and Systems*, vol. 12, no. 6, pp. 1246–1255, 2018.

[101] O. Farhanieh, A. Sahafi, R. Bardhan Roy, A. S. Ergun, and A. Bozkurt, "Integrated HIFU drive system on a chip for CMUT-based catheter ablation system," *IEEE Transactions on Biomedical Circuits and Systems*, vol. 11, no. 3, pp. 534–546, 2017.

[102] N. Weste, D. Harris, and C. V. Design, "A circuits and systems perspective," 2010.

[103] H. Wang and P. P. Mercier, "A 1.6%/V 124.2 pW 9.3 Hz relaxation oscillator featuring a 49.7 pW voltage and current reference generator," in *ESSCIRC 2017-43rd IEEE European Solid State Circuits Conference*. IEEE, 2017, pp. 99–102.

[104] C. Kuratli and Q. Huang, "A CMOS ultrasound range-finder microsystem," *IEEE Journal of solid-state circuits*, vol. 35, no. 12, pp. 2005–2017, 2000.

[105] S. Moazzeni, M. Sawan, and G. E. Cowan, "An ultra-low-power energy-efficient dual-mode wake-up receiver," *IEEE Transactions on Circuits and Systems I: Regular Papers*, vol. 62, no. 2, pp. 517–526, 2015.

[106] M. Stojanovic, "On the relationship between capacity and distance in an underwater acoustic communication channel," *ACM SIGMOBILE Mobile Computing and Communications Review*, vol. 11, no. 4, pp. 34–43, 2007.

[107] I. Lee, D. Sylvester, and D. Blaauw, "A constant energy-per-cycle ring oscillator over a wide frequency range for wireless sensor nodes," *IEEE journal of solid-state circuits*, vol. 51, no. 3, pp. 697–711, 2016.

[108] R. J. Urick, *Principles of underwater sound for engineers*. Tata McGraw-Hill Education, 1967.

[109] H.-Y. Tang, D. Seo, U. Singhal, X. Li, M. M. Maharbiz, E. Alon, and B. E. Boser, "Miniaturizing ultrasonic system for portable health care and fitness," *IEEE transactions on biomedical circuits and systems*, vol. 9, no. 6, pp. 767–776, 2015.

[110] M. C. Domingo, "Overview of channel models for underwater wireless communication networks," *Physical Communication*, vol. 1, no. 3, pp. 163–182, 2008.

[111] BII7519FB. (2018) Benthowave instrument inc. communication transducer. [Online]. Available: http://www.benthowave.com/products/BII-7510communicationtransducer.html

[112] X. Huang, G. Dolmans, H. de Groot, and J. R. Long, "Noise and sensitivity in RF envelope detection receivers," *IEEE Transactions on Circuits and Systems II: Express Briefs*, vol. 60, no. 10, pp. 637–641, 2013.

List of publications

1. **G. Berkol**, P. G. M. Baltus, and E. Cantatore, "An Ultrasound Rangefinder System and Distance Measurement Technique based on a Harmonic FMCW Method." Submitted to Dutch Patent Office

2. **G. Berkol**, P. G. M. Baltus, P. J. A. Harpe and E. Cantatore, "A 1.25μJ per Measurement Ultrasound Rangefinder System in 65nm CMOS for Explorations with a Swarm of Sensor Nodes." Accepted for publication in IEEE Transactions on Circuits and Systems-1

3. **G. Berkol**, P. G. M. Baltus, P. J. A. Harpe and E. Cantatore, "A 2.67μJ per Measurement FMCW Ultrasound Rangefinder System for the Exploration of Enclosed Environments," in IEEE Solid-State Circuits Letters, 2020, vol. 3, pp. 326-329

4. **G. Berkol**, P. G. M. Baltus, P. J. A. Harpe and E. Cantatore, "A 81.6dBm Sensitivity Ultrasound Transceiver in 65nm CMOS for Symmetrical Data-Links," ESSCIRC 2019 - IEEE 45th European Solid State Circuits Conference (ESSCIRC), Cracow, Poland, 2019, pp. 145-148

5. E. Afacan, **G. Berkol** and G. Dündar, "Post-Silicon Validation of Yield-Aware Analog Circuit Synthesis," 2019 16th International Conference on Synthesis, Modeling, Analysis and Simulation Methods and Applications to Circuit Design (SMACD), Lausanne, Switzerland, 2019, pp. 245-248

6. **G. Berkol**, P. G. M. Baltus, P. J. A. Harpe and E. Cantatore, "An Ultrasound Transceiver in 65nm CMOS." 2019 Annual Conference on Integrated Circuit (IC) Design (ProRISC 2019), Delft, The Netherlands (presentation).

7. **G. Berkol**, P. G. M. Baltus, P. J. A. Harpe and E. Cantatore, "A Low Power Ultrasound Communication Link." 2018 Annual Conference on Integrated Circuit (IC) Design (ProRISC 2018), Enschede, The Netherlands (poster).

8. **G. Berkol**, P. G. M. Baltus, P. J. A. Harpe and E. Cantatore, "Design of a Low-power Ultrasound Transceiver for Underwater Sensor Networks," 2018 14th Conference on Ph.D. Research in Microelectronics and Electronics (PRIME), Prague, 2018, pp. 129-132

9. M. Andraud, **G. Berkol**, J. De Roose, S. Gannavarapu, H. Xin, E. Cantatore, P.J.A. Harpe, M. Verhelst, P.G.M. Baltus, "Exploring the Unknown through Successive Generations of Low-power and Low-resource Versatile Agents," Design, Automation & Test in Europe Conference & Exhibition (DATE), 2017, Lausanne, 2017, pp. 290-293

10. **G. Berkol**, E. Afacan, G. Dündar and E. V. Fernandez, "A Hierarchical Design Automation Concept for Analog Circuits," 2016 IEEE International Conference on Electronics, Circuits and Systems (ICECS), Monte Carlo, 2016, pp. 133-136

11. M. O. Saglamdemir, **G. Berkol**, G. Dündar, A. Sen, "An Analog Behavioral Equivalence Boundary Search methodology for Simulink models and Circuit level Designs Utilizing Evolutionary Computation," Integration, Volume 55, 2016, pp. 366-375 ISSN 0167-9260

12. E. Afacan, **G. Berkol**, G. Dündar, A. E. Pusane, F. Bakaya, "A Lifetime-aware Analog Circuit Sizing Tool," Integration, Volume 55, 2016, pp. 349-356, ISSN 0167-9260

13. E. Afacan, **G. Berkol**, G. Dündar, A. E. Pusane, F. Bakaya, "An Analog Circuit Synthesis Tool based on Efficient and Reliable Yield Estimation," Microelectronics Journal, Volume 54, 2016, pp. 14-22, ISSN 0026-2692

14. E. Afacan, **G. Berkol**, G. Dündar, A. E. Pusane and F. Bakaya, "A Deterministic Aging Simulator and an Analog Circuit Sizing Tool Robust to Aging Phenomena," 2015 International Conference on Synthesis, Modeling, Analysis and Simulation Methods and Applications to Circuit Design (SMACD), Istanbul, 2015, pp. 1-4

15. **G. Berkol** et al., "A Two-step Layout-in-the-loop Design Automation Tool," 2015 IEEE 13th International New Circuits and Systems Conference (NEWCAS), Grenoble, 2015, pp. 1-4

16. **G. Berkol**, E. Afacan, G. Dündar, A. E. Pusane and F. Bakaya, "A Novel Yield-aware Multi-objective Analog Circuit Optimization Tool," 2015 IEEE International Symposium on Circuits and Systems (ISCAS), Lisbon, 2015, pp. 2652-2655

17. E. Afacan, **G. Berkol**, A. E. Pusane, G. Dündar and F. Bakaya, "A Hybrid Quasi Monte Carlo Method for Yield-aware Analog Circuit Sizing Tool," 2015 Design, Automation & Test in Europe Conference & Exhibition (DATE), Grenoble, 2015, pp. 1225-1228

18. E. Afacan, **G. Berkol**, A. E. Pusane, G. Dündar and F. Bakaya, "Adaptive sized Quasi-Monte Carlo based Yield-aware Analog Circuit Optimization Tool," 2014 5th European Workshop on CMOS Variability (VARI), Palma de Mallorca, 2014, pp. 1-6

19. E. Afacan, **G. Berkol**, F. Bakaya and G. Dündar, "Sensitivity based Methodologies for Process Variation aware Analog IC Optimization," 2014 10th Conference on Ph.D. Research in Microelectronics and Electronics (PRIME), Grenoble, 2014, pp. 1-4

Summary
Architecture and IC Implementation of Ultrasound Communication and Rangefinder Systems for Sensor Swarms

This thesis studies swarms of sensors able to communicate and measure reciprocal distances using ultrasound waves. In the context of this work, novel system architectures and circuit level techniques suited for resource-limited sensor nodes in a swarm have been proposed.

Chapter 1 introduces the go-with-the-flow approach to enable collecting distance measurement data among resource-limited sensor nodes injected into fluid-filled volumes to explore. These data will be used to extract information about the geometry of the volumes explored by a swarm of sensors.

Chapter 2 analyzes the main system-level challenges in the implementation of ultrasound communication and range-finding systems when the sensor nodes operate in an enclosed volume. Two novel Frequency-Division Duplexing (FDD) Frequency Modulated Continuous Wave (FMCW)-based ultrasound rangefinder methods for distance measurements are then presented, together with a study of their system level implementation. The first rangefinder system is based on exchanging properly designated chirp signals. The second system is a wake-up based rangefinder system, where a separate wake-up link has been used in addition to the ranging link to decrease the always-on power consumption of the nodes. Both proposed FDD-FMCW based rangefinder systems address the challenges related to collision and multipath phenomena without the need of a global synchronization among the elements of the swarm.

Chapter 3 presents the design of three critical interface circuits for the implementation of the systems discussed in Chapter 2: low-noise amplifier, transmitter, and wake-up receiver. The low-noise amplifier exploits a novel DC feedback method enabling to stabilize the DC output voltage of single-ended inverter-based amplifiers. An energy-efficient four-level transmitter is implemented to reduce the power consumption of

ultrasound transmitters. Finally, an ultra-low power wake-up receiver design principle enabling a moderate sensitivity while dissipating ultra-low-power is discussed.

Chapter 4 summarizes the main experimental results obtained with the proposed ultrasound communication and rangefinder systems. The ultrasound data transceiver exploits an OOK modulation scheme and enables a 1kbps data-rate with state-of-the-art sensitivity (-81.6dBm) and energy per bit (51.18nJ/b). The measurement results of the rangefinder system with a chirp exchange result in a $2.67\mu J$ energy per distance measurement and a ranging resolution of 6.5mm up to 1m distance in air. To lower the always-on power consumption and energy per measurement, a wake-up based rangefinder system is proposed, where the nodes use a wake-up receiver and an energy efficient four-level transmitter. The wake-up based rangefinder system achieves a $1.25\mu J$ energy per distance measurement and a ranging resolution of 18.7mm up to 1m in air with an always-on power consumption of only 23.6nW.

Chapter 5 presents the conclusions of this work, considering the results achieved by the experimental characterization of custom IC-based implementations of the energy-efficient ultrasound communication link, and of the two novel rangefinder systems. In addition, a list of possible future improvements to the work described is provided.

In the appendices of this thesis, four scientific publications are included. The chapters in the thesis present a concise but thorough overview of the research carried out in the context of this thesis, while the readers are referred to the papers in the appendices for more detailed discussion of design, implementation, and experimental characterization.

Acknowledgment

I dedicate this thesis to the memory of my dear mother, Selma. Her vision, discipline, and unconditional love and trust have made me the person I am today. I would like to express my deepest gratitude to my father, Tayfun, who was supportive and encouraging throughout my life. I have always felt the love of my parents and considered myself very lucky to have such a caring family. My best friend, who also happened to be my beloved wife, Tuğçe, was always there for me during these last five years with great patience. I am grateful to have you by my side, your love and affection have been the key driving force during my doctoral journey.

When pursuing a doctoral degree in microelectronics, one may encounter many challenging roadblocks, e.g. uncommon DRC-LVS errors during the last day of a tape-out, delays in receiving the dies, uncalibrated measurement equipment, PCB shorts, never-ending electrical characterizations, 50Hz noise from an unknown origin, incorrect bond-wires, among others. Words are not enough to describe my profound appreciation to Prof. Eugenio Cantatore, who was with me during these darkest times. I am grateful that I find an opportunity to be a doctoral student of such an amazing researcher with admirable background not only in electrical engineering but in science. He has a unique "scientific eye" and reasoning, which tremendously contributed to my development as a researcher. He had been a great mentor to me in every dimension of this work. My doctoral journey comprises indeed many peaks and valleys (mostly valleys), however, thanks to the immense guidance, patience, and effort of Eugenio, I was able to find my way out of the valleys. He is a source of inspiration with his smart ideas and alternative solutions to the problems we encounter, which helped me to complete this work. *His review of scientific publications is a form of art*, and I learned significantly throughout the years that I had the privilege to work with him. Eugenio and I, together, have been through long working hours and countless discussions on weekends, build a setup at my home during the pandemic, prepare countless iterations of paper revisions due to my poor placing of *a/an/the*, submit papers as well as finalize the layout of circuits, on the last minute of the deadline, and many more. During these times, Eugenio was always full of motivation and determination, and more importantly, had everlasting patience with me despite my stubbornness. I am aware that the endeavor may felt Sisyphian at times, and I am grateful for his efforts in helping me to become a better researcher.

My doctoral journey owes a great deal to many other figures of inspiration, guidance, and support. I have had the luck to work together with Dr. Pieter Harpe and Prof. Peter Baltus through my years at TU Eindhoven. Pieter has made significant contributions to my tapeouts and publications, and I am grateful for his time and effort. Without his guidance, it would have been impossible to complete a tapeout. Pieter gently combines his calm and kind attitude with his admirable expertise in analog circuits, which makes him an excellent supervisor. Besides the supervision, he is an excellent analog designer as well, and always open to share his ideas with his students while actively participating the design process. This is something very unique, which improves the quality of the research significantly. I really appreciate that I had the chance to work with such a great researcher that I see as a role model. Likewise, Peter is a great source of inspiration. He is an excellent manager with admirably broad range of scientific interests. On one hand, one can be really surprised to learn how busy he is as the Chair of the IC group. On the other hand, he is also very accessible and always finds time for the students (e.g. one may gently ask to have a coffee meeting). In fact, Peter was the one who led me towards investigating a new ranging method, which we discussed in detail during one of our many coffee meetings. I consider this incident as a milestone in my doctoral study, and I would like to thank sincerely Peter for his guidance, support, patience, and faith in me, which enabled me to complete this work. I would like to thank Prof. Marion Matters-Kammerer, Prof. Patrick Reynaert, and Dr. Michiel Pertijs for being part of the jury for my doctoral defense.

During my master study at Bogazici University, I had the chance to work with a great mentor, Prof. Günhan Dündar, whose support, guidance, and faith in me have made me the researcher I am today. He is the reason that I focused on the microelectronics field and I have learned from him all the necessary ingredients needed to pursue my academic career. His personality and wisdom will always be a reference in my life. I wish to express my sincere gratitude to my big (i.e. elderly) brother, great supervisor, Dr. Engin Afacan. It was my luck to have such a great role model early in my career, whose impressive discipline and work ethic set a good example to me. It was, and always will be, a great pleasure to work with him. Indeed, good people of BETA Lab; Okan, Gürkan, Ismail, Emre, Ozan, Hikmet, Naci, Berk, Melih, Iskender, Kemal, Burcu, Ece, Seyhan, and many others, are a huge family wherever they are in the world.

I would like to extend my gratitude to the colleagues that make my journey much more fun. Thank you, Margot, for all of your efforts, I appreciate the special relationship we have over the past years and you will always have a special place in my heart. Thank you, Rainier, I appreciate your professionalism and expertise in solving many nasty issues in Cadence. I appreciate the support of Georgi, Dusan, and Heinrich; I learned a lot by assisting their courses and enjoyed deeply our kind conversations. My dearest office mates; Kevin, Haoming, Corne, Xi, Xiao, Yijing, Meiyi, Dirkjan, and Noortje, over the years we develop a strong friendship and withstand all of the

challenges of the work and the Dutch food together. A special thanks to the dearest friends of the IC Group; Sahel, Martin, Juan, Marco, Carlos, Lammert, Joost, Debashis 1 & 2, Enrico, Marios, Pavlos, Carmine, James, Qilong, Yuting, Hanyue, Piyush, Zulqar, and many others. We have collected many good memories and had many pleasant events. May your reviewers always be easygoing, your tapeouts be swift, your chips be typical-typical, and your measurements be identical to your simulations.

Last but definitely not the least, I would like to thank my friends who improve the quality of my life and contributed to me in a way I could never imagine. Yunus and Ismail; you guys opened a new era of entertainment for me. I consider our time together as a milestone. Tunç and Nehir Berk; you guys were always there for me and I will never forget your companionship when I needed the most. I appreciate all the good memories we collected over the years with Orhan, Berk, Cem, Semih, Dilge and Yankı. Even though we may be far away, I always felt the support and friendship of the *Izmir Kemik Tayfa*; Anıl, Faik, Emre, Mehmet Fatih, Güray, Erkan, Ali, Onuralp and Dinçer, and my dearest lifelong friends; Furkan and Yağmur, Fatih and Ece, Oğuz and Kübra, I never felt alone thanks to you all.

Biography

Gönenç Berkol was born in 1991, in Izmir, Turkey. He received the B.Sc. (top three) and M.Sc. degree in electrical & electronics engineering from Ege University, Izmir, Turkey, in 2013, and Bogazici University, Istanbul, Turkey, in 2015, respectively. He completed the M.Sc. program in the Electronics group, BETA Lab with the thesis entitled "Novel Design Methods for Analog Design Automation Tools".
In 2016, he started a PhD-student position at the IC Group, Eindhoven University of Technology on the Phoenix Project of which the results are presented in this dissertation. His research interests include low-power low-noise analog integrated-circuit design and design automation tools for analog circuits.

Appendices

Appendix A

A 1.25μJ per Measurement Ultrasonic Rangefinder System in 65nm CMOS for the Exploration with Swarm of Sensor Nodes

Gönenç Berkol, Peter G. M. Baltus, Pieter J. A. Harpe, and Eugenio Cantatore

Accepted for publication in IEEE Transactions on Circuits and Systems-1

This paper presents an ultrasound rangefinder system able to find relative distances among energy-constrained sensor nodes. The nodes build a swarm that is operated in collision and multipath rich environments. A new distance measurement technique combining Wake-up and Frequency Modulated Continuous Wave (FMCW) is proposed to enable the ranging while neglecting the echoes from passive reflectors in the environment. The building blocks of the sensor nodes comprise a transmitter, a wake-up receiver, and a ranging receiver, all implemented in a 65nm CMOS technology. The transmitter includes two switched-capacitor converters and an output multiplexer to generate a four-level driving signal and broadcast either a wake-up sequence or a digitally synthesized ultrasound Chirp. The transmitter dissipates 0.43μJ and 0.82μJ to broadcast the wake-up signal and the Chirp, respectively. A mixer first architecture is exploited in the wake-up receiver to reduce the always-on power consumption of the nodes. The ranging receiver uses a heterodyne architecture suited for the FMCW. The power consumption of the wake-up receiver and ranging receiver is 23.6nW and 0.56μW, respectively. The proposed rangefinder is experimentally characterized up to a 1m distance in air and dissipates 1.25μJ per measurement, achieving a resolution of 18.7mm at 0.55m.

Ultrasound rangefinder, Ultrasound front-end, Ultrasound receiver, Analog IC, Swarm of sensor nodes

A.1 Introduction

Ultrasound (US) has been used in emerging applications for the exploration of the ocean floor [12], underground infrastructures [36], water distribution systems, and industrial tanks for processing chemicals [9,11,13,29,30]. In these applications different fluidic environments are explored with a swarm of sensor nodes, to gather data on the shape and dimensions of enclosed volumes that are missing GPS coverage. Sensors should be autonomous as human intervention during the exploration is not possible. Miniaturized and energy-constrained sensor nodes are needed considering the limited size of these environments. US is preferred for low bit-rate and energy efficient data exchange and ranging between the nodes, as US propagates with a lower attenuation in fluids compared to RF [33]. The nodes are injected into the volume to explore and perform distance measurements among them while going with the flow of the medium [10]. Their mutual distance measurements are recorded to their memory as they traverse the volume. These data are analyzed after recuperating the sensor nodes. Data post-processing is performed at central computing stations [7, 14], to extract information about the geometry of the volumes explored by the swarm, based on the mutual distance measurements performed.

Most ranging methods proposed in literature [23] are based on either using additional hardware like GPS or having a beacon in the network that has the capability to communicate with the outside world and the other sensor nodes [24]. Both approaches are not suited for the applications considered in this paper. Moreover, the distance measurement methods that are based on Received Signal Strength Indicator (RSSI), and Time of Arrival (ToA) require a global network synchronization [25], together with highly stable timing sources (such as atomic clocks) and advanced MAC protocols [26] that require exchanging several data packets. These approaches are too power hungry for our applications. The Time Difference of Arrival (TDoA) based distance measurement methods take advantage of the different propagation speeds of US and RF in the operating medium. However, their maximum range is limited due to the attenuation of RF in fluids [33]. Typical US distance measurement methods exploit Time of Flight (ToF) of the US echoes coming from passive reflectors [95–97]. However, collisions and multipath propagation of the echoes experienced when the nodes are operated in an enclosed volume [21] increase the complexity of extracting distance information from the measurements and decrease the reliability when reconstructing the geometry of the explored volumes. As a result, a new distance measurement method able to cope with the echoes reflected from the boundary of the enclosed volumes while minimizing US data-exchange needed to support synchronization is required. To address the aforementioned challenges, a novel US rangefinder system based on a Wake-up and a Frequency Modulated Continuous Wave (FMCW) based ranging is proposed in this paper. An important feature of the proposed system is that the sensor nodes use a wake-up link, which provides ultra low power consumption, while the FMCW method is exploited in a ranging link to find the relative distance among the nodes in the swarm. Furthermore, the wake-up and FMCW ranging links use separate frequency bands, therefore passive reflections from the boundary of the enclosed volume

and active responses of the nodes can be easily distinguished. The paper is organized as follows: In Sections II and III, high-level system and circuit design are discussed. The detailed circuit implementation and the measurement results are presented in Section IV and Section V, respectively. The performance of the US rangefinder is benchmarked against prior art in Section VI and conclusions are provided in Section VII.

A.2 US Rangefinder System

A.2.1 System Operation

The proposed rangefinder system is based on identical sensor nodes. Their block diagram is depicted in Fig. A.1a, where each node consists of two off-chip piezoelectric transducers (PZT1 and PZT2); a transmitter (TX), a wake-up receiver (WURX), a ranging receiver (MAINRX) integrated on-chip, and a digital backend implemented on an FPGA. PZT1 and PZT2 are routed to corresponding hardware with an off-chip switching matrix. PZT1 and PZT2 have different resonance frequencies, thereby their operating frequency bands are separated. The nodes can be configured in two different modes of operation. The first one is called the initiator mode, where the node starts the ranging protocol to find its relative distance to the surrounding nodes. The second operating mode is called the wake-up mode. In this state, the sensor nodes listen to the environment via PZT1 and WURX. If the level of the incoming signal exceeds a pre-defined threshold, the nodes wake-up and transmit back a frequency-modulated response. The sensors operating in wake-up mode activate only their WURX, while TX and MAINRX are switched-off. Therefore, power consumption in this mode is extremely limited. Fig. A.1b demonstrates an example of the proposed rangefinder system, where the ranging between two sensor nodes, NODE1 and NODE2 at a distance R, together with the timing diagram illustrating the activation of the corresponding blocks in the nodes, are depicted. Here, NODE1 (in initiator mode) starts the ranging by broadcasting a $WURX_{code}$ to the environment via PZT1. At the same time, NODE1 activates its MAINRX to listen to the responses from the nearby nodes. The activation of the initiator mode is controlled via a Start input generated by the digital backend without any need for global synchronization in the network. As illustrated in Fig. A.1b, a digitally synthesized US signal, Chirp2r, is generated by the FPGA and used in NODE1 as a mixing signal in its MAINRX, which listens to PZT2. Chirp2r (Fig. A.2) is a frequency-modulated US signal whose frequency increases linearly with time in the interval 0 - T_{sweep}. Meanwhile, NODE2 is in the wake-up mode. The $WURX_{code}$ reaches NODE2 after a propagation delay $\frac{\tau_d}{2}$, is received by its PZT1 and transformed to a digital representation via WURX. This is followed by a digital comparison performed in the FPGA of NODE2. If the digital output of WURX exceeds a pre-defined threshold, the TX in NODE2 is immediately activated to broadcast a response, Chirp2t, via PZT2. Chirp2t is a frequency-modulated US signal identical to Chirp2r, which is digitally synthesized by the FPGA of NODE2.

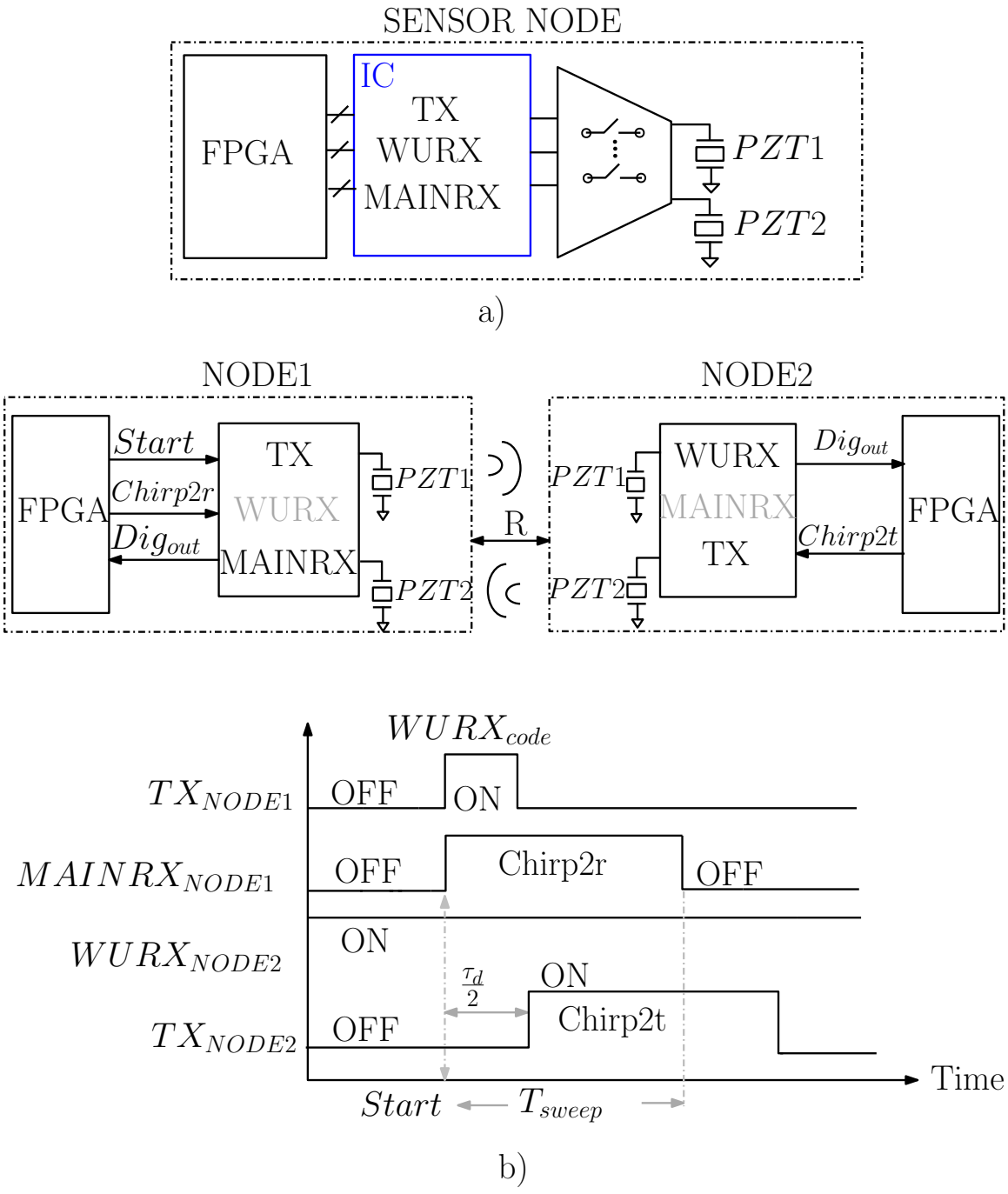

Figure A.1: a) Building blocks of the sensor node. b) Illustration of the proposed ranging concept including two sensor nodes, NODE1 and NODE2, which are activating their corresponding hardware (not to scale).

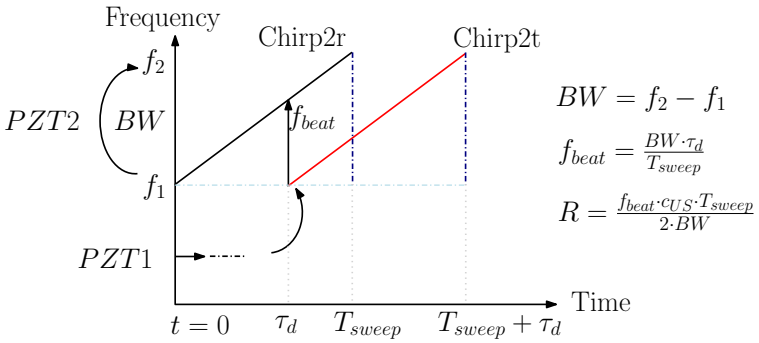

Figure A.2: Illustration of the proposed distance (R) measurement method in a frequency-time plot.

The duration as well as the operating frequency bands of Chirp2r and Chirp2t are equal and reside in the frequency band of PZT2. The only difference is that Chirp2r starts at the very moment that the ranging is initiated, while the response (Chirp2t) arriving from NODE2 is delayed by the round trip time of US. The delay τ_d in Fig. A.1b and A.2 corresponds to the round trip time of flight between the nodes and equals to $\frac{2R}{c_{US}}$, where R is the distance between the nodes and c_{US} is the speed of US in the medium. NODE1 records the signal obtained after mixing Chirp2r and Chirp2t in MAINRX to its memory. As shown in Fig. A.2, the spectrum of this signal will show a frequency peak, f_{beat}, corresponding to the time of flight τ_d of US traveling back and forth between NODE1 and NODE2. An important highlight of the proposed method is that the initial frequency, f_1, the stop frequency, f_2, as well as the duration, T_{sweep}, of the identical Chirps are known apriori and digitally synthesized in the nodes to fit inside the bandwidth of PZT2. As a result, the relative distance between NODE1 and NODE2 can be calculated with the knowledge of BW, T_{sweep}, and c_{US}, as shown in Fig. A.2. Since the proposed measurement method is only controlled by the initiator node, a global synchronization between the nodes is not needed. Clearly, the clocks needed for digital synthesis in the initiator and the wake-up nodes should be sufficiently accurate during the time T_{sweep}. However, this requirement is easy to achieve considering the rather short duration of T_{sweep} (which is typically in the order of milliseconds) and a typical short-term accuracy of real time clocks (RTCs) [70], which is better than 100ppm. A 100ppm variation in the RTCs used in the nodes would translate an error in T_{sweep} that is lower than 0.01%, which will thus not affect in an appreciable way the resolution of the ranging system. Thanks to the different frequency bands exploited for the wake-up signal $WURX_{code}$ sent by the initiator and the FMCW US signal sent back by the nodes that wake-up, the initiator node can distinguish echoes coming from passive reflectors from frequency-modulated response signals sent back by the nodes. This happens even if the wake-up nodes are approximately at a fixed distance from the initiator, and thus if no Doppler shift occurs. One should notice, indeed, that in the applications envisaged, the swarm of nodes is moving with the flow of the fluid, therefore the relative distances between the nodes are expected to change slowly in time. Furthermore, in case multiple sensor nodes

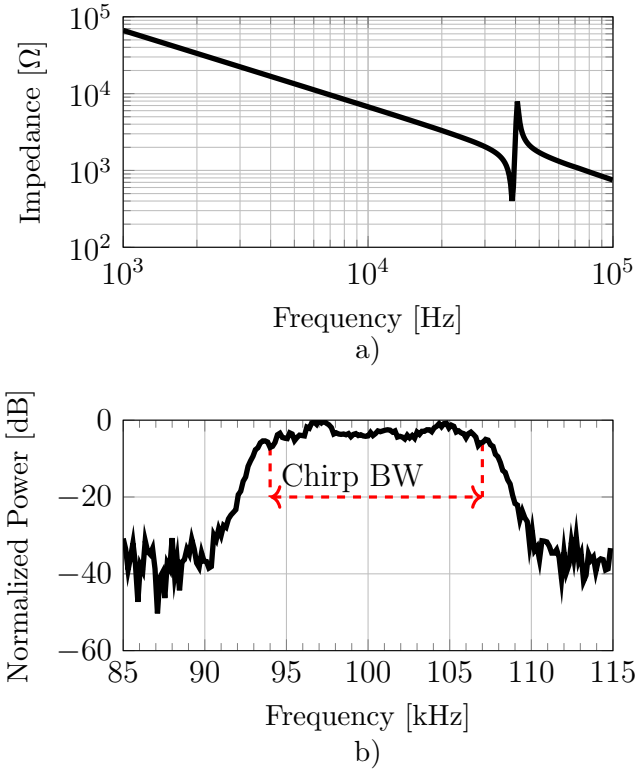

Figure A.3: a) Measured impedance plot of PZT1. The series resonance is at 39kHz. b) A link characterization from PZT2 to PZT2, where a bandwidth of 13kHz between 94kHz and 107kHz is found suitable for the Chirp signals.

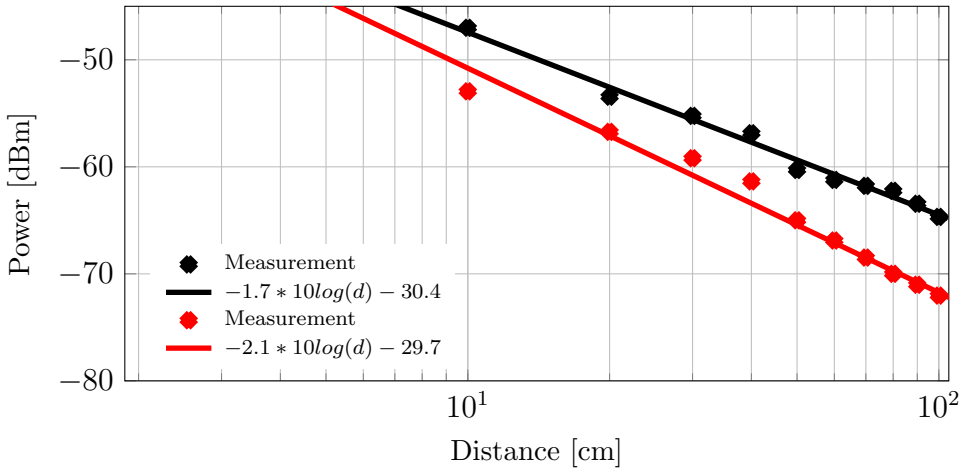

Figure A.4: Received power characterization in air for PZT2 (black, top) and PZT1 (red, bottom).

that are at different distances from NODE1 wake-up, their response will correspond to different beat frequencies that are separated in the frequency domain, and can be distinguished during post-processing [67]. Finally, an identification (ID) payload of

the woke-up node can be embedded in the response Chirp2t, for instance by amplitude modulation [75] or phase modulation [71]. This allows distinguishing between the first signal received by a node that wakes up and possible delayed version of the signal coming from the same node due to multipath propagation [67].

A.2.2 Transducer Characterization

Most of the applications considered in this paper use a fluidic medium, where the US propagates with much lower attenuation (<100x in water [98]) compared to air. However, due to the difficulty to measure at large distances in fluids, and thus to simplify the characterizations while keeping the maximum distance between the sensor nodes at a manageable level, the experimental setup of the proposed system has been built in air to demonstrate the proof-of-concept principle. Piezoelectric transducers (PZTs) have been used because of their availability in the market. PZTs typically have a nominal operating frequency spanning from a few tens of kHz to several hundreds of kHz with a relatively low bandwidth [19,99]. Although Capacitive Micromachined Ultrasound Transducers (CMUTs) have been used in literature [100] to achieve a larger bandwidth compared to PZTs, the high-voltage DC bias requirement of CMUTs [101] is an important drawback in battery-operated applications. Accordingly, PZT1 and PZT2 are chosen as commercially available piezoelectric transducers with a nominal resonance frequency of 40kHz and 100kHz, and an input capacitance of 2nF and 1nF, respectively [20]. Fig. A.3a shows an impedance measurement of PZT1, where its resonance frequency and the impedance at resonance are measured as 39kHz and 400Ω, respectively. Fig. A.3b shows the normalized received power for a link consisting of two identical PZT2 transducers, where the frequency band between 94kHz to 107kHz has been chosen for the Chirp signals. PZT2 is used in the FMCW ranging link, as a larger bandwidth in the Chirp signals is desired to improve the theoretical range resolution [67]. The resonance frequency of PZT1 is used as a carrier frequency in the wake-up link to broadcast the $WURX_{code}$.

A.2.3 Link Budget Analysis and System Specifications

Power-loss in the propagation of US is investigated by building a test setup in air at room temperature, where PZT1 and PZT2 are driven with a $0.6V_{pp}$ burst signal at 39kHz and 100kHz, respectively, and the power received by an identical transducer is recorded up to 1m distance. Fig. A.4 shows this characterization, where the received power is modeled with the equation: $P_{rec} = -k \cdot 10log(d) + P_0$. Here, d is the distance in cm, k is the path loss coefficient, and P_0 is the initial power loss. The outcome of this characterization is reported in Fig. A.4, where the received powers of PZT1 and PZT2 at 1m distance are measured as $-72dBm$ and $-65dBm$, respectively. Although PZT1 has a lower resonance frequency, it is less directive compared to PZT2, which leads to a larger signal attenuation with distance. While it is possible to balance the received power of the links, for instance by reducing the driving voltage of PZT2,

Table A.1: System Specs

Parameter	Value
V_{DD}	0.6V
Max. distance in air	$\approx 1m$
SNR_{in}	>12dB
IRN_{WURX}	$<14\mu V_{rms}$
BW_{WURX}	$\approx 1kHz$
IRN_{MAINRX}	$<32\mu V_{rms}$
T_{sweep}	10ms
f_{beat}	<7.6kHz
BW_{MAINRX}	>10kHz

we have chosen to use a single 0.6V driving supply to avoid using an extra voltage regulator. At the input of the receivers ≈12dB SNR is sufficient to have a 90% detection probability with a $<10^{-3}$ false alarm ratio [53]. As summarized in Table A.1, this can be achieved when the integrated Input-Referred Noise (IRN) of the WURX and MAINRX is lower than $14\mu V_{rms}$ and $32\mu V_{rms}$, respectively. To reduce the always-on power consumption of the nodes, a low-complexity communication scheme (e.g. On Off Keying) with a limited data-rate (e.g $\leq 0.5kbps$) can be exploited in the wake-up link [17]. This allows allocating a ≈1kHz baseband bandwidth (BW_{WURX}), thus an Input-Referred Noise Density (IRND) of $443\frac{nV}{\sqrt{Hz}}$ for the WURX is estimated. The duration of the Chirp signals, T_{sweep}, has to be larger than the round trip time ($\approx 6ms$) among the sensors at the maximum specified measurement distance of 1m in air, therefore, T_{sweep} is chosen to be 10ms. The frequency band between 94kHz and 107kHz was chosen for the FMCW link, thus a 13kHz Chirp BW is used in the ranging. Accordingly, the smallest distance step that can be measured ($R_{min} = \frac{c_{US}}{2BW}$) in air is calculated as 13mm [67]. At 1m distance, an f_{beat} of ≈7.6kHz is estimated, which has to reside inside the BW of the MAINRX (BW_{MAINRX}). Therefore, by specifying at least 10kHz BW, an IRND of $320\frac{nV}{\sqrt{Hz}}$ for the MAINRX is calculated.

A.3 High Level Description of Hardware Blocks

US transducers can typically be modeled [60] by a series resonator (R_m, L_m, C_m) in parallel with a parasitic capacitor, C_p, as shown in Fig. A.5a. When driving piezoelectric transducers, a large amount of energy is dissipated to charge and discharge the large parasitic capacitance C_p. Using an inductance (mH range) to cancel out C_p requires large volumes and is thus impractical. To reduce capacitive losses, a well-known step-wise charging method [89], [90] has been used in literature. In this work, a similar method is chosen to drive the transducers PZT1 and PZT2. For each transducer, a step-wise charging/discharging using a multi-level driving signal is

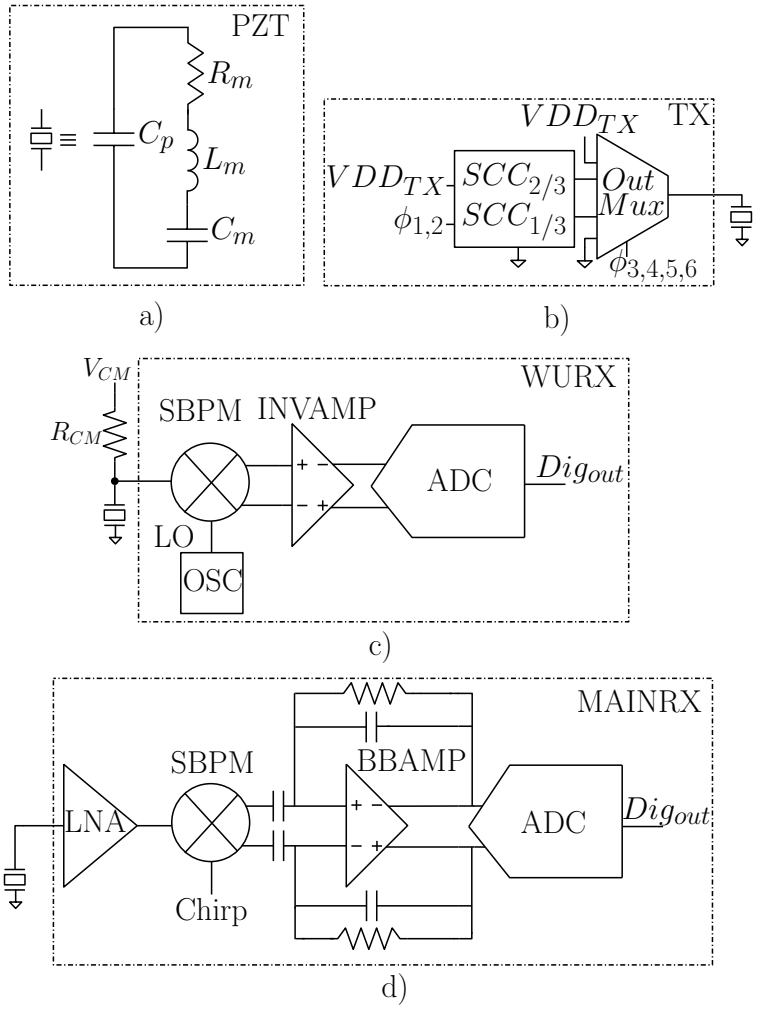

Figure A.5: a) Equivalent circuit model of a PZT transducer. b) Top-level circuit implementation of TX, c) WURX, d) MAINRX.

more energy-efficient than the conventional two-level driving scheme. On one hand, multi-level driving reduces the losses associated to charging and discharging the parasitic transducer capacitance. On the other hand, multi-level periodic signals have a higher ratio between the energy at the fundamental frequency and the energy in the harmonics. For this reason, multi-level signals can excite more efficiently the resonator branch of the transducer and transform electric energy into acoustic one. To realize an efficient transmitter, thus, a multi-level TX is used in this work, as shown in Fig. A.5b. A 4-level driving signal has been chosen, which is generated connecting the transducer periodically to VDD_{TX}, the maximum voltage level applied to the load, two intermediate voltage levels ($2/3 \cdot VDD_{TX}$ and $1/3 \cdot VDD_{TX}$), and ground. The intermediate DC voltage levels are obtained from VDD_{TX} by using two Switched-Capacitor Converters ($SCC_{1/3,2/3}$). These converters use two 50% duty-cycled non-overlapping clocks, $\phi_{1,2}$. Each DC level is connected to the transducer for

a time span and in an order that are controlled via the output multiplexer by the clocks $\phi_{3,..6}$.
As shown in Fig. A.5c, a mixer-first topology with a single-balanced passive mixer (SBPM) is used in the WURX to minimize the always-on power consumption of the nodes. Although the input-referred noise density of the front-end increases without an LNA preceding the mixer, the target integrated noise level is achievable with this topology by keeping a limited BW of 1kHz in the baseband amplifier. This is possible, as the transducer PZT1 is used at its resonance frequency, and only the fundamental component is needed to transmit the wake-up message. The SBPM does not consume DC power, but enables single-ended to differential conversion, thus providing a theoretical gain of 1.48dB [93]. After the SBPM, the WURX comprises an open-loop inverter-based baseband amplifier, INVAMP, and a 10-bit SAR ADC, which uses a similar design as reported in [55]. The down-conversion signal of the SBPM, LO, as well as the ADC clock, are provided by an on-chip oscillator, OSC. A single supply, V_{DD}, has been used in the WURX. The transducer is DC coupled to the front-end, and the DC common-mode bias of the front-end, $V_{CM} = V_{DD}/2$, is provided through an off-chip resistance, R_{CM}, of 5MΩ.
The MAINRX exploits a basic heterodyne architecture as shown in Fig. A.5d, which comprises a single-ended inverter-based low-noise amplifier (LNA), followed by an SBPM, a closed-loop baseband amplifier (BBAMP), and a 10-bit SAR ADC, all sharing the same supply, V_{DD}. The $Chirp$ needed for mixing is provided by the digital backend as a two-level square wave. The high-frequency harmonics of the SBPM are filtered out by the BBAMP, and the baseband signal is converted to the digital domain by the 10-bit SAR ADC [55]. A detailed report on the MAINRX can be found in [30], while some parts of this circuit are briefly discussed here for better readability.
A Xilinx Spartan-3 FPGA Board has been used as digital backend. The Chirp needed in the MAINRX and the output multiplexer control clocks of the TX, $\phi_{3,..6}$, are synthesized by reading at a constant rate (1MHz) suitable bit streams preloaded to a memory in the digital backend. The time reference is provided by an external 50MHz crystal oscillator available in the FPGA board, which in wake-up mode can be duty cycled using the wake up signal. All other timing signals needed in the nodes are derived from the same reference, except for the always active clocks in wake-up mode, which are directly derived from the on-chip oscillator OSC. Most of the digital signal processing, such as the FFT needed to determine the beat frequency in the FMCW ranging, are performed outside of the nodes. The output data generated from the MAINRX by mixing the Chirp signals during the ranging are thus saved to a memory in the digital backend.

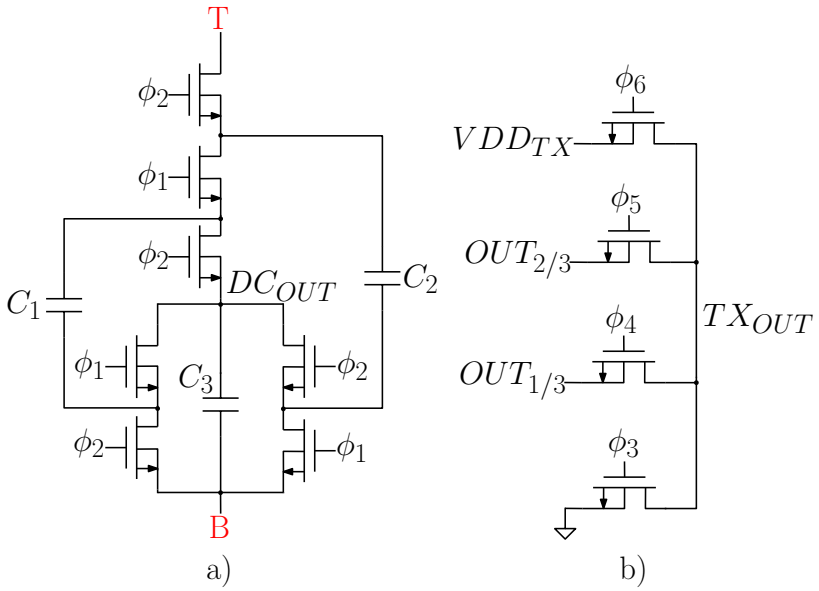

Figure A.6: Schematic of the a) Dickson converter, b) Output multiplexer.

A.4 Circuit Design

A.4.1 TX Circuit Design

An SCC can be modeled [91] as an ideal transformer (whose voltage ratio is defined by the SCC topology) in series with an output resistor, R_{out}. The DC level of the output of the TX is determined by the voltage division between R_{out} and the load impedance. In our implementation, R_{out} represents the output resistance of the corresponding SCCs with an additional series resistance due to the output multiplexer (Fig. A.5b). To reduce the power consumption of the TX, 0.6V is chosen as VDD_{TX}. Each clock phase ϕ is buffered to the switching transistors in the SSCs and output multiplexer by on-chip drivers, which use a $VDD_{driver} = 1.2V$ supply. The transistor-level implementation of the TX is shown in Fig. A.6. All switches are implemented using insulated well nMOS transistors. A Dickson topology is chosen to implement the SCCs, since the same topology can be reused to obtain the intermediate voltage levels with a minor change in top-level connection. As shown in Fig. A.6a, a voltage conversion ratio of 3:1 is obtained when VDD_{TX} and ground are connected to the top node, T, and the bottom node, B, respectively. The division ratio of 3:2 is obtained by interchanging the top node and the bottom node. The SCC output node is marked DC_{out} in Fig. A.6a. $OUT_{1/3}$ and $OUT_{2/3}$ correspond to the output of $SCC_{1/3}$ and $SCC_{2/3}$, respectively. The capacitors $C_{1,2,3}$ are off-chip flying capacitors. The output multiplexer comprises 4 NMOS transistors that connect the desired DC voltage to the transducer load, as shown in Fig. A.6b. An NMOS transistor is chosen to build the switches due to its lower combined conduction and switching losses compared to a PMOS transistor with a similar overdrive voltage. A deep-NWELL transistor with a

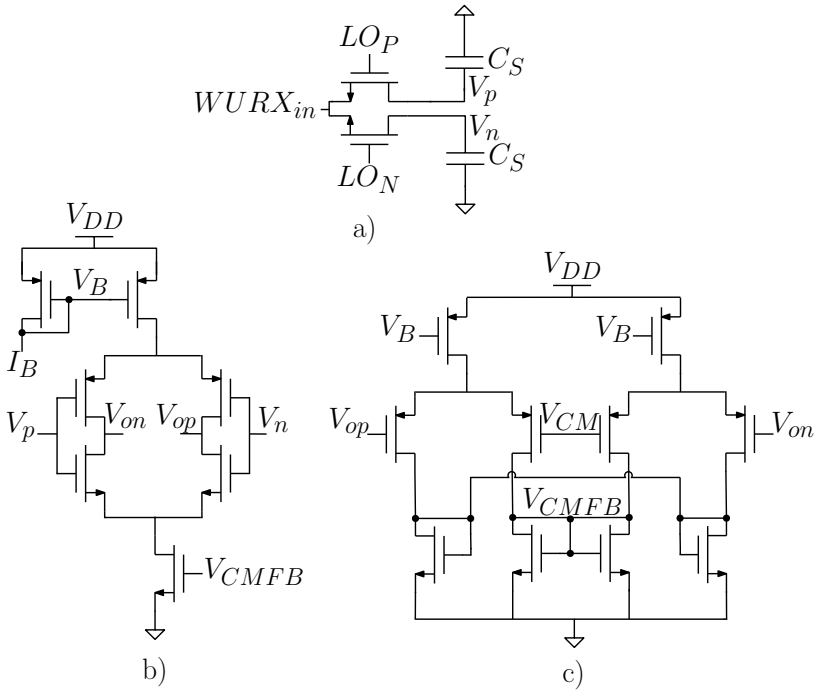

Figure A.7: Building blocks of the WuRX; a) Single-balanced passive mixer, b) Inverter based baseband amplifier, c) Its CMFB.

size of $10\mu m/0.3\mu m$ and 32 fingers is used as a unit switch in $SCC_{1/3}$. In $SCC_{2/3}$ and the output multiplexer, a parallel connection of four of these unit switches is used. This improves the driving efficiency of the TX as a lower SCC output resistance is assigned to a higher DC voltage level. The value of the flying capacitors is chosen as $1\mu F$, which leads to a simulated corner frequency between Fast and Slow Switching limits [91] of 10kHz. The simulated total output resistance is 20Ω and 10Ω for $SCC_{1/3}$ and $SCC_{2/3}$ in the Fast Switching Limit, respectively.

A.4.2 WuRX Circuit Design

Fig. A.7 shows the transistor-level implementation of the WURX. The SBPM (Fig. A.7a) comprises two NMOS transistors and sampling capacitors, C_S. The size of the transistors ($400nm/60nm$) is chosen to reduce the dynamic power. A C_S of $8.5pF$ is used to lower the noise contribution of the mixer. Considering the large capacitance of the PZT transducers, the loading introduced by these capacitors is negligible. Fig. A.7b and A.7c show the implementation of the inverter-based baseband amplifier and its common-mode feedback (CMFB) [47], respectively. An inverter-based topology is chosen to increase the power efficiency while all transistors are biased in the weak-inversion region with a g_m/I_D ratio of 31 V^{-1}. With a supply voltage, V_{DD}, of $0.6V$, a bias current, I_B, of $0.35nA$, and an LO of 38kHz, the post-layout simulations of the front-end predict a total conversion gain of 34dB, a 1.2kHz 3-dB BW and an

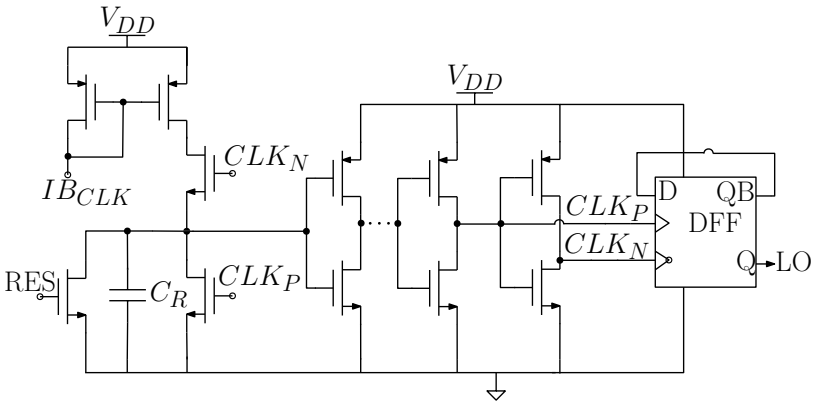

Figure A.8: Schematic of the on-chip clock generator in WURX (OSC).

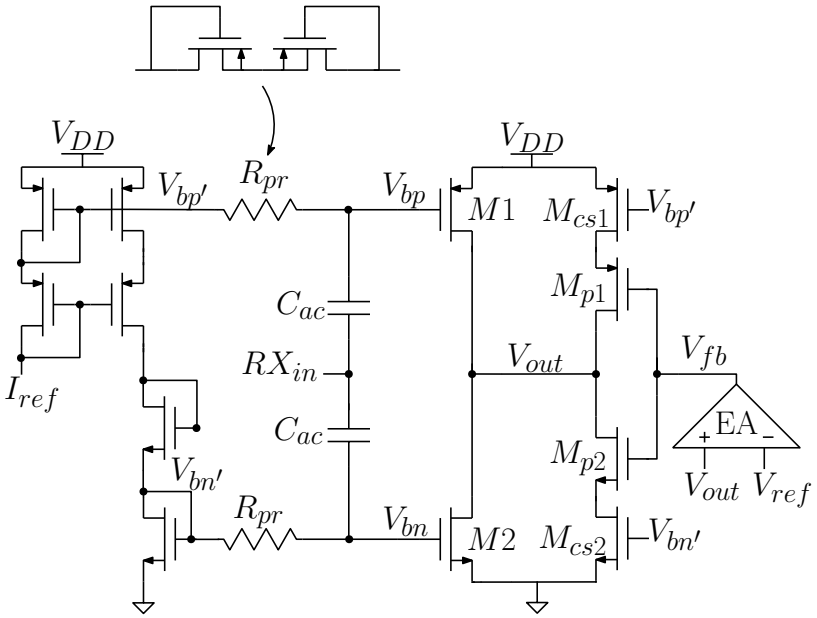

Figure A.9: Schematic of the LNA in MAINRX [30].

IRND of 365nV/$\sqrt{Hz}$. Thus, the IRN is calculated as 13μV_{rms}, which satisfies the specs in Table A.1. The digital output of the WURX will be followed by a digital thresholding, to decide whether or not to wake-up the node. Although the sensitivity of the front-end can be degraded due to the variations of the LO over PVT, the digital thresholding will not be influenced, and the nodes can successfully wake-up, as long as the SNR at the input of the front-end is sufficient. Thereby, the accuracy requirement of the LO frequency can be relaxed to save power. This allows using a simple on-chip clock generator, as shown Fig. A.8. Here, an external reference current, IB_{CLK}, is integrated on the capacitor, C_R, to generate a ramp voltage. Then, a feedback loop comprising 6 stages of inverters resets the voltage on C_R when the threshold of the first inverter is reached. An external reset signal, RES, is used

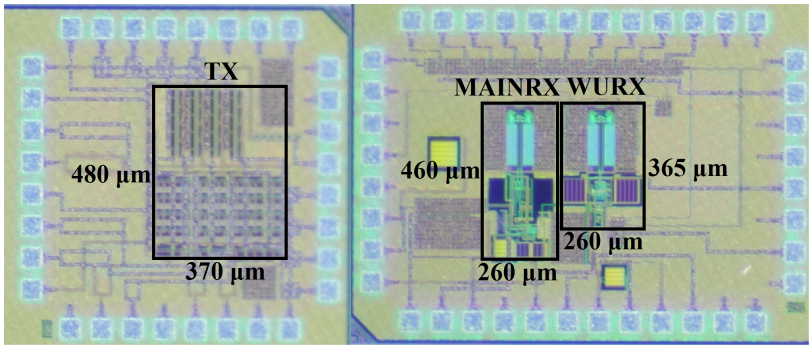

Figure A.10: Die photo of the transmitter TX and receivers: MAINRX and WURX.

only at start-up. High-threshold transistors are used in the inverter chain to limit the power consumption, while 6 stages of inverters are used to provide enough on-time for the generated pulse signal. To obtain a 50% duty-cyle LO, the inverter chain is followed by a Master/Slave D-type flip-flop, which is implemented with two pass gate latches. The Q output of the DFF is used as an input to the non-overlapping clock generator circuit [102], which provides the signals, LO_P and LO_N, used by the SBPM for down-conversion. The ADC clock is generated dividing by two the LO.

A.4.3 MAINRX Circuit Design

The MAINRX uses a single-ended inverter-based LNA to save power. A DC feedback is needed to stabilize its output DC voltage. As shown in Fig. A.9, a current starved auxiliary inverter, formed by M_{p1} and M_{p2}, is used in parallel to the main inverter (M_1 and M_2) to stabilize the DC level of the output node, V_{out}. The gate of the auxiliary inverter is controlled via feedback by comparing V_{out} to a reference voltage, V_{ref}, and feeding back the error signal, V_{fb}, amplified by the error amplifier, EA [30]. The auxiliary inverter can either source or sink a suitable current to the output node, thus keeping the output DC voltage at the desired value. The proposed DC feedback can compensate the errors due to leakage of pseudo-resistors, R_{pr}, and mismatch between the biasing network and the LNA. The transconductance of the auxiliary inverter is much lower than the main inverter. This provides a small DC current, low power, and high output resistance, minimizing the impact of the auxiliary inverter on the LNA gain. Compared to previous works [60, 81, 87], the proposed DC feedback allows the single-ended inverter to work in continuous-time. Besides, it applies the feedback to the output node instead of the LNA input, preventing any degradation of the SNR. The SBPM uses similar size transistors as in the WURX, however, the sampling capacitors are not used to avoid loading the LNA. Due to the presence of the LNA in the MAINRX, the resulting kT/C noise of the mixer is negligible when referred to the input. The BBAMP uses a two-stage architecture with Miller compensation. The feedback capacitors have a ratio of $(134fF/35fF)$ to obtain a gain of about 12dB. The complete front-end is simulated to have a conversion gain of 43dB, a 3-dB BW of

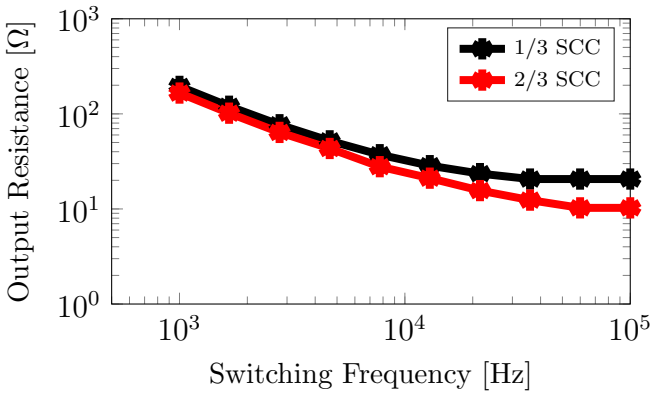

Figure A.11: Measured output resistance of the switched capacitor converters (SCC) with respect to the switching frequency.

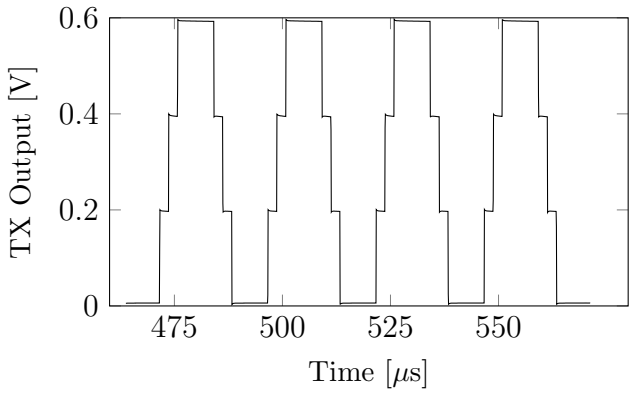

Figure A.12: Measured four-level output voltage of the TX with a 400Ω load.

20kHz, and an IRN of 7.8μV_{rms} while using a single 0.6V supply. The MAINRX can be overdesigned in terms of IRN and 3-dB BW compared to the specs in Table A.1, as the MAINRX is normally off, and a larger bandwidth can be useful to improve ranging resolution in means characterized by higher speed of sound.

A.5 Measurement Results

A 65nm CMOS process is used for fabrication and the die photos of the circuits are shown in Fig. A.10. A detailed measurement of the individual circuits and the proposed ranging system will be presented in the following sections.

A.5.1 TX Characterization

To characterize the output resistance of the TX, the output voltage of each SCC is measured with an external 400Ω resistor load (equal to the impedance of PZT1 at

Table A.2: TX Characterization Summary

	PZT1	PZT2	10nF
Driving Frequency [kHz]	39	94 - 107	39
SCC Switching Frequency [kHz]	10	10	3
VDD_{driver} [V]	1.2	1.2	1.2
IDC_{driver} [μA]	3.2	3.2	1.07
VDD_{TX} [V]	0.6	0.6	0.6
$IDC_{4-level}$ [μA]	231.7	131.1	79.8
$IDC_{2-level}$ [μA]	311.1	210.4	230.1
Improvement: $\frac{IDC_2-IDC_4}{IDC_2}$	25.5%	37.7%	65.3%

resonance) while varying the switching frequency. The outcome is depicted in Fig. A.11, where the two asymptotes of Slow Switching Limit (SSL) and Fast Switching Limit (FSL) [91] can be appreciated. The transient output voltage of the TX is shown in Fig. A.12, where a 4-level output driving signal with a frequency of 40kHz is shown while switching the SCCs at 10kHz. The performance summary of the TX when PZT1, PZT2, and a 10nF capacitor are used as a load is reported in Table A.2. In these measurements, $VDD_{TX} = 0.6$V, while the gate drivers are supplied by $VDD_{driver} = 1.2$V, PZT1 is driven at its resonance frequency of 39kHz, the capacitor is driven at the same frequency, while PZT2 is driven with Chirp2t. The average currents, IDC and IDC_{driver}, drawn from the supply voltages, VDD_{TX}, and VDD_{driver}, respectively, are measured. A load of 10nF is used as a reference to validate the energy-saving in the case that the load is purely capacitive. As summarized in Table A.2, a reduction of 65.3% in IDC is measured when a 4-level driving signal is applied to the 10nF load compared to the two-level case. This measurement is in good agreement with the fact that a step-wise charging of a capacitor in three equal steps reduces the energy spent to charge the capacitor to one third of the one needed when charging the capacitor directly to the final voltage level [89]. Concerning the experiments with PZT1, this transducer is driven at its resonance and an identical PZT1 is placed at 5cm apart to monitor the received signal. In this experiment, a reduction of 25.5% in IDC when using four levels instead of two is observed, while there is only a 1.4% loss in the received signal power, compared to the two-level case. This is due to the fact that four-level driving at the same driving frequency as the two-level one contains less energy in the harmonics, while having a similar energy at the fundamental tone. Moreover, a relatively larger reduction of 37.7% in IDC is measured when driving PZT2 with Chirp2t and using four levels instead of two. As the driving frequency is swept in a BW of 13kHz, the impedance of PZT2 is in average more capacitive compared to that experienced in the measurement of PZT1, and thus a larger energy-saving is measured than the one experienced in the measurement of PZT1 at resonance. The electrical efficiency of the TX is defined as the ratio between the electric power delivered to the transducer and the total power consumed by the TX. The measured TX efficiency when driving PZT1 with a four-level driving signal at its resonance frequency of 39kHz is 88%. In resonance, part of the power losses

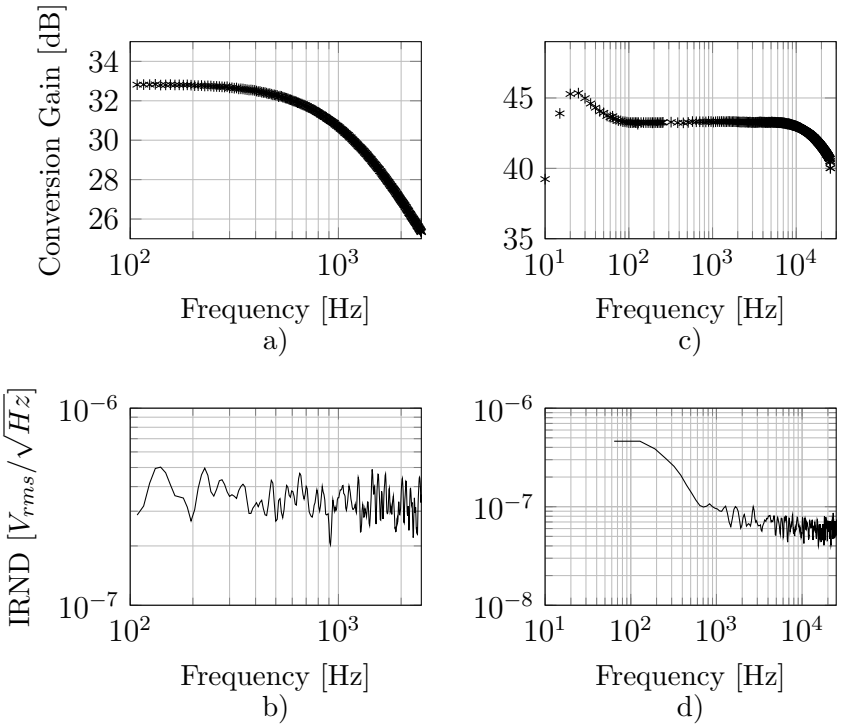

Figure A.13: a) Measured conversion gain of the WURX for an LO=39kHz. The maximum gain is 32.8dB @200Hz and the 3-dB BW is 1.2kHz. b) Corresponding IRND of the WURX. IRND = $400nV_{rms}/\sqrt{Hz}$@1.2kHz is measured. c) Measured conversion gain of the MAINRX for an LO=100kHz. The gain is 43.3dB @5kHz and the 3-dB BW is from 10Hz to 25kHz. d) Corresponding IRND of the MAINRX. IRND = $60nV_{rms}/\sqrt{Hz}$@5kHz is measured.

come from the resistance of the switches and part of the losses come from switching on and off the switches. Out of resonance, the efficiency will decrease, as the load becomes capacitive. Indeed the measured transmitter efficiency when driving PZT2 with a two-level Chirp signal (94kHz - 107kHz) is 47%, and the efficiency increases to 62%, when a four-level Chirp signal is used.

A.5.2 WURX and Wake-up Link Characterization

A.5.2.1 Electrical Measurements

The measured conversion gain and IRND of the WURX for an LO=39kHz are shown in Fig. A.13a and b, respectively. The total integrated noise in the 3-dB BW of 1.2kHz is found to be $14\mu V_{rms}$. For these measurements, external reference currents, I_B of 0.35nA and IB_{CLK} of 0.45nA, are used. The sensitivity level of the WURX is estimated first with electrical BER measurements, where an OOK modulated signal with different attenuated amplitudes is provided by an arbitrary signal generator

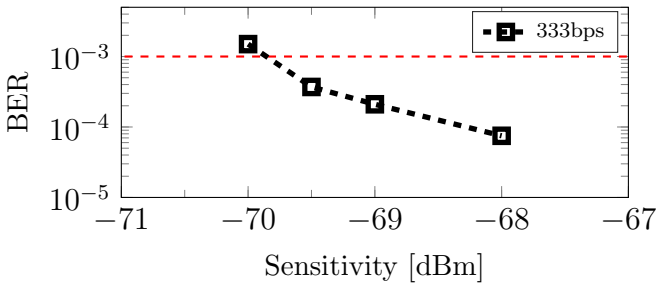

Figure A.14: Measured BER of the WURX

to the WURX, and the ADC codes at the output are read-out and transferred to MATLAB for demodulation. Fig. A.14 shows BER plots for this setup, where a -69.5dBm ($74.9\mu V_{rms}$) input signal at 333bps data-rate is demodulated with a 10^{-3} BER. This sensitivity level is validated with an experimental setup built with two PZT1 transducers, a TX, and a WURX to transmit OOK signals using a 39kHz carrier. An input signal of $-69.5dBm$ is received when the transducers are 75cm apart and a successful communication link with a 10^{-3} BER is established in air. In this measurement, the on-chip oscillator is used to provide a 38kHz LO. The resulting 1kHz baseband signal is sampled with a 19kHz (LO/2) ADC sampling clock. Although lowering the sampling frequency will reduce the ADC power consumption, a 19kHz sampling clock is used to have sufficient margin to sample the baseband signal considering the temperature sensitivity of the LO, as will be discussed in the following section.

A.5.2.2 Missed Detection Rate (MDR) Measurements

In order to reduce the demodulation complexity in the digital domain and to save power, the WURX digital output is used in a digital threshold detector, where a threshold around the DC output code of the ADC is applied to wake-up the node. The measurement shown in Fig. A.15 is performed when NODE1 and NODE2 are 75cm apart, and NODE2 activates its TX to broadcast the $WURX_{code}$ of a symbol one, '1'. Since the initial phase of two separate nodes is unknown, two different thresholds have been chosen; an upper one (535) and a lower one (525) to detect the level of the incoming signal. The ratio between the threshold levels and the rms of the noise voltage at the output of the WURX determines the probability of a false alarm. To have a false alarm rate of one per 15min (the average time interval between the crossings of the threshold due to noise), the threshold levels are chosen as ≈4 times the rms value of the measured noise voltage ($\sim 0.8LSB$) at the output of the WURX [53]. To characterize the performance of the WURX link, missed-detection rate (MDR) measurements have been performed, too. In these measurements, the data rate is set to 100bps, where the symbol '1', as shown in Fig. A.15, is transmitted in a 10ms ($= T_{sweep}$) period, according to the proposed system. Lowering the data rate compared to our measurements in Fig. A.14 relaxes the SNR needed to correctly receive a '1', and enables increasing the achievable distance for 10^{-3} MDR between

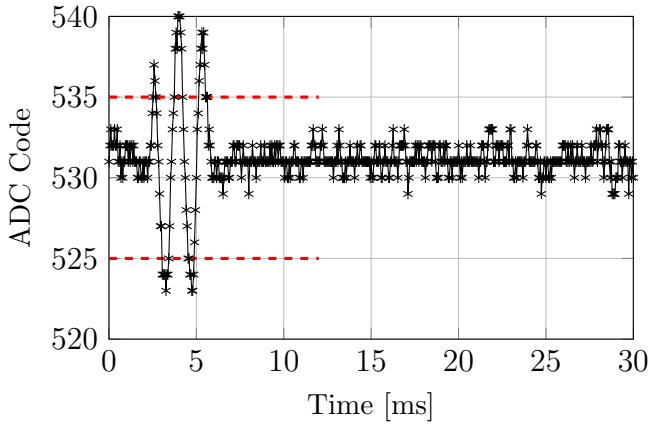

Figure A.15: A Measurement of WURX ADC code when TX transmits a single one (encoded as 2.5 periods of sinusoid) as $WURX_{CODE}$.

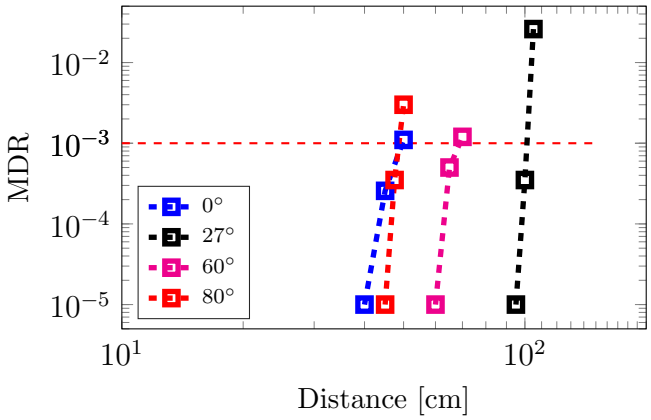

Figure A.16: MDR characterization of WURX.

the nodes to 1m in air, satisfying the specs in Table A.1. To further investigate the WURX link performance under temperature variation, the WURX is placed in a temperature chamber and the operating temperature of the WURX is swept from 0°C to 80°C. During these characterizations, the external bias currents (IB_{CLK} and I_B) provided to the WURX are also varied with the temperature according to the data reported for the reference current generator in [103]. The results of these experiments are summarized in Fig. A.16, where at room temperature of 27°C, the wake-up link has been established until 1m in air with an MDR lower than 10^{-3}. When the operating temperature increases, the clock frequency of the on-chip oscillator increases as well. This results in that the baseband signal after down-conversion falls outside the 3-dB bandwidth of the WURX, worsening the sensitivity of the front-end. When the temperature is reduced to 0°C, the LO frequency and the bandwidth of the amplifier decrease together, thus the baseband signal is attenuated even more and further degrades the sensitivity. As shown in Fig. A.16, at the limit temperatures of 0°C and 80°C, the distance that the WURX link can achieve with an MDR better than

10^{-3} is reduced to 45cm. For these temperatures, the power supply can be increased by 10% while keeping an MDR better than 10^{-3}. It is important to mention that in [103] about +-30% change of the absolute value of the reference current due to process variations is reported. In the WURX link, it is desired to keep the baseband signal, obtained after down converting the carrier (39kHz) of the $WURX_{code}$ with the LO, inside the 3-dB BW of the amplifier (1.2kHz), to maintain the sensitivity of the front-end. This means that a calibration of the LO with at least 5bit resolution is needed to keep the LO error e.g. within 2% from its 39kHz target. Such calibration, which can be implemented with a simple current DAC fed by the current reference, is not yet implemented in the present chip.
At room temperature, a total power consumption of 23.1nW for the WURX under a single supply of 0.6V is measured. This figure includes the power of on-chip buffers used to distribute the LO (38kHz) and the ADC sampling clock (LO/2). The comparison of the ADC code with the thresholds is done in the FPGA by using simple digital comparators, where the output of the on-chip clock generator is used as a clock. The power overhead of this comparison is simulated at a transistor level as 0.5nW, and added to the power consumption of the WURX. As a result, a 23.6nW power consumption is obtained. Although the power required to generate the reference currents is excluded from this figure, this overhead is estimated to be much lower ($<120pW$) than the reported WURX power, when using relevant prior-art implementations in similar technology and supply voltage [103].
A distance of 45cm in air at the worst-case operating conditions is sufficient in the foreseen applications, indeed, considering that the attenuation of US in water is more than 100 times lower than that of in air [98], a much larger operating distance can be obtained if the nodes are operated in a fluidic environment. In water, the limiting factor for the distance measurement will be the sweep time of the Chirps, which must be longer than the round-trip time of flight between nodes. Considering that the speed of US in water is around 1500m/s, the max. achievable distance in fluids with a T_{sweep} of 10ms is calculated to be 7.5m. If a larger distance in fluids is needed, a longer sweep time can be used at the cost of an increased energy consumption during the ranging.

A.5.3 MAINRX and Ranging Link Characterization

A.5.3.1 Electrical Measurements

The measured conversion gain and IRND of the MAINRX for an LO=100kHz are shown in Fig. A.13c and d, respectively, where an IRN of $\sim 12.2\mu V_{rms}$ is found in its 3-dB BW from 10Hz to 25kHz. For these measurements, an external reference current, I_{ref}, of 1nA and a sampling clock of 50kHz for the ADC are used. The small low-frequency peaking in the response is due to the mismatch between the pseudo resistors in the feedback network of the BBAMP, and can be reproduced in post-layout simulations. Under these conditions, a total power consumption of 0.56μW when using a single supply of 0.6V is measured, including the power of on-chip buffers

needed to distribute all clocks, and excluding the overhead for generating the on-chip reference current.

A.5.3.2 One-way FMCW Ranging Measurements

A separate setup to characterize the FMCW ranging link is built in air at room temperature. The TX sends a Chirp via a PZT2, which is received by an identical PZT2, passed to the MAINRX and there mixed with an identical Chirp. The moment at which both Chirp signals begin is synchronized by a common start signal. The ADC data of the MAINRX are recorded during one sweep time, T_{sweep} of 10ms. Afterward, the FFT of the recorded data is calculated in MATLAB. The FFT resolution of the derived spectrum is equal to the inverse of the recorded time (T_{sweep}), which corresponds to 100Hz ($\frac{1}{10ms}$). The characterization of this FMCW ranging link up to 180cm in air is shown in Fig. A.17a and the absolute error between the calculated distance and the reference distance is depicted in Fig. A.17b. The mean of the error in ranging is calculated as 0.18mm with a standard deviation of 8.4mm. Modifying the equation to determine the distance R between nodes (Fig. A.2) for a one-way trip of the US waves, a minimum measurable distance $d_{min} = \frac{f_{beat} \cdot c_{US} \cdot T_{sweep}}{BW} = 26mm$ is obtained from the minimum FFT resolution of 100Hz. Thus, as shown in Fig.

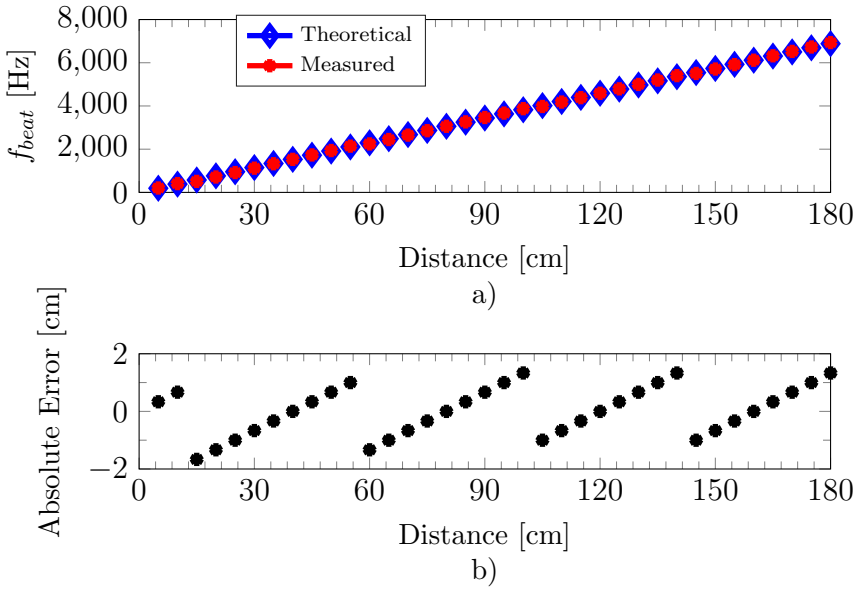

Figure A.17: a) FMCW ranging link characterization. b) Absolute error in the distance calculation.

A.17b, the absolute error of this measurement will follow the trend of a quantization error of amplitude d_{min}, to which would correspond a theoretical standard deviation of $\sigma_{FFT1} = \frac{d_{min}}{\sqrt{12}} = 7.5mm$. The FFT quantization is thus the main limiting factor to the ranging resolution in this experiment. To keep the post-processing as simple as possible, f_{beat} (Fig. A.2) is simply chosen as the frequency with the highest power

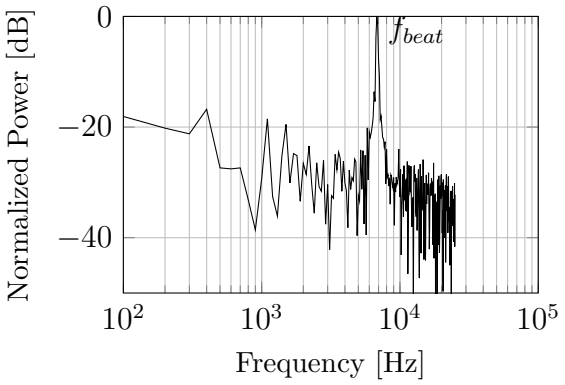

Figure A.18: A spectrum of the recorded ADC data at 1.8m distance.

signal in the measured spectrum, as shown in Fig. A.18. According to this characterization, the achievable distance in the FMCW ranging link can be up to 1.8m, where the f_{beat} is successfully measured with at least 10dB margin above the max. measured noise level.

A.5.4 Rangefinder System Characterization

A proof-of-concept characterization of the full proposed system, including the wake-up and ranging links is demonstrated here. The setup is the one shown in Fig. A.1b, and described in Section A.2.1. Similarly to the one-way FMCW ranging measurements, a 50kHz sampling clock for the ADC is used and the ADC data of the MAINRX is recorded during a 10ms of sweep time. The experiment is performed in air at room temperature without external synchronization. The LO of 38kHz from the on-chip clock generator is used in the WURX. To quantify the overall ranging error, NODE1 and NODE2 are placed at 0.55m apart and the distance measurement of the full rangefinder system is repeated 10000 times. Fig. A.19 shows the histogram of the absolute error, which is fitted to a normal distribution with a mean (μ_{WU}) of 6.6mm and a standard deviation (σ_{WU}) of 18.7mm. In this experiment, the jitter of the LO in the WURX link and the WURX ADC sampling result in an uncertainty of the wake-up time of the node, which reflects in an error in the distance measurement and in the observed standard deviation. In Fig. A.20a, the rangefinder system measurements of the f_{beat} up to 1m are shown, where at each point an average of N=15 measurements is reported. The averaging results in a decrease of the standard deviation due to random sources of uncertainty in the WURX. The deterministic error caused by the FFT resolution for the two-way ranging can be estimated using the R equation in Fig. A.2, to obtain a minimum measurable distance $R_{min} = 13mm$. Changing the measurement distance will thus cause a uniformly distributed ranging error with a standard deviation $\sigma_{FFT2} = \frac{R_{min}}{\sqrt{(12)}} = 3.7mm$. Combining the two uncorrelated error sources, one would predict for the full system measurements a standard deviation σ_{tot}, which can be estimated as $\sigma_{tot} = \sqrt{\frac{\sigma_{WU}^2}{N} + \sigma_{FFT2}^2} = 6.1$mm. The measured error in

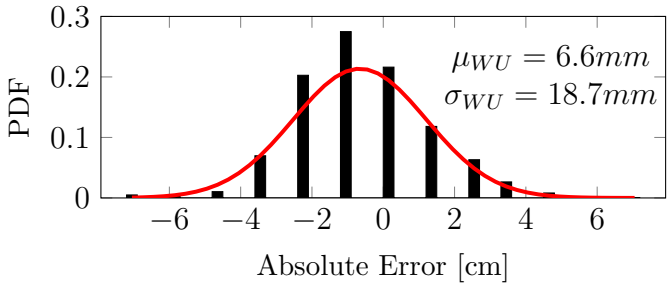

Figure A.19: A normalized histogram of the 10000 measurements at 0.55m.

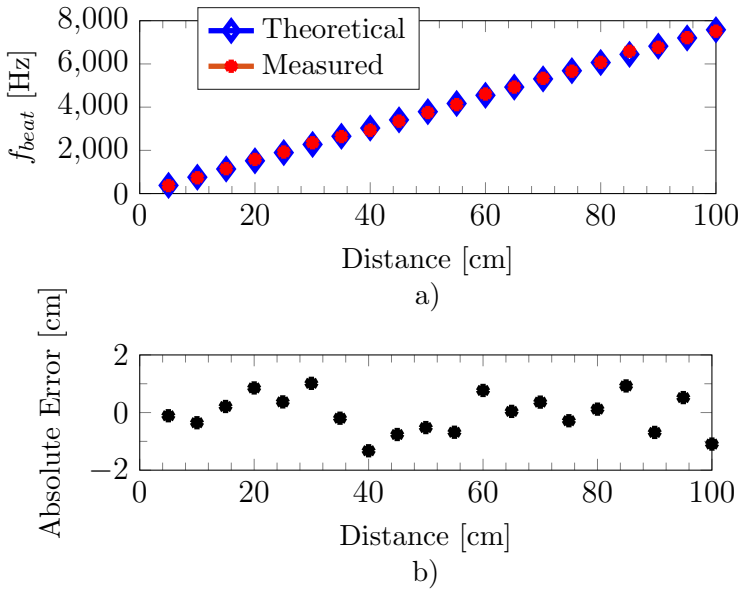

Figure A.20: a) Full-system ranging link characterization. b) Absolute error of the rangefinder system. Each point is an average of 15 independent measurements.

Fig. A.20b has a mean of 0.5mm and a standard deviation of 7mm, which is close to the expected value. It can be observed that the addition of the wake-up uncertainty randomizes the shape of the error in Fig. A.20b compared to the sawtooth behavior observed in Fig. A.17b.

A.6 Benchmark

The performance of the proposed US WURX and its comparison with recent prior-art is summarized in Table A.3, where a Figure-of-Merit for wake-up receivers proposed in [105] as $FoM_{WuRx} = Energy(J)/bit \cdot P_{sensitivity}(W)$ is used for benchmarking. The works in [45, 50, 92] achieve a sensitivity level of around $-81dBm$, while consuming more than $1\mu W$. In [48], the lowest power consumption of $8nW$ is reported with an envelope-detector (ED) first topology, where a lower sensitivity of -59.7dBm is

Table A.3: Performance Comparison of the Proposed US WuRX

	[45]	[50]	[48]	[92]	**This Work**
Technology [nm]	65	250	65	65	65
Carrier Frequency [kHz]	40	41	57	40	39
Supply Voltage [V]	0.6	0.3	0.5	0.8	0.6
Modulation	OOK	OOK	OOK	OOK	OOK
Data Rate [bps]	250	250	336	1000	333
Receiver Power [μW]	4.4	1	0.008	1.18	0.0236
Sensitivity [dBm]	-81	-81	-59.7	-81.6	-69.5
FOM_{WuRx} [$(J/b) \cdot W \cdot 10^{-20}$]	14	3.18	2.55	0.82	0.79

Table A.4: Performance Comparison of the Proposed US Rangefinder

	[57]	[104]	[30]		This Work	
Method	ToF	Phase-shift	FMCW		FMCW	
Target Reflector	Passive	Passive	Active		Active	
Medium	Air	Air	Air		Air	
Transducers	PMUT	Membrane	PZT		PZT	
Technology [nm]	180	800	65		65	
Min/Max Range [mm/m]	45/1	18/0.11	50/1		50/1	
Range Error [mm]	0.41 @0.5m	2.5@0.1m	6.5@0.55m		18.7@0.55m	
Field of view	3D	1D	1D		1D	
TX Supply [V]	32	5	0.6 + 1.2		0.6 + 1.2	
			FMCW	FMCW	Wake-Up	FMCW
Frequency [kHz]	220	100	98-106	194-202	39	94-107
TX Energy Consumption [μJ]	1.05	2800	1.07	1.59	0.43	0.82
RX Supply [V]	1.8	5	0.6	0.6	0.6	0.6
RX Energy Consumption [nJ]	1600	$3.7 \cdot 10^6$	4.48	4.48	0.236	5.6
Always-on Power Consumption [nW]	N/A	N/A	560		23.6	
Total Energy per Measurement [μJ]	2.65[a]	6500	2.67		1.25	

a: Energy consumption is scaled per channel excluding the power overhead of the digital circuits.

obtained. In this work, by using a mixer-first front-end, the low-conversion gain of the ED is avoided and the sensitivity of the WURX is improved. One should notice that the FoM_{WuRx} reported in [92] does not include, similarly to the present work, the negligible power overhead of the bias current generation. With a total of 23.6nW power consumption, our work achieves a FOM_{WuRx} of 0.79 $(J/b) \cdot W \cdot 10^{-20}$, which in line with the best prior-art.

The performance of the proposed US rangefinder and its comparison with prior-art is summarized in Table A.4. The works in [57, 104] are based on the processing of the echoes coming from passive reflectors in air. On the other hand, the rangefinder in [30] and this work enable US distance measurement between active sensor nodes. This work and [30] exploit a frequency division duplexing between their transmitters and receivers, thereby, the interference from passive reflectors is avoided, as demanded

in our application. Compared to [30], this work uses a multi-level driver to improve the driving efficiency of the US transducers, which allows lowering the TX power consumption. In addition, this work uses identical Chirps residing in the same frequency band, which are digitally synthesized separately on the initiator and wake-up node without any analog or digital modification, thus simplifies the hardware needed in the nodes. Another profound difference of this work compared to [30, 104] and [57] is the use of a mixer-first WURX combined with FMCW ranging to lower the always-on power consumption of the nodes down to 23.6nW. Although this work has a lower ranging resolution of 18.7mm, which is tolerable in our applications, the proposed rangefinder system dissipates $1.25\mu J$ per measurement, an improvement of at least 2x compared to prior art US rangefinders. This figure includes the power of the on-chip buffers used to distribute and drive the Chirp signals and the sampling clock of the ADC, while it excludes the power needed for generation of the on-chip current references and the clocks to synthesize the Chirp signals, the losses due to the generation of the 0.6V and 1.2V supplies from a battery, the memory leakage and the energy needed to write (read) the data to (from) an on-chip memory.. An additional highlight of this work is that the response of the nodes in wake-up mode will be transmitted only when they receive a signal in a separate frequency band, thus their operation is independent of each other. This means that a global synchronization is not needed in the swarm of sensor nodes. Furthermore, the signal processing (e.g. FFT) needed to derive the spectrum of the received data and calculating the distances can be performed outside the environment under test, after the nodes are recuperated at the end of the exploration. As a result, the power overhead for digital processing can be minimized in the actual application. The memory needed to store one measurement is $10ms \cdot 50kS/ \cdot 10b = 5$kb. The on-chip memory needed to store these data is not implemented yet. A recent work in [76] demonstrates a 1Mb flash memory which features a sleep mode power that is lower than the power consumption of the WURX. Based on the parameters provided by this work, the energy that would be spent to write and read the data needed per distance measurement, including the memory used to synthesize the Chirp, is only 20% of the total energy consumption per measurement. Furthermore, using ultra low-power approaches such as in [77], the memory leakage can be reduced even more, making it completely negligible when compared to the always-on node power achieved in this work.

A.7 Conclusion

This work presents the circuit and system design for an ultrasonic rangefinder system, where the sensor nodes can be operated in air or a fluidic environment. The nodes in a swarm perform measurements to find their relative distance while using separate frequency bands for the wake-up and FMCW ranging links. This makes the distance measurement insensitive to the echoes generated by the boundary of the environment being explored. The experimental characterization of the building blocks of the proposed system has been presented. The measurement results show

that the proposed approach enables an always-on power consumption of only 23.6nW per node and makes possible ultrasonic distance measurements with the lowest energy per measurement reported to date.

Acknowledgment

This work has been funded by the European Union′s Horizon 2020 research and innovation programme under grant agreement No 665347.

Appendix B

A $2.67\mu J$ per Measurement FMCW Ultrasound Rangefinder System for the Exploration of Enclosed Environments

Gönenç Berkol, Peter G. M. Baltus, Pieter J. A. Harpe, and Eugenio Cantatore

Published in Solid State Circuits Letters (SSCL). IEEE, 2020

This paper presents the design and experimental characterization of an ultrasound rangefinder system. A new distance measurement method is proposed for determining the relative position among sensor nodes that are operated in a collision and multipath rich environment, while needing no common time reference between them. A 65nm CMOS technology has been used to build the sensor nodes, which comprise an on-chip receiver and transmitter. The proposed rangefinder system is characterized up to 1m in air and has a range resolution of 6.5mm, while dissipating $2.67\mu J$ *per measurement.*

Ultrasound rangefinder, Ultrasound front-end, Ultrasound receiver, Analog IC, Swarm of sensor nodes

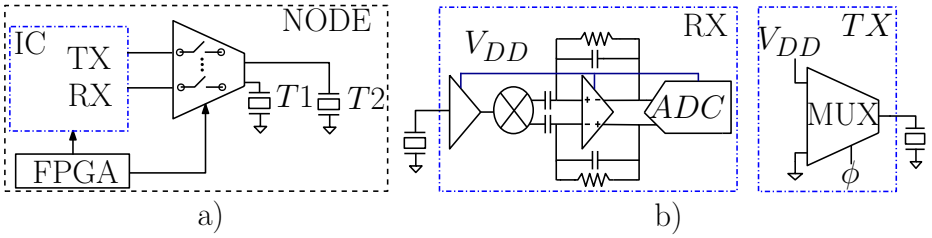

Figure B.1: a) Building blocks of a sensor node b) Top-level implementation of the corresponding blocks.

B.1 Introduction

Exploration of environments that are inaccessible and miss GPS coverage is an emerging application, where the information on the geometry of enclosed volumes such as underground reservoirs, or water and oil pipelines is desired. Swarms of sensor nodes can be used for this exploration. The nodes are injected into the volume to explore, where they perform distance measurements while traversing the unknown environment with the flow of the medium [10]. Afterwards, the nodes are recuperated and the data in their memories are analyzed, to build a map of the environment visited based on the distances measured between the nodes during the exploration [14]. Ultrasound (US) has been used as a way to exchange data in fluidic environments due to its favourable propagation characteristic in liquids compared to RF. Typical approaches to US distance measurement are based on the Time-of-Flight (ToF) of the reflected echoes. In the described application, however, it is desired to measure the distances between nodes, while echoes from passive reflectors in the environment should be neglected. This problem is addressed in this paper by devising a novel rangefinder system based on an US Frequency Modulated Continuous Wave (FMCW) method to determine the distance between nodes in a swarm. Moreover, the measurement method described does not require global clock synchronization within the swarm. The paper is organized as follows: Section II explains the details of the proposed rangefinder system. In Sections III and IV, the system and circuit design are discussed. The measurement results are presented in Section V. The performance of the US transceiver is benchmarked against prior art and conclusions are given in Section VI.

B.2 Proposed Rangefinder System

Each sensor node has an on-chip RX and TX for receiving and broadcasting US data, as shown in Fig. B.1a. An FPGA is used here as a digital backend, which initiates the ranging operation and controls the operating mode of the sensors. The nodes use two off-chip transducers, T1 and T2, which can be connected to either the TX or RX using an off-chip switching matrix. The nodes enable two different modes of

operation. The default mode is called the active tag mode. The nodes operating as an active tag listen to the incoming signals via the transducer T1, and actively transmit back a modified version of the incoming signal by using the transducer T2. The second operating mode is called the ranger mode, where a node aims to find the distance of the surrounding active tags. The digital backend of a sensor node activates the ranger mode periodically, to initiate the distance measurement protocol. The initiation does not need a global synchronization among nodes in the system and can be activated anytime based on an algorithm inside the digital backend. The distance measurement is performed by means of a two-way ranging using frequency modulated US signals. The conventional FMCW ranging method is shown in Fig. B.2a. A Chirp, a signal with a linearly changing frequency in time, is transmitted, and its reflected echo is received after a time τ_d. The spectrum of the signal obtained mixing the sent and received Chirps will show a frequency peak, f_{beat}, corresponding to the round trip time, τ_d, of the echo Chirp. As we would like to find the distance to the active tags and avoid the echoes from the boundary of the environment, a modified version of the conventional method is proposed, as shown in Fig. B.2b. Its principle can be explained as follows: The ranger node generates two Chirp signals, Chirp1r and Chirp2r. Chirp1r fits the bandwidth of T1, and Chirp2r fits the bandwidth of T2, which do not overlap. Chirp1r is broadcasted via T1, and reaches the other nodes that are operating as active tags. These nodes down-modulate the Chirp1r to baseband and up-modulate it again to a frequency band fitting T2, named as the Chirp2t. This signal is sent back using T2 and reaches the ranger node, where it is multiplied by the original Chirp2r. The resulting spectrum, similar to the conventional method, will have a frequency beat corresponding to the round trip delay between the nodes. As a result, with knowledge of the bandwidth (BW) and the duration (T_{sweep}) of the Chirps, as well as the speed of US in the medium, the distance to the active tags is calculated (Fig. B.2). Thanks to the different frequencies of the signal sent by the ranger and the signal sent back by the active tag, the ranger node can distinguish echoes coming from passive reflectors from signals sent back by active tags. In case multiple active tags are present at different distances, different frequency peaks corresponding to the active tags will be obtained [67]. By adding a different identification payload to the Chirp in each active tag, the ranger can also distinguish between the first signal received by a tag and possible later signals coming from the same tag due to multipath.

B.3 System Design

The intended operating medium for the rangefinder system is fluidic, where US propagate with much lower attenuation (<100x) compared to air. However, to simplify measurements and keep the maximum distance between the sensor nodes at a manageable level, we built the proof-of-concept characterization setup of the proposed system in air. Accordingly, considering that the duration of the Chirp has to be larger than the round-trip ($\approx 6msec$) among the sensors at the desired maximum

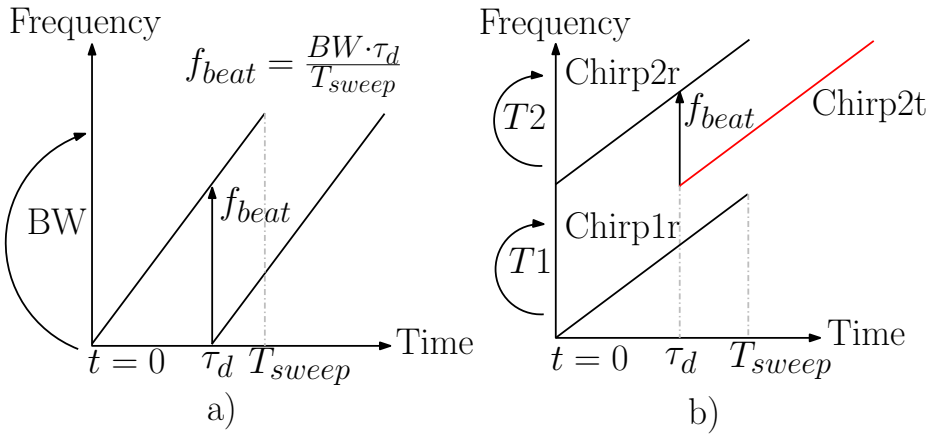

Figure B.2: a) Conventional FMCW Method. b) Proposed Method

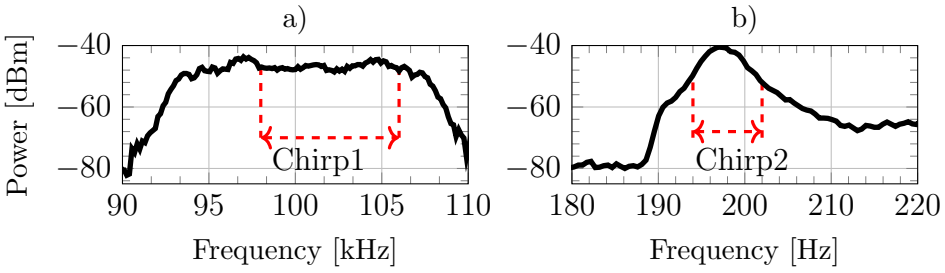

Figure B.3: Link characterization of a) T1 and b) T2. Each measurement is performed at 10cm distance.

distance, which is chosen as 1m in air, T_{sweep} is determined as 8msec. With this choice, a max. distance of 6m can be achieved in water. If c_{US} is the speed of sound in air and BW is the bandwidth of the Chirp signals, the smallest distance step that can be measured using FMCW is $\frac{c_{US}}{2BW}$. To keep it about 20mm, a Chirp BW of 8kHz is needed in air. T1 and T2 are commercially available piezo-electric transducers [20] chosen to broadcast and receive the above mentioned Chirps. T1 and T2 have a size of 40x40x17mm and 19x19x11mm, a parasitic capacitance of 0.88nF and 1.1nF, and a nominal resonance of 100kHz and 200kHz, respectively. The link among the transducers are characterized by exciting them with a $0.6V_{pp}$ square-wave signal and recording the electrical power received with identical transducer, as shown in Fig. B.3. Due to the narrow-band characteristic of T2, the frequency range between 194kHz to 202kHz corresponding to its 10dB BW has been assigned for Chirp2, while Chirp1 occupies the range between 98kHz to 106kHz residing inside the 6dB BW of T1. The link-budget analysis has been performed by investigating the power-loss of the transducers in air at room temperature, where T1 and T2 are driven with a $0.6V_{pp}$ burst signal at their resonance. The received power is modeled with the formula: $P_{rec} = -k \cdot 10log(d) + P_0$, where d is the distance in cm, k is the path loss coefficient and P_0 is the initial power loss (Table B.1). Accordingly, the power received for a

Table B.1: System Specifications

Parameter	Value
$f_{Resonance}$	100kHz (T1), 200kHz (T2)
Distance in air	1m
T_{sweep}	8msec
V_{DD}	0.6V
BW	8kHz
$P_{rec,T1}$	$-1.7 \cdot 10log(d) - 30.37$ (dBm)
$P_{rec,T2}$	$-2.2 \cdot 10log(d) - 20.1$ (dBm)
SNR_{in}	>12dB
IRN_{RX}	$<9\mu V_{rms}$
f_{beat}	<6kHz

link built with two T2 transducers at 1m distance in air is measured as -64dBm. Considering that T2 will be used within its 10dB BW and reminding that ≈12dB SNR at the input of the receivers is needed to have a 90% detection probability with a ¡10^{-3} false alarm ratio [53], the required RX integrated noise should be lower than $9\mu V_{rms}$. As reported in Table B.1, using the above-mentioned system settings, an f_{beat} of ≈6kHz is estimated at 1m, which has to reside inside the bandwidth of the RX. The link losses for T1 at 1m are very similar, but the attenuation provided by that transducer is lower, and thus the RX noise level is defined by the link using T2.

B.4 Circuit Design

Fig. B.1b shows the top-level implementation of the RX, which comprises a single-ended inverter-based low-noise amplifier (LNA), a single-balanced passive mixer (SBPM), a closed-loop baseband amplifier (BBAMP), and a 10-bit SAR ADC, all sharing a single supply, V_{DD}, of 0.6V. The output of the LNA is DC coupled to the SBPM, which uses two nMOS transistors as a switch. After the high frequency harmonics of the mixer are filtered by the BBAMP, the signal is converted to the digital domain by a 10-bit SAR ADC, which has been presented in detail in [55]. The non-linearity and noise-level of the ADC are negligible for overall RX performance. A single-ended, open-loop topology is chosen in the LNA to save power and reduce the effect on the input noise of the rest of the front-end. Stabilizing the output DC voltage of the inverter-based amplifiers requires a DC feedback [79, 92]. In this design, as shown in Fig. B.4a, the DC feedback is applied using an error amplifier (EA) and an auxilary inverter, formed by M_{p1} and M_{p2}, put in parallel to the main input inverter (M_1, M_2). The auxiliary inverter is current starved with the transistors M_{cs1} and M_{cs2} to limit its power consumption. M_1 and M_2 are AC coupled to the transducers input, RX_{in}, and these transistors are separately biased. The DC gate voltages of M_1, M_{cs1}, M_2, and M_{cs2} are provided via pseudo-resistors and internal current mirrors. The EA is designed as a differential pair with active load and uses the same supply of V_{DD} as

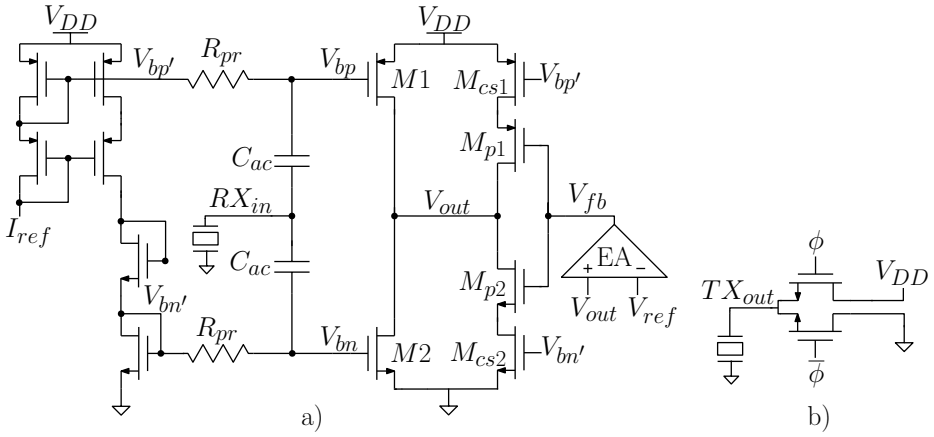

Figure B.4: Schematic of the a) LNA and its biasing network b) The output multiplexer as a TX.

in the LNA. To save power and to increase the output impedance, the transconductance of the auxiliary inverter is made much lower than the one of M_1 and M_2. All transistors in the LNA, bias network, and the EA are biased in weak-inversion region to maximize their g_m/I_D ratio. The proposed DC feedback method can compensate the errors due to mismatch in the biasing network and the LNA. Simulations predict that the output voltage is stabilized to V_{ref} with less than a 10mV error across PVT, when an ideal $V_{ref} = \frac{V_{DD}}{2}$ is used. The BBAMP uses a two-stage architecture with Miller compensation and provides a gain of 12dB determined by a capacitive feedback network (Fig. B.1b). The complete front-end is simulated to have a conversion gain of 43dB, a bandwidth of 20kHz, and an IRN of $7.8\mu V_{rms}$ while using a single 0.6V supply. The TX is designed as a simple multiplexer and comprises 2 nMOS transistors that connect the desired DC voltage to the transducer load, as shown in Fig. B.4b. The switches are designed to avoid voltage division with the impedance of the transducers at their resonance. The period of the driving signal is controlled by activating the non-overlapping clocks ϕ and $\overline{\phi}$, which are distributed to the switch transistors with on-chip buffers having a 1.2V supply.

B.5 Measurement Results

A 65nm CMOS process is used for fabrication and the die photos of the RX and TX are shown in Fig. B.5. The measured conversion gain and IRND of the RX are shown in Fig. B.6a and b, respectively. The RX has an IRN of $8.8\mu V_{rms}$ in the band 125Hz - 21.4kHz, which is sufficient for detecting beat frequencies at the target ranges. During characterization, an external reference current, I_{ref}, of 1nA is used. The LO required for the active tag (96kHz/192kHz), the Chirps for the ranger node, and the sampling clock (50kHz) for the ADCs are provided by the FPGA, derived from an external oscillator. The integrated RX draws a total measured current of

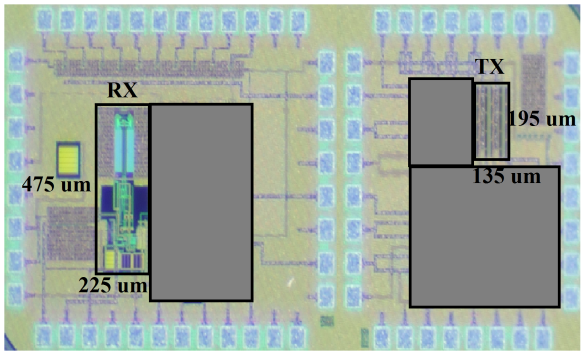

Figure B.5: Die photo of the RX and the TX. Only chip areas that are relevant to this paper are shown.

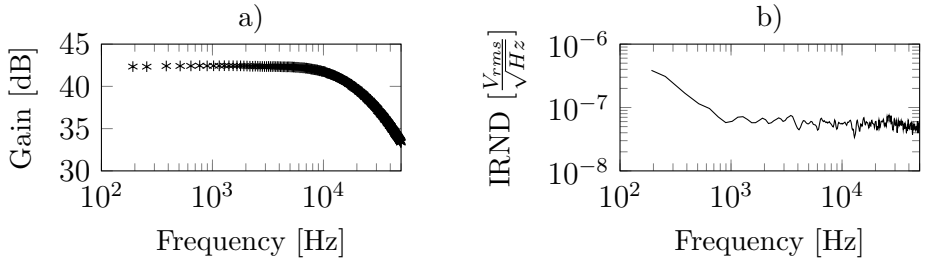

Figure B.6: a) Measured conversion gain of the RX. The maximum gain is 42.4dB @1kHz and the 3-dB BW is 21.4kHz. b) Input-Referred Noise Density (IRND) of the RX. IRND = $60nV_{rms}/\sqrt{Hz}$@1kHz is measured.

930nA from a 0.6V supply, therefore, dissipates a total power of $0.56\mu W$. The TX dissipates $1.59\mu J$ per Chirp when driving T2, and dissipates $1.07\mu J$ per Chirp when it drives T1. The measured TX efficiency (power transferred to the transducer as a fraction of the power required from the supply) when driving T1 and T2 with the Chirp signals is 58% and 44%, respectively. The proposed rangefinder system requires $2.67\mu J$ energy per distance measurement. This figure includes the power of the on-chip buffers used to distribute and drive the Chirps, the control phases of the TX and the sampling clock of the ADC. It excludes the digital power, the losses in the power management, and the power needed for generation of the on-chip current references and clocks. The baseband output of the active tag RX is recorded when the tag receives Chirp1r via T1. The corresponding transient output of the ADC and its spectrogram are shown in Fig. B.7, where the broadcasted Chirp BW of 8kHz can be appreciated. The active-tag then up-modulates this Chirp by simply XORing the ADC code with the fixed frequency 2·LO=192kHz, and broadcasts the resulting signal via T2. The spectrum of the data recorded by the ranger node after mixing the received Chirp2t with the original Chirp2r at 1m distance in air is depicted in Fig. B.8, where the highest frequency peak is defined as f_{beat}. To reduce the complexity in the digital domain, no additional filters are used, and the mixing spurs of the image Chirp are also visible in the spectrum. A proof-of-concept characterization of

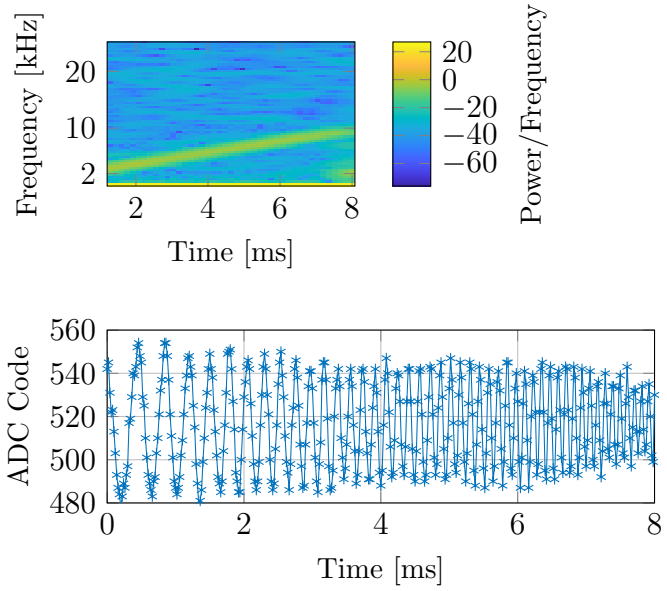

Figure B.7: Top: Spectrogram of the down-converted Chirp of the active tag. Bottom: The corresponding transient ADC output, coherent with the frequency-dependent attenuation of T1.

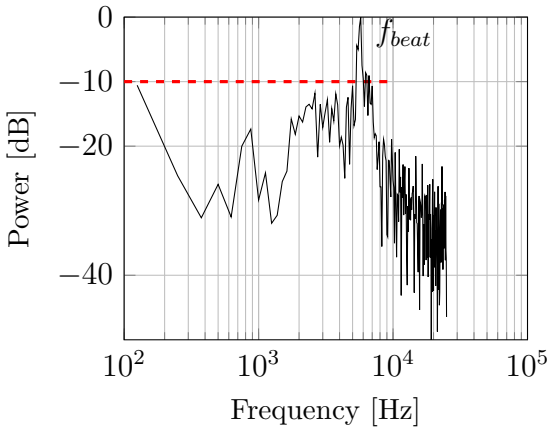

Figure B.8: A normalized spectrum of the measured ADC data at 1m.

the proposed rangefinder system up to 1m in air is summarized in Fig. B.9a, and the calculated absolute distance error is depicted in Fig. B.9b. The standard deviation of the absolute error is found to be 6.5mm. The FFT resolution is equal to the inverse of the T_{sweep}, which is 125Hz. This provides a minimum measurable distance (d_{min}) of 21mm and a theoretical measurement resolution (standard deviation of the error distribution) of $\frac{d_{min}}{\sqrt{12}} = 6.1mm$, which is in good agreement with the value determined experimentally. The memory needed for one measurement is 4kb.

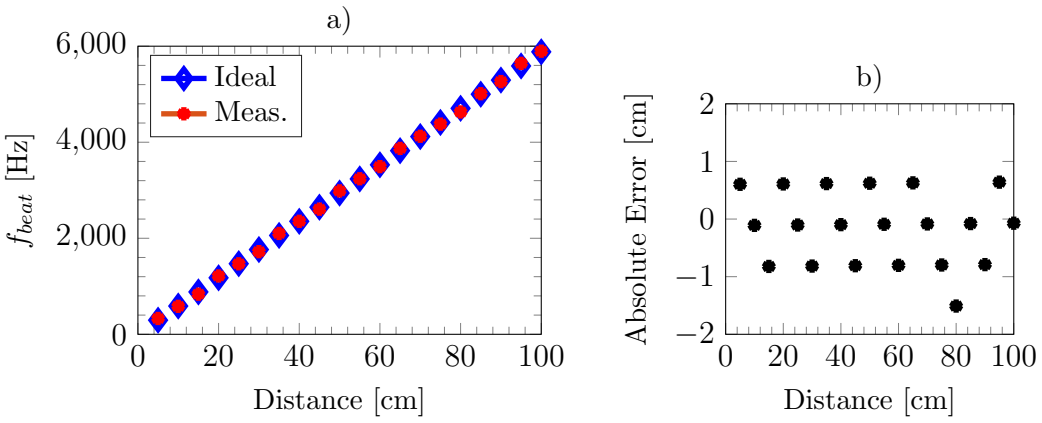

Figure B.9: a) FMCW Ranging Link Characterization b) Absolute error in the distance measurement.

Table B.2: Performance Comparison of the Proposed US Rangefinder

	[57]	[104]	**This Work**	
Method	ToF	Phase-shift	FMCW	
Target Reflector	Passive	Passive	Active	
Transducers	PMUT	Membrane	PZT	
Technology [nm]	180	800	65	
Min/Max Range [mm/m]	45/1	18/0.11	50/1	
Range Error [mm]	0.41 @0.5m	2.5@0.1m	6.5@1m	
Field of view	3D	1D	1D	
TX Supply [V]	32	5	0.6 + 1.2	
			T1	T2
Frequency [kHz]	220	100	98-106	194-202
TX Energy Consumption [μJ]	1.05	2800	1.07	1.59
RX Supply [V]	1.8	5	0.6	0.6
RX Energy Consumption [μJ]	1.6	3700	0.004	0.004
Total Energy per Measurement [μJ]	2.65[a]	6500	2.67	

a: Energy consumption is scaled per channel excluding the power overhead of the digital circuits.

B.6 Benchmark and Conclusion

The performance of the proposed US rangefinder and its comparison with prior-art is summarized in Table B.2. The work in [104] is based on the detection of phase-shift, and the work in [57] is based on a ToF measurement of the echoes coming from passive reflectors in air. Contrary to the prior-art, this work enables US distance measurement between active tags while minimizing interference from passive reflec-

tors. For this purpose, our work uses two separate frequency bands to distinguish the active responses from the passive reflections of the environment. In our work, due to the narrow-band transducers used to broadcast the Chirps, the range resolution of the distance measurement is 6.5mm, which is tolerable in the applications considered. Thanks to the power-aware design methodology for the rangefinder system described in this paper, our work dissipates $2.67\mu J$ per measurement. The response of the active tags will be transmitted only when they receive a signal in a separate frequency band, thus their operation is independent of each other and the need of a global synchronization is eliminated. The extraction of distance information from raw ADC data is done outside the nodes, after recuperating them. The energy needed to write the raw data in a memory and the power needed to keep them can be negligible when compared, respectively, to the measurement energy and the normally-on node power [76].

Appendix C

A -81.6dBm Sensitivity Ultrasound Transceiver in 65nm CMOS for Symmetrical Data-Links

Gönenç Berkol, Peter G. M. Baltus, Pieter J. A. Harpe, and Eugenio Cantatore

Published in IEEE 45th European Solid State Circuits Conference (ESSCIRC). IEEE, 2019.

This paper presents the design and experimental characterization of an ultrasound transceiver. The transceiver includes an on-chip transmitter and a receiver to be used in a symmetric data-link, where each sensor node has limited energy resources and is operated in air or a fluidic environment. The receiver and the transmitter operate from a 0.8V supply and consume 1.18μW and 50μW, respectively, while exchanging data at 1kbps data-rate. The receiver sensitivity is -81.6dBm at a 10^{-3} Bit Error Rate (BER) level, which enables an experimentally verified transmission over 3.2m in air and a predicted transmission distance in water in the order of 2km, with a measured energy per bit performance of 51.18 nJ/b.

C.1 Introduction

Using ultrasound (US) has become popular in emerging communication applications where ultra low-power operation is desired. The relatively low operating frequency range compared to RF makes US a promising approach for ultra low-power systems. Prior-art [45, 46, 50] uses US in asymmetric data-links, where data exchange between sensors is performed from a resource-rich external master node to resource-limited slave nodes. The slave nodes are based on an always-on US receiver which is used to save energy during a long-operation time and to activate the main RF radio when high bitrate communication is desired. In this paper, we propose a symmetric US communication link to be used in a network of identical sensor nodes having a limited energy budget and immersed in a fluidic environment. US communication is attractive in this case for its favorable attenuation characteristics compared to RF waves [106]. The proposed sensor network can be deployed for energy-constrained, low bit-rate applications including environmental monitoring, detection of defects in pipelines and water distribution networks. In this work, the design of an US transceiver employing On-Off Keying (OOK) for a symmetric US data-link will be introduced. The US receiver (RX) comprises a low-noise amplifier (LNA) and a 10bit SAR ADC. On the transmitter side (TX), a class-D buffer has been chosen due the relaxed linearity constraints of OOK. The paper is organized as follows: In Sections II and III, the system design and circuit details are discussed. The measurement results are presented in Section IV. The performance of the US transceiver is benchmarked against prior art in Section V. This study is concluded in Section VI.

C.2 System Design

A commercial US transducer [20] with a resonance frequency (f_R) of 40kHz is chosen. The system transfer characteristic, measured by exciting the transducer and recording the electric signal received from an identical transducer placed at 6cm distance in air is shown in Fig. C.1. The bandwidth (7.1kHz) and the Q-factor (5.6) of the system are enough to support simple modulation schemes. To minimize the complexity of the base-band demodulation circuitry, OOK communication is selected. The time chosen for the "one" symbol is 3Q cycles, of which Q cycles are needed to start up and Q cycles to extinguish the oscillation. The time for the "zero" symbol is identical. Considering this, a data rate of 1kbps is specified. The transducer can be modeled by its electrical input capacitance, C_{in}, in parallel with a series resonator comprising R_m, L_m and C_m, which models the transducer's mechanic resonance [45]. The values of the different components in the transducer equivalent model have been estimated by impedance measurements and are reported in Table C.1. When driving the US transducer, a big portion of the used energy is dissipated to charge and discharge the electrical input capacitance C_{in}. To minimize this loss, a 0.8V supply is chosen for the class-D buffer. Considering that transmitting a one and a zero have equal probability, the total transmitter power. P_{TX}, is simulated to be 47.8μW when the buffer drives

Table C.1: System Specifications

Parameter	Value
f_R	40kHz
Data Rate	1kbps
C_{in}	2.1nF
V_{DD}	0.8V
R_m,L_m,C_m	434.4Ω, 87mH, 0.192nF
P_{TX}	47.82μW
$Duty_{TX}$	2.5%
$P_{RX} \approx P_{TX} \cdot Duty_{TX}$	1.2μW
NEF	≈ 2
BER	$< 10^{-3}$
Sensitivity	<-80dBm
Distance in water	$\approx 2km$

the electrical equivalent model of the transducer at frequency f_R. It is assumed that the transmitting node sends once per second a 25b message, which contains e.g. data measured from internal sensors. This means that the transmitter can be duty cycled ($Duty_{TX}$) by a factor 25/1000=2.5%, bringing its average power consumption down to $\approx 1.2\mu$W. A similar power budget is allocated for the receiver to balance the power used in the overall transceiver. The sensitivity level of the receiver can be estimated by assuming for the LNA a noise-efficiency factor (NEF) of 2 and a bias current of 0.8μA. In this case, the input integrated noise voltage is calculated as $2.9\mu V_{rms}$ in the transducer bandwidth. For a 10^{-3} BER in OOK, 16dB SNR at the input is sufficient, which means that -82dBm input signal can be successfully received, as shown in Table C.1. Here, the effect of the quantization noise of the ADC at the input is assumed negligible, while a power of about 0.5μW is assigned to the ADC. The maximum communication distance that can be reached with this sensitivity is investigated by building an underwater lab setup in a water tank. The tank measures 0.4m by 1.1m by 0.5m and is filled with tap water to a depth of 0.25m. The TX transducer is driven by a $0.8V_{pp}$ square wave at f_R, while the power received by the RX transducer is recorded. Fig. C.2 shows the underwater link characterization up to 1m distance, where the received power is modeled [106] according to

$$P_{rec} = -k \cdot 10 \log d + P_0 \tag{C.1}$$

In this equation d is the distance in cm, k is the path loss coefficient (which is found to be 1.05) and P_0 is the initial power loss of -25.7dBm. This result is similar to what was reported in [106] and includes attenuation and path loss together. The received power at room temperature at 1m is ≈-47dBm. The outcome of this measurement is promising in the sense that, with the sensitivity we aim at, a communication distance in the order of 2km in water can be estimated using Eq.C.1. However, since the OOK communication is susceptible to echoes, the maximum achievable communica-

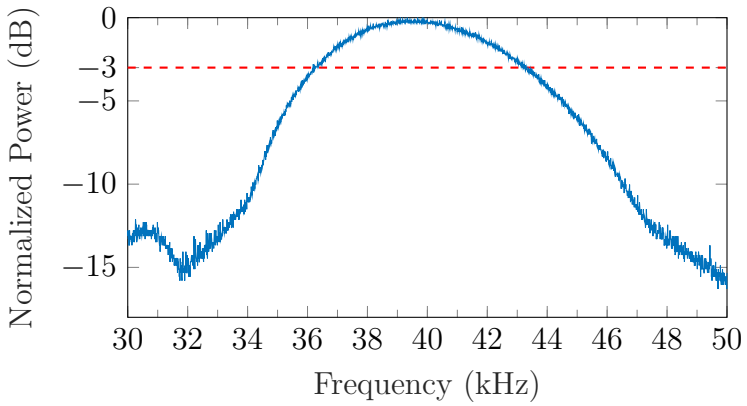

Figure C.1: Transducer to transducer characterization. The resonance frequency is ≈40kHz and the bandwidth is 7.1kHz (between 36.2kHz - 43.3kHz). The Q factor of the system is 5.6.

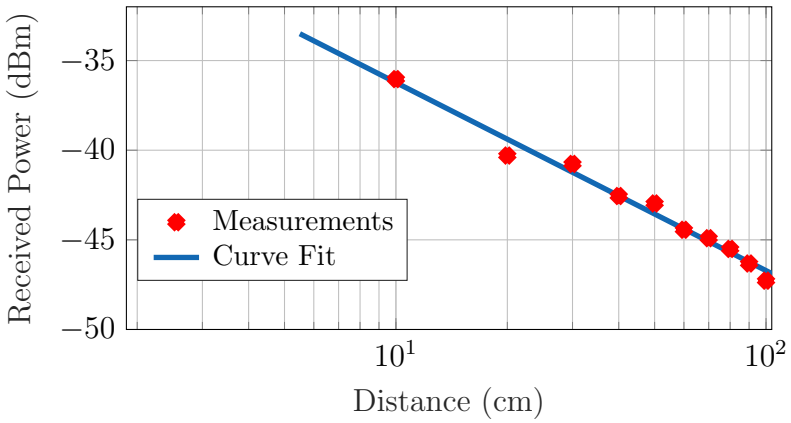

Figure C.2: Underwater received power characterization.

tion distance will be influenced by the multipath propagations in the environment.

C.3 Circuit Design

The class-D buffer in [29] is shown in Fig. C.3 and re-designed to drive the US transmitting transducer. It consists of a level shifter input stage and 6 stages of inverter chain. Each stage is tapered by a factor 7 to drive a large capacitive load up to 2nF. In this circuit, thick-oxide transistors have been used together with a separate supply level, V_{DDH}, which can be set higher than the one used for the receiver, to further increase the communication distance, or to cope with mediums like air where the attenuation is larger than in water. However, in this paper, the same supply is used for both TX and RX. The circuit proposed for the US LNA is shown in Fig.

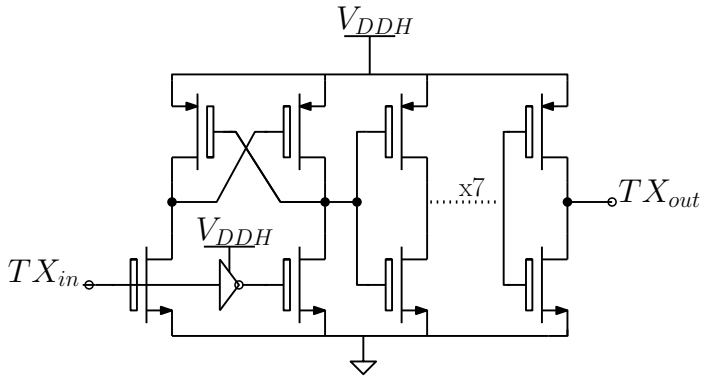

Figure C.3: Schematic of the Transmitter

C.4a. It exploits an inverter-based amplifier in open-loop to maximize gain and reduce the influence of the quantization noise of the ADC on the input-referred noise. Poor PSRR performance of the inverter-based topology can be tolerated in our application as we foresee a battery operated system, where the DC voltages are provided via external voltage regulators. The power overhead due to the LDOs is not considered in the rest of the paper. The inverter-based topology is chosen as both the pMOS (M_1) and the nMOS (M_2) transistors contribute to the total transconductance for a given current, thereby increasing current efficiency and enabling an NEF of 2 [55]. The capacitors C_{ac}, are used to AC couple the inverter to the input of the receiver V_{in}. Both transistors in the inverter are biased in the weak-inversion region and sized to have a gm/I_D ratio of about 31 [V^{-1}]. A reference current I_{bias} is provided to the chip, and internally mirrored (as in Fig. C.4b) to bias the LNA and the error amplifier. The DC gate voltage of M_1 and M_2, V_{bp} and V_{bn}, are provided via pseudo-resistors composed of two back-to-back diodes as shown in Fig. C.4a. The value of C_{ac} is 3.2pF and the pseudo-resistor value is simulated to be more than 3MΩ across PVT variations, so that the high-pass corner frequency is set below 20kHz. The DC point at the output of the inverter is stabilized via a negative feedback. This is achieved by comparing the LNA output, V_{out}, to a reference voltage, V_{ref}, and feeding back the error signal, V_{fb}, to the gate of two current control transistors M_{p1} and M_{p2}. The DC feedback can efficiently compensate the errors due to leakage currents flowing in the pesudoresistors, and to mismatch between the biasing network and the transistors M_1 and M_2. M_{p1} and M_{p2} can indeed source (or sink) a suitable current in the output node, keeping the output DC voltage at the desired value. The schematic of the error amplifier is shown in Fig. C.4c. Its output is connected to a 3.2pF capacitor, to filter out the signal from the DC stabilization loop. According to simulations, the feedback is able to stabilize the DC point with less than 7mV DC error across PVT variations. The output of the LNA is DC coupled to the ADC (Fig. C.4a), which uses the same reference voltage, V_{ref}. The 10 bit asynchronous SAR ADC is designed as in [55]. The total current consumption of the LNA (including bias network and error amplifier) is simulated as 830nA and the sampling clock of the ADC is set to 400kHz to make the contribution of the quantization noise to the total input referred

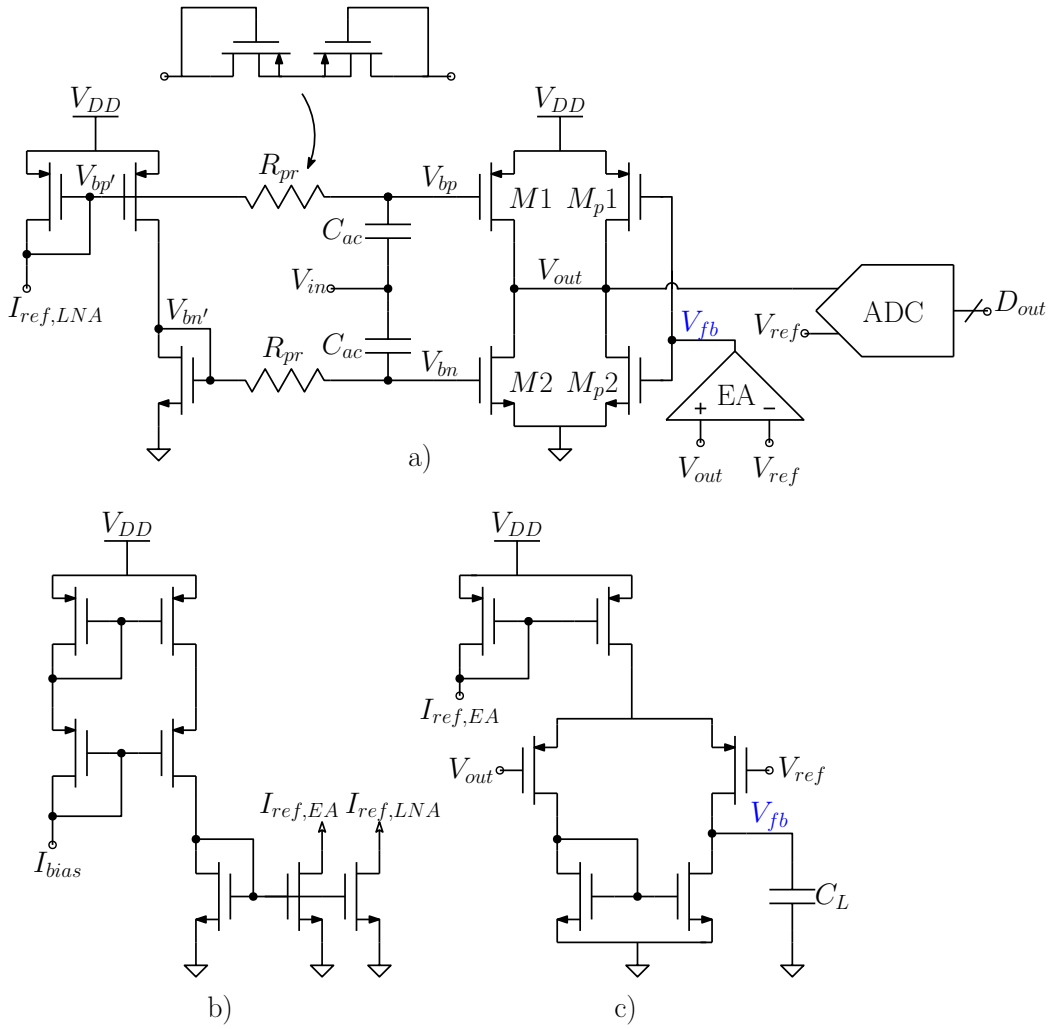

Figure C.4: a) Inverter-based LNA and its bias network including pseudo-resistors and a coupling capacitor, C_{ac}, of 3.2pF. The LNA output is DC coupled to a 10bit SAR ADC b) Bias circuit for mirroring the external bias current c) Error Amplifier with a load capacitance, C_L, of 3.2pF

noise negligible. The simulated ADC power is $\approx 0.51\mu$W. A simulated input-referred noise density (IRND) of $20\frac{nV}{\sqrt{Hz}}$ is obtained at the typical corner, which enables a sensitivity level ¡-80dBm.

C.4 Measurement Results

A 65nm CMOS process is used for fabrication and the die photo of the proposed ultrasound transceiver is shown in Fig. C.5. The measured transfer curve of the LNA is shown in Fig. C.6, where a 30.7dB voltage gain is measured at $15kHz$ and the 3dB bandwidth (BW) is 40kHz. In Fig. C.7, the measured IRND of the LNA is

shown. The total integrated noise inside the transducer bandwidth is measured to be $2.2\mu V_{rms}$. The sensitivity level is validated with electrical BER measurements, where an OOK modulated signal with different amplitudes provided by a bench-top arbitrary signal generator (AWG Keysight 33500B) is given to the input of the receiver. 50dB attenuation is applied to the AWG output to bring the signal amplitude to the desired level. Fig. C.8 shows BER plots for this electrical input signal, where a $-83dBm$ input signal at 1kbps data-rate is demodulated with a 10^{-3} BER. Afterwards, an

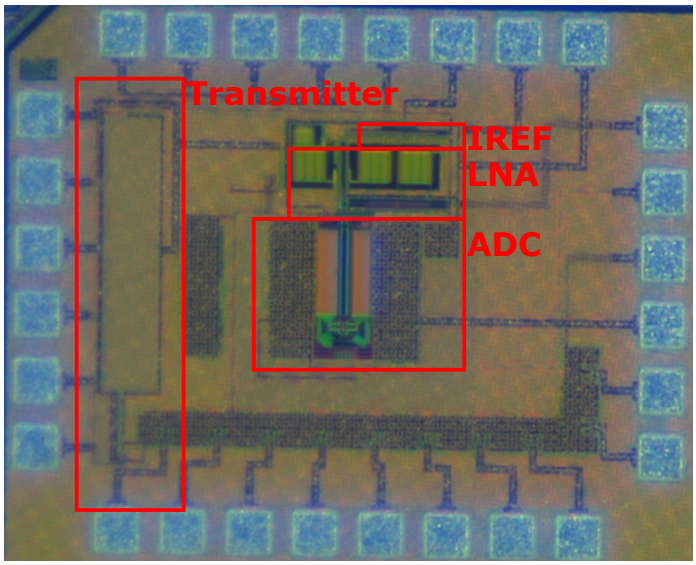

Figure C.5: Die photo

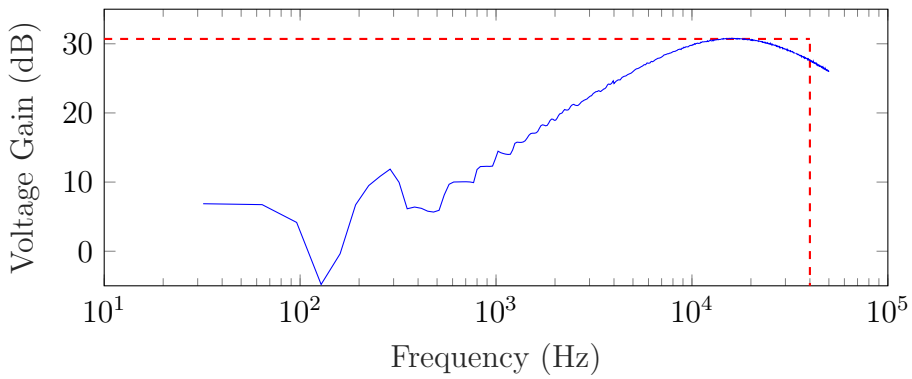

Figure C.6: Measured transfer curve of the LNA. The maximum gain is 30.7dB @15kHz and the 3-dB BW is 40kHz.

underwater test setup is built with transmitter, receiver and two US transducers. When a 40kHz, $0.8V_{pp}$ square wave input signal is given to the TX chip, around

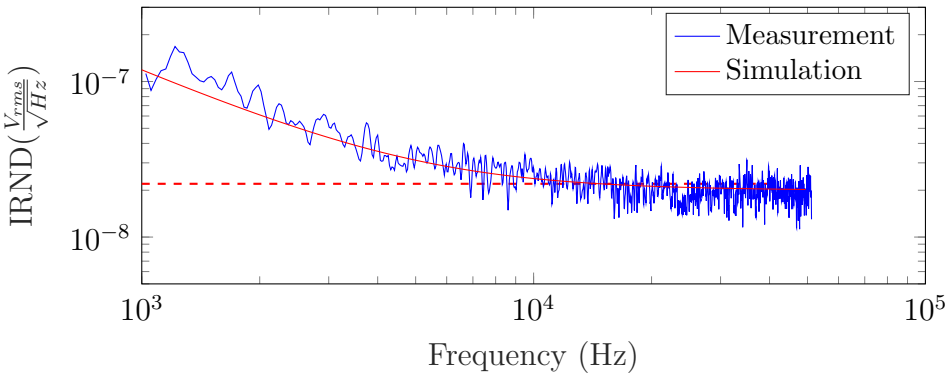

Figure C.7: Input-Referred Noise Density (IRND) of the LNA. IRND = $22nV_{rms}/\sqrt{Hz}$@40kHz is measured.

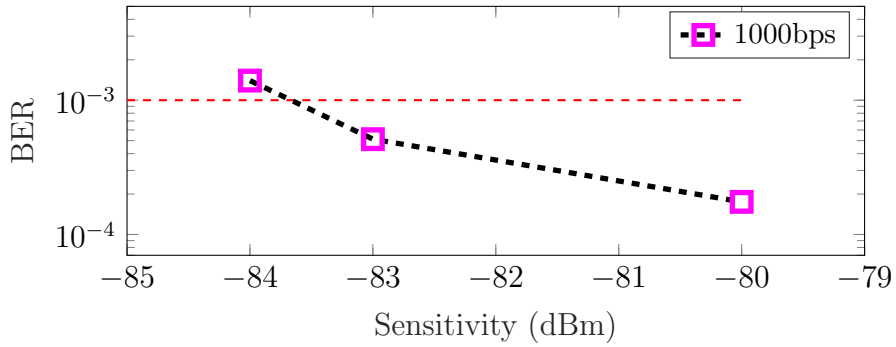

Figure C.8: BER plots for an electrical input signal of variable amplitude provided to the receiver.

$\approx 80mV_{pp}$ signal (corresponding to >54dB SNR at the input of RX) is measured at 1m distance in the water tank. As the achievable communication distance in water exceeds the limits of a standard lab, we built another measurement test setup in air, as shown in Fig. C.9, to be able to test the RX sensitivity at a manageable distance between the transducers. Here, OOK modulated random bits are generated in MATLAB and applied via an AWG to the transmitter chip, which drives the TX transducer. The resulting ultrasonic signal from the RX transducer is read-out via the receiver chain and the ADC output, D_{out}, is recorded via an external FPGA and transferred to a computer. There, a simple demodulation algorithm based on a band-pass filtering and a thresholding is implemented to detect the incoming bits. Due to the additional noise and echoes coming from the setup environment, a 10^{-3} BER with a sensitivity of -81.6dBm was achieved at a communication distance of 3.2m. The total receiver power consumption of the LNA and ADC is measured as $1.18\mu W$. The measured power consumption of the transmitter is $50\mu W$. As a result, the overall energy consumption of the TX+RX link is measured as 51.18 nJ/bit. Furthermore, considering the Figure-of-Merit for wake-up receivers proposed [105] as $FoM_{WuRx} = Energy(J)/bit \cdot P_{sensitivity}(W)$, our receiver achieves a FoM_{WuRx} of $0.82 \cdot 10^{-20}(J/b \cdot W)$. FoM_{WuRx} is measured excluding the power required to generate

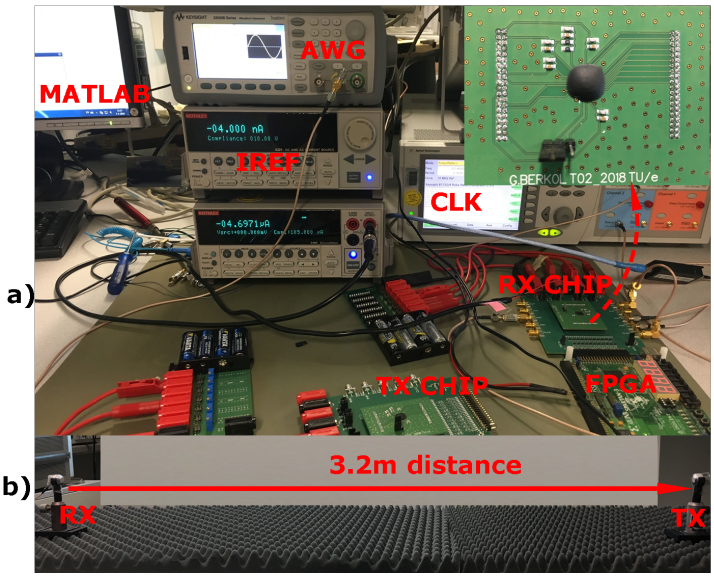

Figure C.9: Test Setup a) Bench-top setup and experimental boards b) Transducers separated by 3.2m in air

the ADC clock and the references. However, by reviewing relevant prior art [55, 107] these overheads can be estimated to be much lower than the RX power and thus will not significantly change the overall results. A simple digital backend based on a threshold detector has also been implemented at transistor level and simulated: its power overhead (46nW) is negligible too in the total RX power budget.

Table C.2: Performance Comparison of the Proposed US Transceiver with prior art

	Yadav [45]	Fuketa [50]	Rekhi [46]	**This Work**
Technology [nm]	65	250	65	65
Carrier Frequency [kHz]	40	41	57	40
Supply Voltage [V]	0.6	0.3	0.5	0.8
Modulation	OOK	OOK	OOK	OOK
Data Rate [bps]	250	250	336	1000
Receiver Power [μW]	4.4	1	0.008	1.18*
Sensitivity [dBm]	-81	-81	-59.7	-81.6
FOM_{WuRx} [$(J/b) \cdot W \cdot 10^{-20}$]	13.98	3.18	2.55	0.82
Transmitter Power [μW]	16	1000	N/A	50
Distance- in air [m]	8.6	6.3	3.3	3.2
Distance- in water [km]	N/A	N/A	N/A	2
FoM=Energy/Bit (full link)	81.6nJ/b	4μJ/b	N/A	51.18nJ/b

*Excludes the power needed for the ADC clock and the reference generation.

C.5 Discussion

The performance of the proposed US transceiver and its comparison with recent integrated US receivers is summarized in Table C.2. The work in [46] achieves the lowest US receiver power while relaxing sensitivity. The works in [45, 50] are designed as a wake-up receivers for an asymmetric US link, and achieve US receiver sensitivity of $-81dBm$. The work in [45] achieves a longer communication distance with less transmitting power, exploiting an optimized TX transducer with high transmit efficiency and a different, optimized receiving transducer. In contrast, our work uses the same commercial transducer for both transmission and reception. The proposed receiver achieves the best measured sensitivity of -81.6dBm, which corresponds to a communication distance of 3.2m in air with the transducers used. Based on measurements, the communication distance predicted in water would be 2km to reach a 10^{-3} BER level. To the best of our knowledge, the proposed transceiver achieves the lowest energy per bit performance of 51.18nJ/b and the best FOM_{WuRx} of 0.82 $(J/b) \cdot W \cdot 10^{-20}$ reported among US transceivers.

C.6 Conclusion

Ultrasound communication is useful in resource-limited sensor networks using low bitrate communication and deployed in fluidic environments. This work focuses on the design of a symmetrical US communication link, where a similar average power budget is allocated to the transmitter and the receiver to efficiently use the available energy. Measurement results show that the proposed circuits achieve this goal at 1kbps data-rate with a state-of-the-art sensitivity, energy per bit, and FOM_{WuRx} for a US transceiver.

Acknowledgement

This work has been funded by the European Union′s Horizon 2020 research and innovation programme under grant agreement No 665347.

Appendix D

Design of a Low-power Ultrasound Transceiver for Underwater Sensor Networks

Gönenç Berkol, Peter G. M. Baltus, Pieter J. A. Harpe, and Eugenio Cantatore

Published in 14th Conference on Ph. D. Research in Microelectronics and Electronics (PRIME). IEEE, 2018.

This paper presents an ultrasound (US) transceiver including a transmitter and a receiver for underwater wireless sensor nodes, where low-power operation is desired to extend the life-time of the network. A system-level analysis of the underwater communication has been performed by taking into account the underwater propagation and the medium characteristics to show their impact on the overall performance. In addition, a low-noise amplifier using an inverter-based topology has been introduced to ensure power efficiency of the receiver, where a bulk-feedback method is proposed to stabilize the output bias point of the inverter. Simulation results show that the proposed transceiver has a scalable power consumption from 1.95μW to 10.4μW while achieving 100μV to 20μV sensitivity at a 10^{-3} BER level.

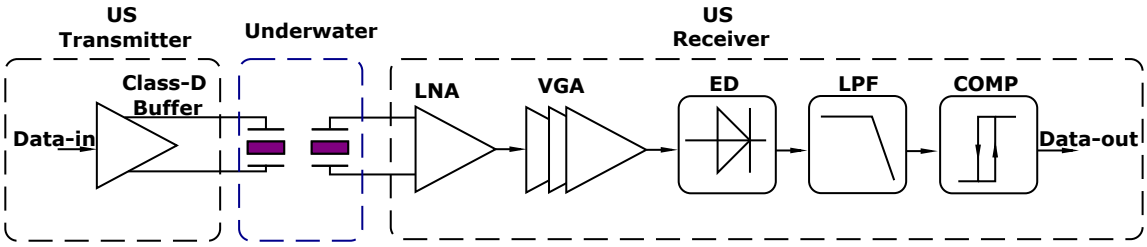

Figure D.1: The proposed architecture of the US transceiver. The transducer has a band-pass transfer centered around its resonance frequency.

D.1 Introduction

Underwater wireless sensor networks (UWSNs) are useful for various emerging applications such as environmental monitoring, early detection of disasters, and localization in pipes [8]. A low-power transceiver is required in these applications to achieve sufficiently long life-time of the network since the sensor nodes are required to operate continuously. US signals are commonly preferred over RF signals for the data exchange among sensor nodes because of their relatively low attenuation in underwater conditions [108]. On the other hand, US data-rate is limited due to the low speed of US signals, and the communication bandwidth is bounded by that of the transducer, which is much lower compared to terrestrial RF applications [109]. The limited bandwidth of the transducer limits the choice of the communication schemes to low-complexity amplitude or frequency modulation methods, which can be sensitive to e.g. multi-path propagation and interference in the communication among different sensor nodes. In this work, a design procedure for a low-power US Transmitter and US Receiver for UWSNs will be described. In order to determine the power trade-off between transmitting and receiving the US data, a system level analysis will be performed, where a top-down approach is used to capture the effects of the transducer and the underwater medium as well as the circuit parameters. The proposed US transceiver is shown in Fig.D.1. An on-off keying (OOK) scheme has been chosen for the communication due to its simplicity and low power operation [49]. The receiver comprises a low-noise amplifier (LNA), a variable gain amplifier (VGA), an envelope-detector (ED), a low pass filter (LPF), and a comparator to reconstruct the incoming data. To minimize power consumption of the amplifiers, an inverter-based topology has been used, where a bulk feedback method is proposed to stabilize the output bias point of the inverter. On the transmitter side, a power-efficient two-stage class-D buffer has been used thanks to relaxed linearity constraints of the OOK scheme. The paper is organized as follows: In Section II, the system-level analysis of the US transceiver for underwater communication is performed. The details of the circuit design are presented in Section III. Post-layout simulation results are given in Section IV. The performance of the US transceiver with respect to system-level analysis is discussed in Section V. Finally, Section VI concludes this study.

D.2 System Level Analysis of the Underwater Communication

Piezoelectric transducers are considered in this work as they do not require external bias [109]. These transducers can be simply modelled by their parallel capacitance, C_p, in transmitting mode [61]. As a result, the dominant power is spent by the transmitter circuit to charge and discharge C_p. Furthermore, since an OOK based scheme is chosen, linearity is not a relevant factor. Thus, it is possible to use a class-D output buffer [109]. As a result, the power consumption of the transmitter, P_{Tx}, can be calculated as

$$P_{Tx} = \frac{C_p \cdot V_{drive}^2 \cdot f}{\alpha}, \qquad [\text{W}] \tag{D.1}$$

where V_{drive} is the amplitude of the driving signal, f is the data rate, α is the efficiency of the buffer. Assuming a single omni-directional transducer working in its linear regime, the applied voltage, V_{drive}, will generate a source level pressure, SL, which can be found as

$$SL = S_v + 20\log(V_{drive}), \qquad [\text{dB } re \text{ µPa}] \tag{D.2}$$

where S_v is the transmit sensitivity of the transducer. The passive sonar equations [108, 110] can be used to estimate the pressure level at the receiver. In this case, the received sound pressure level, SPL, can be calculated as

$$SPL = SL - TL, \qquad [\text{dB } re \text{ µPa}] \tag{D.3}$$

where TL is the transmission loss of the environment. The corresponding received voltage level, V_{rec}, is given by

$$SPL = |S_r| + 20\log(V_{rec}), \qquad [\text{dB } re \text{ µPa}] \tag{D.4}$$

where $|S_r|$ is the receive sensitivity of the transducer. As a result, the relationship between V_{drive} and V_{rec} can be obtained by substituting equations (D.3) and (D.4) into (D.2) to write

$$\begin{aligned} V_{drive} &= V_{rec} \cdot 10^{\frac{|S_r| - S_v + TL}{20}} \\ V_{drive} &= V_{rec} \cdot K, \qquad [\text{V}] \end{aligned} \tag{D.5}$$

where the constant K captures the combined effects of the transducer, the communication frequency and distance, and the medium of interest. The level of V_{rec} is important for the estimation of the power consumption of the receiver, since it determines the signal-to-noise ratio (SNR). Moreover, assuming that the VGA provides sufficiently large gain to suppress the noise and non-linearity of the ED, the noise factor of the LNA basically determines the input noise level of the front-end, which makes its power consumption dominant in the receiver chain. To estimate the power

consumption of the LNA, the noise-efficiency factor (NEF) of an amplifier can be used. It is defined as

$$NEF = V_{in,noise}\sqrt{\frac{2I_{amp}}{\pi \cdot U_t \cdot 4kT \cdot BW}}, \tag{D.6}$$

where $V_{in,noise}$ is the total input-referred rms noise voltage, U_t is the thermal voltage, k is the Boltzmann constant, T the temperature, I_{amp} and BW are the current consumption and the bandwidth of the LNA. The ratio between V_{rec} and $V_{in,noise}$ needs to be larger than 12dB to have 10^{-3} bit error rate in OOK [49], and BW can be assumed to be equal to the transducer bandwidth. Therefore, given that NEF of 2 is achievable with inverter-based LNA topologies [55], I_{amp} and thus the power consumption of the LNA can be calculated. Fig.D.2 shows the estimated amount of

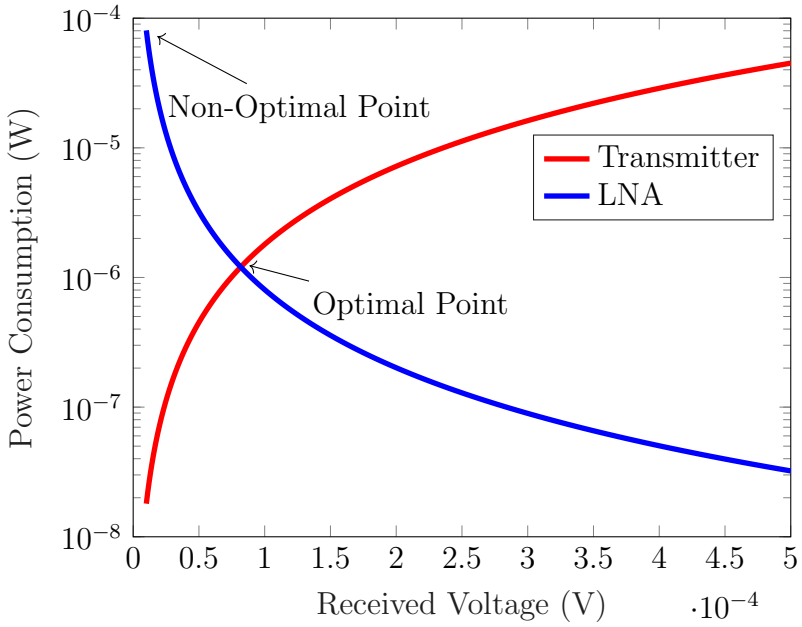

Figure D.2: Power consumption behaviour of Transmitter and LNA

power consumption in the transmitter and the LNA with respect to the amplitude of the received voltage, assuming a commercial transducer [111] is used in a shallow water[1]. Further assumptions are: 80% efficiency of the transmitter, C_p of 1nF, the communication distance is $10m$, the bandwidth is $50kHz$, the data rate is $250bps$, and the supply voltage of the LNA is $0.6V$. As a result, the power of the LNA dominates when a higher sensitivity must be achieved, whereas the transmitter power dominates when sensitivity is relaxed. It should be noted that in this discussion no duty-cycling is considered. The methodology described in this section indicates that there is an optimum power consumption for the underwater US transceiver when the performance

[1]For a communication distance of $10m$ and a frequency of $200kHz$, the value of TL in shallow water is calculated to be 30dB at 27 °C temperature [108], and around $20dB$ margin is added to TL to account for the additional losses and the variation of the underwater medium [110].

of the receiver and the transmitter are considered together, rather than focusing on the performance of the individual blocks.

D.3 Circuit Design

D.3.1 Low Noise Amplifier and Variable Gain Amplifier

A voltage amplifier with high input resistance is desired for the piezo transducers due to their relatively low impedance at the resonance frequency [61]. A closed-loop capacitor feedback architecture as shown in Fig.D.3 is selected for the LNA. An inverter-based topology is chosen for the core amplifier to increase the transconductance and improve the NEF. No current sources in series with the inverter are used

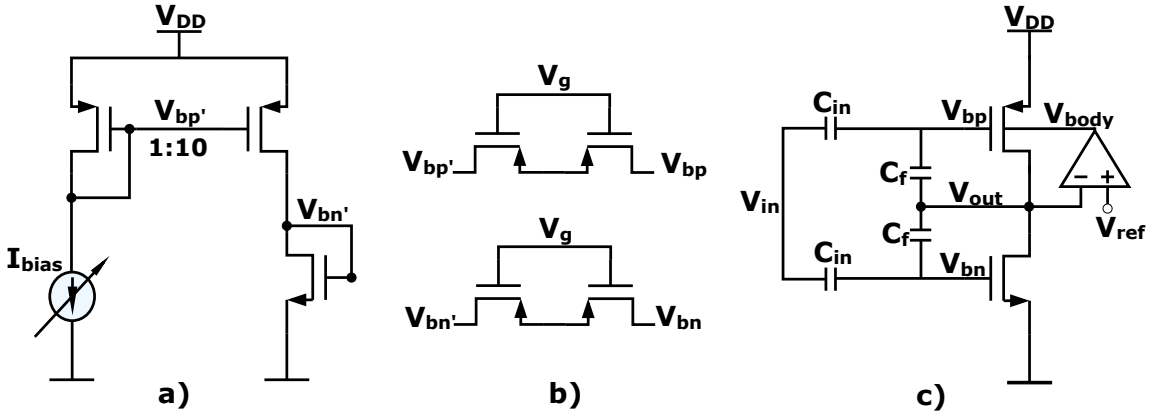

Figure D.3: Circuit implementation of the LNA a) Biasing current mirror b) Pseudo-Resistors c) Capacitive-feedback amplifier with bulk-feedback.

to bias it. This makes possible to lower aggressively the supply voltage, V_{DD}. The inverter transistors are biased in weak inversion and use relatively large aspect ratio to maximize the current efficiency. To reduce the effects of parasitic capacitors on the in-band gain, the capacitor splitting method [79] is applied and the transistors are biased separately. The bias current, I_{bias}, is multiplied 10 times by the the current mirror. The gate voltages for the input transistors (V_{bp} and V_{bn}) are provided through pseudo-resistors (PRs) having a large resistance (100MΩ to 10GΩ) to set the high-pass corner below 1kHz. The gate voltage (V_g) of the PRs is provided separately to control their resistance against process variations. An important point in the inverter-based topology is to stabilize the output bias point against process variations and mismatches in the biasing networks. This can be achieved by applying a negative feedback to control the pull-up current provided by a transistor in series with the inverter [55], or to control the gate bias of one of the transistors in

the inverter [79]. The former option limits the minimum V_{DD} level, whereas the latter results in extra parasitic capacitance to the gate of one of the input transistors, which degrades the gain and the noise performance. Although this problem can be solved via a dynamic bias loop [79], this technique is not applicable to continuous operations since it requires a pre-determined on and off time of the LNA. To solve this problem, a bulk-feedback method is proposed, where the negative feedback is applied to the bulk terminal of the p-type transistor to control its threshold voltage via the body-effect. The output DC point is compared to a mid-rail reference voltage (V_{ref}) and the error signal is fed back to the bulk terminal by an error amplifier (EA), thereby avoiding parasitic loading on the gate of the input transistors. On the other hand, this method requires higher EA gain compared to the method in [79] due to reduced bulk transconductance, and the EA output voltage should be around V_{DD}. As a result, a supply voltage (V_{DDH}) higher than V_{DD} is used for the EA, which is built as a conventional folded-cascode amplifier with diode-connected load [54]. The power overhead is negligible since the bias current of the EA is kept to $10nA$ to slow down its operation. A similar topology is used for the amplifiers of the VGA; here five inverter-based stages like the one depicted in Fig.D.3 are cascaded to provide high gain, as shown in Fig.D.4. A reduced closed-loop gain with respect to the LNA

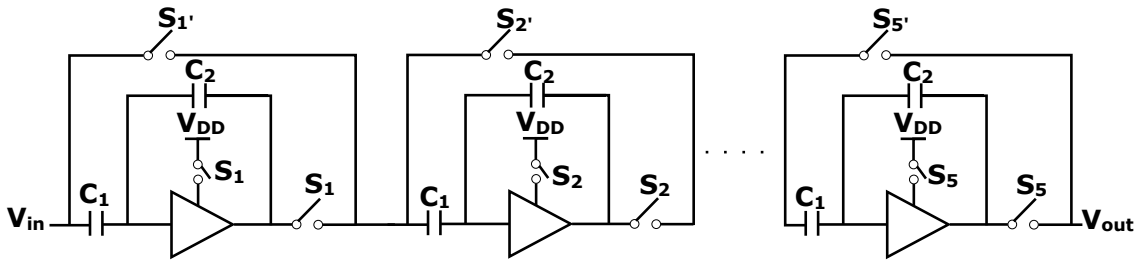

Figure D.4: Schematic diagram of the VGA.

as well as reduced bias current is used for the VGA stages since these amplifiers are not noise-limited. By appropriately selecting the switches (S_1 to S_5), the number of cascaded stages, and thus the total gain can be changed.

D.3.2 Envelope Detector, Low Pass Filter, and Comparator

The amplitude of the modulated signal can be extracted by using the ED, where a common drain topology [112] has been chosen as shown in Fig.D.5a. The transistor is biased in weak-inversion to provide the non-linearity. A $5pF$ capacitance C_L is used as hold capacitor. The ED is followed by the LPF given in Fig.D.5b, which is implemented as a $Gm - C$ filter for low-power operation. A simple inverter is used as a transconductance block. After the signal is squared and filtered, a hysteresis comparator as shown in Fig.D.5c has been used to compare the amplitude with an external reference (V_{ref2}) and obtain a digital output signal.

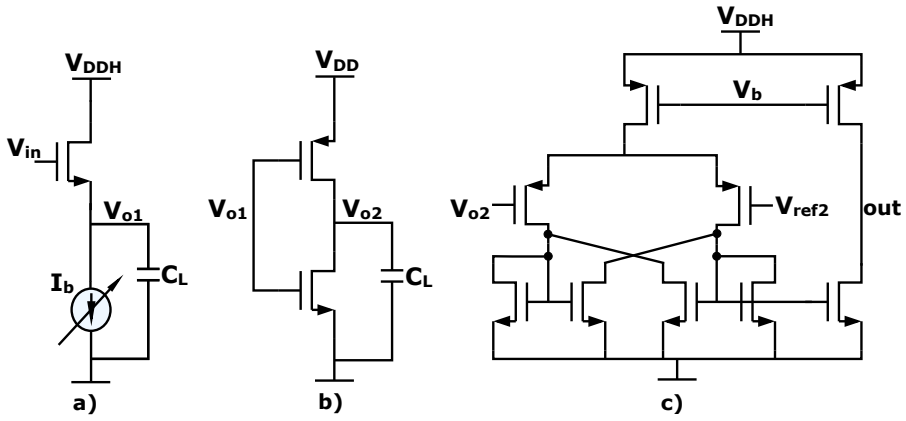

Figure D.5: The schematic of the a) ED b) LPF c) Comparator (The biasing network of the circuits are not shown for simplicity)

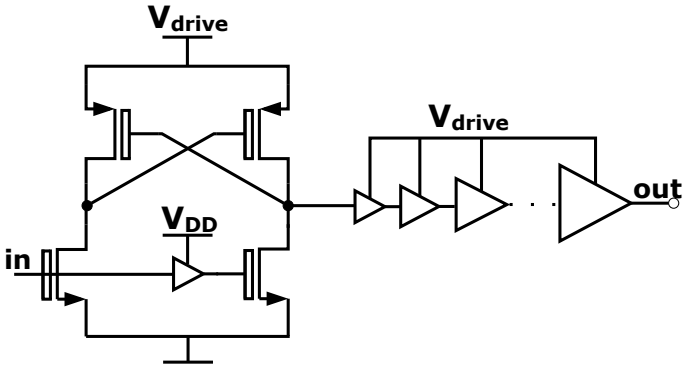

Figure D.6: The schematic of the Transmitter

D.3.3 Transmitter

As discussed in section D.2, a class-D buffer as shown in Fig.D.6 is used as a transmitter. It is formed by a chain of inverters sized to drive large capacitance load of 1nF. In this circuit a level shifter and inverters using 3.3.V transistors have been used, to enable to use a separate supply level, V_{drive}, higher than the one used in the receiver.

D.4 Simulation Results

A 65nm commercial CMOS technology is used for the implementation. The I_{bias} of the LNA is provided from outside of the chip, and can be tuned to achieve various

power and noise performances, as summarized in Table D.1. V_{DD} can be lowered down to 0.4V for low-power operation. The current drawn from the V_{DD} (including LNA bias and core amplifier), I_{total}, varies from $0.33\mu A$ to $7.1\mu A$ and corresponds to a total power consumption of $0.2\mu W$ to $4.26\mu W$. The functionality of the bulk-feedback method is shown by the output DC voltage, $V_{dc,out}$, which is set to half of the V_{DD} (V_{ref}) with a maximum error of $4mV$. The capacitance ratio, $\frac{C_{in}}{C_f}$, is set to 10. The simulated closed-loop gain (A_v) is 19dB in all cases. Since large aspect ratios are utilized in the inverter, the 1dB discrepancy in the closed-loop gain is due to the parasitic capacitors at the inverter input. A 0.6V supply is used for the VGA, where the capacitance ratio is set to achieve $12dB$ closed loop gain of each stage. The maximum power consumption of the VGA is $1.1\mu W$ when the five stages are all activated, and it can be reduced down to $0.45\mu W$, depending on the input signal level. A 1.2V supply voltage is used for the EA, ED, and the comparator where the power consumption of these circuits at their typical biasing conditions is $0.012\mu W$, $0.036\mu W$, and $0.038\mu W$, respectively. Total power consumption of the US receiver is scalable from $1\mu W$ to $7\mu W$, while achieving an input-referred noise density ($IRND$) from $28.4nV/\sqrt{\text{Hz}}$ to $8.5nV/\sqrt{\text{Hz}}$ at $200kHz$ and a sensitivity from $100\mu V$ to $20\mu V$. On the transmitter side, the maximum available voltage in the technology used is 3.3V, which results in a power consumption of $3.4\mu W$ for the 1nF transducer considered in this work. This can be lowered down to $0.45\mu W$ and $1\mu W$ when V_{drive} is set to 1.2V and 1.8V, respectively.

Table D.1: Performance of the LNA

V_{DD} (V)	I_{bias} (nA)	I_{total} (μA)	$V_{dc,out}$ (mV)	A_v (dB)	IRND@200kHz ($nV/\sqrt{\text{Hz}}$)
0.6	10	0.33	299	19	26.2
	100	3.69	299	19	10.2
	200	7.1	299	19	8.5
0.4	10	0.41	198	19	28.4
	100	2.68	196	19	11.4

D.5 Discussion

The power consumption for the total US transceiver, including transmitter and receiver, with respect to the received voltage level, is shown in Fig.D.2. This trend shows an optimum where the power used in the transmitter and receiver are similar. When a more challenging scenario is to desired, e.g. when a longer communication distance is needed in harsh environmental conditions, the optimal point moves to higher power levels. This problem is addressed in this work, and a flexible transceiver

is proposed to cover a range of performance, as summarized in the bottom of Table D.2. The flexibility is achieved by varying V_{drive} at the transmitter and I_{bias} at the receiver. As a result, considering the 10m underwater communication scenario described in Sec.D.2, it can be shown that a voltage sensitivity around $70\mu V$ leads to an optimum power consumption of $2.20\mu W$, which is achievable with the proposed transceiver when $V_{drive} = 1.8V$, and $I_{bias} = 10nA$. The performance of the proposed

Table D.2: Performance Comparison of the proposed US transceiver

Specs	[49]	[50]	This Work*	
Frequency (kHz)	40.6	41	200	
CMOS process (nm)	65	250	65	
Modulation	OOK	OOK	OOK	
Data Rate (bps)	250	250	250	
Supply Voltage (V)	0.6	0.3	1.2 - 0.6 - 0.4	
Off-chip L&C	Yes	Yes	No	
On-CHIP Rx&Tx	No	No	Yes	
Communication Distance (m)	8.6 (air)	6.3 (air)	10 (shallow underwater)	
			Range	Optimal
Tx Power Consumption (μW)	16000	1000	0.45 - 3.4	1
Rx Power Consumption (μW)	4.4	1	0.95 - 7	1.2
Sensitivity (μV)	20	20	100 - 20	70

*Based on post-layout simulations

US transceiver and its comparison with relevant integrated US transceivers from recent literature is given in Table D.2. Each work uses the same modulation scheme and data-rate, but the prior art focuses on transmission in air, while we exploit US for underwater communication, where the US signal attenuation is much smaller. A super-regenerative receiver is proposed in [50], where a supply voltage of 0.3V is used and a power consumption of $1\mu W$ on the receiver side is achieved for $20\mu V$ sensitivity. The work in [49] achieves a $4.4\mu W$ receiver power consumption for $20\mu V$ sensitivity. Our work relaxes the receiver sensitivity requirements thanks to the underwater environment. To reach 10m communication distance, only $70\mu V$ receiver sensitivity is needed, which brings the power consumption in our receiver down to $1.2\mu W$. Besides, exploiting an holistic optimization of both transmitter and receiver power for the low-loss underwater environment, we achieve a total power consumption for the 10m communication link of only $2.2\mu W$.

D.6 Conclusion

The underwater medium offers various emerging applications demanding low-power circuit design to enable long-term continuous operations of the sensor nodes. This work presents a system-level design approach of a US transceiver, where it is shown

that the minimum power consumption can be achieved when transmitter and receiver performance are optimized together. The circuit implementation of the overall transceiver is described, and post-layout simulations show the suitability of the proposed circuits for use in underwater wireless sensor networks achieving extremely competitive, μW power budgets for communication in the 10m distance range.

Acknowledgement

This work has been funded by the European Union′s Horizon 2020 research and innovation programme under grant agreement No 665347.